RANS turbulence models for FENE-P viscoelastic fluids

Michael McDermott

School of Mechanical Engineering

University of Leeds

Submitted in accordance with the requirements for the degree of

Doctor of Philosophy

July 2022

The candidate confirms that the work submitted is his own, except where work which has formed part of jointly-authored publications has been included. The contribution of the candidate and the other authors to this work has been explicitly indicated below. The candidate confirms that appropriate credit has been given within the thesis where reference has been made to the work of others.

Papers Contributing to this Thesis

A FENE-P $k-\varepsilon$ Viscoelastic Turbulence Model Valid up to High Drag Reduction without Friction Velocity Dependence. Journal: *Applied Sciences*
https://doi.org/10.3390/app10228140.
Authors: Michael McDermott; Pedro Resende (PR); Thibaut Charpentier (TC); Mark Wilson (MW); Alexandre Afonso (AA); David Harbottle (DH); Gregory de Boer (GdB).
The models were developed and implemented in OpenFOAM by the candidate. The candidate also drafted and edited the manuscript. The co-authors (TC, MW, DH, GdB) are supervisors who provided guidance on the research. The co-authors (PR, AA) are research colleagues who provided guidance on the research.

An improved $k-\omega$ turbulence model for FENE-P fluids without friction velocity dependence. Journal: *International Journal of Heat and Fluid Flow*
https://doi.org/10.1016/j.ijheatfluidflow.2021.108799
Authors: Michael McDermott; Pedro Resende (PR); Mark Wilson (MW); Alexandre Afonso (AA); David Harbottle (DH); Gregory de Boer (GdB).
The models were developed and implemented in OpenFOAM by the candidate. The candidate also drafted and edited the manuscript. The co-authors (MW, DH, GdB) are supervisors who provided guidance on the research. The co-authors (PR, AA) are research colleagues who provided guidance on the research.

An anisotropic $k-\varepsilon-v^2-f$ model to predict turbulent polymer flow features in fully developed channel and square duct flows. In Review - Journal of Non-Newtonian Fluid Mechanics

Acknowledgements

I would like to thank my supervisors (Gregory de Boer, Mark Wilson, David Harbottle and Thibaut Charpentier) for the amazing guidance and support throughout this project. Special mention to Greg (primary supervisor) — with me being his first PhD student — has gone above and beyond to bolster this project and my own personal and career development.

Thank you to the Portuguese team (Pedro Resende and Alexandre Afonso) who gave me the opportunity to spend time at their university and work on developing the code and models required for the published work. Portugal is a beautiful country and the people I met, experiences I had, and the skills I gained, will forever be cherished. It has been a very enjoyable adventure and incredible learning experience at the University of Porto. Thank you to Fernando Pinho who I originally reached out to for the stay in Portugal. I have received pieces of advice on the current state of the art for modelling and that has been very useful for this project.

Thank you to work colleagues who supported in some technical difficulties in the project. Sam McMaster with advanced latex skills, and Charlie Lloyd with OpenFOAM advice.

Thank you to the University of Leeds pool and snooker club for the memories and friendships gained over my time at the University. We achieved such amazing feats through the years, which I will look back on and cherish.

Lastly, but not least, thank you to all my friends and family who supported me during my undergraduate and PhD. It has been a long road and I would not have been able to do it without all of your involvement.

Abstract

The development of robust turbulent viscoelastic models to predict drag reducing behaviour of polymer additives within industrial flows is highly sought after. The main objective of this thesis is to develop Reynolds Averaged Navier-Stokes (RANS) models based on the Finitely Extensible Nonlinear Elastic Peterlin (FENE-P) rheological constitutive model for the polymer chains, to predict mean features of drag reducing flows. A DNS database from multiple literature sources is collated to validate the closure models *a priori*, along with the performance of the models' mean field predictions. A new finite volume C++ computational solver is adapted in the OpenFOAM software to include the FENE-P parameters within the pre-existing turbulence class structure. A robust framework is developed for fully developed channel flow and square duct cases within foam-extend/4.0. A novel application of the groovyBC functionality is used to develop boundary conditions for the conformation tensor field.

Two isotropic models ($k-\varepsilon$ and $k-\omega$) are developed in the context of fully-developed channel flow which improve upon previous models. This is achieved with a modified damping function which mimics the viscoelastic effects on the turbulent redistribution process. The non-linear terms in the constitutive equation are also greatly improved with robustness and stability, by removing friction velocity dependence and reducing complexity. The model prediction span a larger DNS data set for friction Reynolds number, Re_{τ_0}, Weissenberg number, Wi_{τ_0}, maximum polymer extension, L^2, and concentration variation, β. An anisotropic $k-\varepsilon-v^2-f$ model is also developed to predict turbulent viscoelastic flow features in fully-developed channel flow and square ducts, via an extension to the Newtonian model. The non-linear closures are developed based on the premise that polymer stretching from near wall turbulent shears coincides and aligns with the mean vorticity direction, t_i, and redistributes energy to the wall normal direction, n_i, in a similar process to the Reynolds stress tensor. The predictions for the model include fully developed channel flow and square ducts, with flow features for the conformation tensor, Reynolds stresses, mean velocity (and the bending of the isolines), along with the shift of the secondary flow vorticity centre away from the wall.

Nomenclature

Greek symbols

β	Viscosity ratio	
γ	Shear rate magnitude	s^{-1}
δ_{ij}	Kronecker delta	
ε	Dissipation rate of turbulent kinetic energy	$\mathrm{m}^2\,\mathrm{s}^{-3}$
ε^V	Viscoelastic stress work of turbulent kinetic energy	$\mathrm{m}^2\,\mathrm{s}^{-3}$
ε_{ijk}	Levi-Civita symbol	
κ	Artificial numerical diffusivity constant	$\mathrm{m}^2\,\mathrm{s}^{-1}$
λ	Relaxation time of polymeric fluid	s
μ_0	Total dynamic viscosity	$\mathrm{kg}\,\mathrm{m}^{-1}\,\mathrm{s}^{-1}$
μ_p	Polymer dynamic viscosity	$\mathrm{kg}\,\mathrm{m}^{-1}\,\mathrm{s}^{-1}$
μ_s	Solvent dynamic viscosity	$\mathrm{kg}\,\mathrm{m}^{-1}\,\mathrm{s}^{-1}$
μ_T	Dynamic eddy/turbulent viscosity	$\mathrm{kg}\,\mathrm{m}^{-1}\,\mathrm{s}^{-1}$
ν_0	Total kinematic viscosity	$\mathrm{m}^2\,\mathrm{s}^{-1}$
ν_p	Polymer kinematic viscosity	$\mathrm{m}^2\,\mathrm{s}^{-1}$
ν_s	Solvent kinematic viscosity	$\mathrm{m}^2\,\mathrm{s}^{-1}$
ν_T	Kinematic eddy/turbulent viscosity	$\mathrm{m}^2\,\mathrm{s}^{-1}$
$\Pi^V_{v^2}$	Viscoelastic contribution to the pressure strain term	$\mathrm{m}^2\,\mathrm{s}^{-3}$
Π_{ij}	Pressure strain term	$\mathrm{m}^2\,\mathrm{s}^{-3}$
ρ	Fluid density	$\mathrm{kg}\,\mathrm{m}^{-3}$
σ_k	Constant coefficient in the k transport equation	
σ_ε	Constant coefficient in the ε transport equation	
σ_ω	Constant coefficient in the ω transport equation	

τ_w	Wall shear stress	$\mathrm{kg\,m^{-1}\,s^{-2}}$
τ_{ij}	Shear stress tensor	$\mathrm{kg\,m^{-1}\,s^{-2}}$
Φ	General fluid flow variable	
ω	Specific dissipation rate of turbulent kinetic energy	$\mathrm{s^{-1}}$
ω_x	Mean stream-wise vorticity	$\mathrm{s^{-1}}$
Ω_{ij}	Mean rate of vorticity	$\mathrm{s^{-1}}$

Latin symbols

C_1	Constant coefficient in the f transport equation	
C_2	Constant coefficient in the f transport equation	
C_η	Constant coefficient in the turbulent time scale	
C_μ	Constant coefficient in the eddy viscosity model	
$C_{\omega 1}$	Constant coefficient in the ω transport equation	
$C_{\omega 2}$	Constant coefficient in the ω transport equation	
C_ω	Constant coefficient in the ω transport equation	
$C_{\varepsilon 1}$	Constant coefficient in the ε transport equation	
$C_{\varepsilon 2}$	Constant coefficient in the ε transport equation	
C_A	Constant coefficient in the f_v damping function model	
C_B	Constant coefficient in the f_v damping function model	
C_{ij}	Mean conformation tensor	
C_L	Constant coefficient in the turbulent length scale	
C_{N1}	Constant coefficient in the NLT_{ij} closure model	
C_{N2}	Constant coefficient in the NLT_{ij} closure model	
C_{N3}	Constant coefficient in the NLT_{ij} closure model	
C_{N4}	Constant coefficient in the E_{τ_p} closure model	
C_T	Constant coefficient in the turbulent length scale	
DR	Drag reduction	
E^V	Newtonian destruction to the dissipation rate	$\mathrm{m^2 s^{-4}}$

$f(C_{mm})$	Peterlin function	
f	Elliptic relaxation function	s^{-1}
$f_\mu, f_v, f_1, f_2, f^d, f_t$	Damping functions	
f_N	Local eddy viscosity	
h	Channel half height	m
HDR	High drag reduction	
IDR	Intermediate drag reduction	
J_Φ	Diffusive term of Φ	
k	Turbulent kinetic energy	$\mathrm{m}^2\,\mathrm{s}^{-2}$
L^2	Maximum extensibility of the dumbbell model	
L_t	Turbulent length scale	m
LDR	Low drag reduction	
M_{ij}	Mean flow distortion term of the conformation tensor transport	s^{-1}
N_{ij}	Redistribution term of Reynolds stress normal components	
n_i	Wall normal direction	
NLT_{ij}	Non-linear term of the conformation tensor transport	s^{-1}
P	Mean kinematic pressure	$\mathrm{kg\,m}^{-1}\,\mathrm{s}^{-2}$
P_h	'Wetted' perimeter	m
P_k	Mean rate of production of turbulent kinetic energy	$\mathrm{m}^2\,\mathrm{s}^{-3}$
Q^V	Viscoelastic turbulent transport of turbulent kinetic energy	$\mathrm{m}^2\,\mathrm{s}^{-3}$
R_h	Hydraulic radius	m
Re_{τ_0}	Friction Reynolds number	
S_Φ	Production term of Φ	
S_{ij}	Mean rate of strain	s^{-1}
t_i	Mean vorticity direction	
T_t	Turbulent time scale	s
u, v, w	Velocity components	$\mathrm{m\,s}^{-1}$

U_i	Mean velocity	$\mathrm{m\,s^{-1}}$
v^2	Near wall Reynolds stress scaling	$\mathrm{m^2\,s^{-2}}$
Wi_{τ_0}	Friction Weissenberg number	

Superscript/subscript

$\hat{a}$	Instantaneous quantity
$\overline{a}, A$	Mean quantity
$\overset{\nabla}{a}$	Oldroyd's upper convective derivative
a'	Fluctuating quantity
a^+	Normalised by friction velocity
a^N, a_s	Newtonian/Solvent quantity
a^V, a_p	Viscoelastic/Polymeric quantity
a_w	Near wall quantity

Contents

Publication Statement i

Papers Contributing to this Thesis ii

Acknowledgements iii

Abstract iv

Nomenclature v

Table of Contents ix

List of Figures xi

List of Tables xvi

1 Introduction 1

1.1 Drag reducers and turbulent control 2

1.2 Mathematical modelling 4

1.2.1 Turbulence 5

1.2.2 Polymers 10

1.3 Literature review 15

1.3.1 Drag reduction and mechanisms 15

1.3.2 Models for drag reducing turbulent channel flow 17

1.3.3 Summary of literature, aims and objectives 21

1.4 Contributions of this thesis 22

2 Numerical Procedure 24

2.1 OpenFOAM viscoelastic turbulence code 25

2.2 Case set-up 28

3 A FENE-P $k-\varepsilon$ Viscoelastic Turbulence Model Valid up to High Drag Reduction without Friction Velocity Dependence 34

3.1 Introduction 35

3.2 Governing Equations 35

3.2.1 Model for the Reynolds Stress Tensor . . . 36
3.2.2 Transport Equation for the Turbulent Kinetic Energy . . . 36
3.2.3 Transport Equation for the Rate of Dissipation of Turbulent Kinetic Energy . . . 37
3.3 Development of Viscoelastic Closures . . . 38
3.3.1 Closure for NLT_{ij} . . . 39
3.3.2 Model for the Modified Damping Function, f_v . . . 43
3.3.3 Development of Closures for ε^V and E^V . . . 45
3.4 Summary of the new $k-\varepsilon$ model . . . 47
3.5 Numerical Procedure . . . 48
3.6 Results and Discussion . . . 49
3.6.1 Analysis of Conformation Tensor . . . 49
3.6.2 Analysis of k, ε and v_T . . . 50
3.6.3 Analysis of Stresses and Velocity Profiles . . . 52
3.7 Conclusions . . . 56

4 An improved $k-\omega$ turbulence model for FENE-P fluids with β variation 57
4.1 Introduction . . . 58
4.2 Governing Equations . . . 58
4.3 Turbulence Model . . . 59
4.4 Development of viscoelastic closures . . . 62
4.4.1 Closures for the conformation tensor . . . 64
4.4.2 Model for the modified damping function, f_μ . . . 67
4.4.3 Development of closures within the k and ε transport equations . 69
4.5 Summary of the new $k-\omega$ model . . . 70
4.6 Results and discussion . . . 71
4.7 Conclusions . . . 78

5 An anisotropic $k-\varepsilon-v^2-f$ model to predict turbulent polymer flow features in fully developed channel and square duct flows 80
5.1 Introduction . . . 81
5.2 Governing Equations . . . 81
5.2.1 Reynolds stresses . . . 82
5.2.2 Streamwise vorticity equation . . . 85
5.3 Development of viscoelastic closures . . . 86
5.3.1 Closures for the conformation tensor . . . 86
5.3.2 Closure for Reynolds Stresses . . . 93
5.3.3 Closures for the transport of k, ε, v^2 and f . . . 94
5.4 Summary of the present model . . . 97
5.5 Numerical procedure . . . 99
5.6 Results and discussion . . . 100

5.6.1 Analysis of C_{ij} . . . 100
5.6.2 Analysis of Reynolds stresses and dissipation rate . . . 101
5.6.3 Analysis of mean velocity and secondary flow . . . 104
5.7 Conclusion . . . 107

6 Conclusions and future work **108**
6.1 DNS data, numerical procedure and OpenFOAM . . . 109
6.2 Isotropic $k-\varepsilon$ and $k-\omega$ models . . . 109
6.3 Anisotropic $k-\varepsilon-v^2-f$ model . . . 110
6.4 Future work . . . 111

List of Figures

1.1 Heuristic diagram on the nature of turbulence with (a) the transition from laminar to the turbulent regime of a candle plume and (b) the energy cascade mechanism of turbulence. 3
1.2 Drag reduction in turbulent channel flow under constant pressure gradient (thus same wall shear stress) 6
1.3 A schematic representation of the hierarchy of turbulence modelling. . . . 7
1.4 Real linear polymer chains, recorded using an atomic force microscope on a surface, under liquid medium. 10
1.5 Polymer representation by $N = 10$ beads connected by non-linear springs. 11
1.6 The end-to-end vector of the molecule is denoted as q. Schematic of polymer stretch (and relaxation) in shear flow. Polymer stretch is characterised by the change in q. 12
1.7 Semi-log plot of u^+ and y^+ from Abubakar et al. showing the change in velocity profile with varying S^+ up to the maximum drag reduction line. . 16
1.8 PIV of turbulent shear flow near the wall region captured by Dubief: Newtonian fluid (left) and viscoelastic fluid of drag reduction 60% (right). 17

2.1 Computational domain and mesh for (a, b) channel ($x-y$ plane), and (c, d) square duct ($y-z$ plane). Figures (b, d) show an isometric view of the channel and square duct, respectively. 33

3.1 Comparison of the NLT_{ij} model between DNS data (+DR = 37%, case (19)) and predictions with the new model (continuous lines), and previous model [70] (dash lines). 42
3.2 Comparison of the f_v model between DNS data ($\times$ crosses) and predictions with the new model (continuous lines), and previous model (dash lines): each colour represents a different drag reduction regime: red (low drag reduction (LDR), case 16); blue (intermediate drag reduction (IDR), case 19); green (high drag reduction (HDR), case 20). 45
3.3 Comparison of the ε^V normal components between DNS data ($xx : \diamond$, $yy : \times$, $zz : +$) and model predictions (xx : solid line, yy and zz : dashed line): each colour represents a different drag reduction regime: red (LDR, case 16); orange (HDR), case 22). 46

3.4 Comparison of the conformation tensor between DNS data ($\times$ crosses) and predictions with the new model (continuous lines), and previous model (dash lines). Each colour represents a different drag reduction regime: red (LDR, case 16); blue (IDR, case 19); green (HDR, case 20) and orange (very HDR, case 26. DNS data not available for C_{xy}). 50
3.5 Comparison of turbulent kinetic energy between DNS data ($\times$ crosses) and predictions with the new model (continuous lines), and previous model (dash lines): (**a**) $Re_{\tau_0} = 395$—red (LDR case 16)—and blue (IDR case 19); (**b**) $Re_{\tau_0} = 125$—green (HDR, case 7) and $Re_{\tau_0} = 1000$—blue (IDR, case 27). 51
3.6 Comparison of the rate of Newtonian dissipation of k between DNS data ($\times$ crosses) and predictions with the new model (continuous lines), and $v^2 - f$ model of Masoudian et al. (dash lines). Each colour represents a different drag reduction regime: red (LDR case 16); orange (HDR case 22). 52
3.7 Comparison of the (**a**) local eddy viscosity and (**b**) mean streamwise velocity profile, between DNS data ($\times$ crosses) and model predictions (continuous lines). Each colour represents a different drag reduction regime: red (LDR case 16); blue (IDR case 19); green (HDR case 20); orange (very HDR case 22). 53
3.8 Comparison of the stresses at (a) LDR, (b) IDR and (c) HDR, between DNS data (symbols) and model predictions (lines). 54
3.9 Comparison of the velocity profiles between DNS data ($\times$ crosses), current model predictions (continuous lines) and previous model predictions (dashed lines). Each colour represents a different drag reduction regime: (**a**) red (LDR case 1); blue (IDR case 10); orange (very HDR case 15). (**b**) blue (IDR case 27); orange (very HDR case 26). 55

4.1 (a) Near-wall scaling comparison between y^+ (solid line) and y^* (Equation 4.11) (dashed lines). (b) The damping function (Equation 4.10) compared with Equation 4.12 in Newtonian turbulent channel flow at $Re_{\tau_0} = 180, 395$ and 590. 61
4.2 Comparison of the velocity profiles for Newtonian turbulent channel flow at $Re_{\tau_0} = 180, 395$ and 590 with DNS data (symbols) and model predictions (solid lines). 62
4.3 Comparison of the NLT_{ij} components between DNS data (symbols) and model predictions (lines) for channel flow at $Re_{\tau_0} = 395$: (a) NLT_{xx} (legend used for all figures); (b) NLT_{yy}; (c) NLT_{zz}; (d) NLT_{xy}. Each colour represents a different drag reduction regime: case 16 (LDR); case 19 (IDR); case 20 (HDR). 66

4.4 Comparison of the (a) local eddy viscosity and (b) mean production of turbulent kinetic energy between DNS data (symbols) and model predictions (lines) for channel flow at $Re_{\tau_0} = 395$. Newtonian and case 16 (IDR). 68
4.5 Effect of varying parameters C_A and C_B on the mean velocity profile for IDR (case 19). DNS given by blue cross ($\times$). 68
4.6 Comparison of the conformation tensor components between DNS data (symbols) and model predictions (lines) for channel flow at $Re_{\tau_0} = 395$: (a) C_{xx}/L^2 (legend used for all figures); (b) C_{yy}/L^2; (c) C_{xy}. case 16 (LDR) and case 20 (HDR). 72
4.7 Comparison of the turbulent kinetic energy, k, between DNS data (symbols) and model predictions (lines) for channel flow at $Re_{\tau_0} = 395$. Newtonian, case 16 (IDR). 73
4.8 Comparison of the turbulent kinetic energy, k, and damping function, f_μ, between DNS data (symbols) and model predictions (lines) for channel flow at $Re_{\tau_0} = 395$: (a) case 16 (LDR); (b) case 20 (HDR). 74
4.9 Comparison of the true Newtonian dissipation rate of k between DNS data (symbols) and model predictions (lines) for channel flow at $Re_{\tau_0} = 395$: (a) case 16 (LDR); (b) case 20 (HDR). 74
4.10 Comparison of the local eddy viscosity between DNS data (symbols) and model predictions (lines) for channel flow at $Re_{\tau_0} = 395$. Each colour represents a different drag reduction regime: Newtonian; case 16 (LDR); case 19 (IDR); case 20 (HDR); case 22 (Very HDR); case 24 (MDR). . . 75
4.11 Comparison of (a) normalised shear stresses (case 19 (IDR)) and (b) mean streamwise velocity profiles between DNS data (symbols) and model predictions (lines) for channel flow at $Re_{\tau_0} = 395$. Each colour represents a different drag reduction regime: case 16 (LDR); case 19 (IDR); case 20 (HDR); case 22 (Very HDR); case 24 (MDR). The viscous sub-layer equation, log layer equation, and Virk's asymptote are also shown (dotted lines) in (b). 75
4.12 Comparison of normalised shear stresses at (a) LDR (case 16) and (b) HDR (case 20), between DNS data (symbols) and model predictions (lines) for channel flow at $Re_{\tau_0} = 395$. 76
4.13 Comparison of the mean streamwise velocity profiles between DNS data (symbols) and model predictions (lines) for channel flow at various Reynolds numbers. Each colour represents a different case. See Figure 4.11b for dotted lines. 76

4.14 Comparison of the mean streamwise velocity profiles between DNS data (symbols) and model predictions (lines) for channel flow at varying β at $Re_{\tau_0} = 180$. Each colour represents a different case. See Figure 4.11b for dotted lines. 77

5.1 DNS data of the in-plane anisotropy, $\overline{w'w'} - \overline{v'v'}$, in fully developed channel flow at $Re_{\tau_0} = 395$ with lines: Newtonian (black); 18% DR (red); 37% DR (blue) and 48% (green). 86
5.2 Comparison of the C_{xy} component with DNS data at DR=37% ($Re_{\tau_0} = 395$, $Wi_{\tau_0} = 100$, $L^2 = 900$): ($\times$) DNS data, green line is term I in Equation (5.29), red line is term II in Equation (5.29), black line is the sum of term I and term II in Equation (5.29). 87
5.3 Comparison of the NLT_{yy} (solid line) and NLT_{zz} (dashed line) component with DNS data in fully developed channel flow at $Re_{\tau_0} = 395$ with DR= 18% (red), 37% (blue), 51% (green). 89
5.4 *A priori* DNS data of NLT_{ij} (Equation (5.34)) at 18% DR in fully developed channel flow. Symbols ($\times$) and solid lines are the LHS and RHS of Equation (5.34), respectively. Each normal component is represented by colours: *kk* (black), *xx* (red), *yy* (blue), *zz* (green). 90
5.5 Comparison of the DNS data for NLT_{v^2} and the model of Equation (5.35) in fully developed channel flow with LDR (red), IDR (blue) and HDR (green): NLT_{kk} ($\times$), NLT_{v^2} (+), Equation (5.35). 91
5.6 Comparison of the NLT_{ij} model predictions (solid lines) with DNS data case DR=18% ($Re_{\tau_0} = 395$, $Wi_{\tau_0} = 25$, $L^2 = 900$, $\beta = 0.9$) (crosses) in fully developed channel flow (a, b), and square duct model predictions (c, d): (a) NLT_{kk}, (b) NLT_{yy}, (c) NLT_{kk}, (d) NLT_{yy} + NLT_{zz}. The colour scale ranges from 0 (blue) to 10.4 (red) for (c), and 0 (blue) to 1.2 (red) for (d). 92
5.7 Comparison of the spanwise Reynolds stress component, w'^2, in fully developed channel flow with DNS data (crosses) and *a priori* model (solid lines) given by Equation (5.39). Newtonian in black (DR=0%, $Re_{\tau_0} = 395$), and LDR in red (DR=18%, $Re_{\tau_0} = 395$, $Wi_{\tau_0} = 25$, $L^2 = 900$, $\beta = 0.9$). 94
5.8 Comparison of the C_{ij} model predictions (solid lines) with DNS data case 'A' (crosses) in fully developed channel flow (a, b), and square duct model predictions (c, d): (a, c) C_{kk} and (b, d) C_{xy}. The colour scale ranges from 0 (blue) to 450 (red) for (c), and -30 (blue) to 30 (red) for (d). 101
5.9 Comparison of the $\overline{u_i'u_j'}$ model predictions (lines) with DNS data from Newtonian [14] (crosses) and case 'A' (plus) in fully developed channel flow. Each colour represents a different Reynolds stress component: (a) $\overline{u'u'}$ (red), $\overline{v'v'}$ (blue), $\overline{w'w'}$ (green); (b) $\overline{u'v'}$ (black). Solid lines are Newtonian, and dashed lines are case 'A'. 102

5.10 Model predictions of (a, b) wall Reynolds stress, $\overline{v^2}$, and (c, d) Reynolds shear stress magnitude, $\nu_T \sqrt{S_{pq} S_{pq}}$, in square duct flow with the same comparative flow conditions as DNS data case 'A': (a, c) Newtonian, and (b, d) LDR. The colour scale ranges from 0 (blue) to 1 (red) in all figures. 103
5.11 Comparison of the ε^+ predictions (solid lines) with DNS data from Newtonian (crosses) and case 'A' (plus) in fully developed channel flow (a), and square duct model predictions (b, c): (b) Newtonian, and (c) LDR. The colour scale ranges from 0 (blue) to 0.2 (red). 104
5.12 Comparison of the U^+ predictions (lines: solid line, Newtonian; dashed line, case 'A') with DNS data from Newtonian (crosses) and case 'A' (plus) in fully developed channel flow (a), and square duct model predictions (b, c): (b) Newtonian, and (c) LDR. The colour scale ranges from 0 (blue) to 20 (red). 105
5.13 Model predictions of (a,b) V^+, and (c) cross streamlines, in square duct flow with the same comparative flow conditions as DNS data from Newtonian and case 'A': (a) Newtonian, (b) LDR, and (c) Newtonian (red) and LDR (green). The colour scale in (a, b) ranges from -0.5 (blue) to 0.5 (red). 106

6.1 Model predictions of fully developed triangular (equilateral) duct flow at $Re_{\tau_0} = 395$ for $DR = 0\%$ (Newtonian) and $DR = 18\%$ (LDR). (a, b) mean velocity, U^+; (c, d) wall normal Reynolds stress, v^{2+}; (e, f) NLT_{ij}^+ components. 112
6.2 Model predictions of cross streamlines in fully developed triangular (equilateral) duct flow at $Re_{\tau_0} = 395$: Newtonian (red) and LDR (green). . 113
6.3 Mean confirmation tensor DNS data for ($DR = 27\%, Re_{\tau_0} = 180$, $L^2 = 3600$, $Wi_{\tau_0} = 18$) [75] 116
6.4 Mean velocity and vorticity DNS data for ($DR = 27\%, Re_{\tau_0} = 180$, $L^2 = 3600$, $Wi_{\tau_0} = 18$) [75] 116

List of Tables

1.1 Energy and time scales for eddy viscosity models used in this thesis. . . . 10
1.2 Terms appearing in the governing transport equations (Equation (1.1)) for fully developed turbulent flow described by a RANS FENE-P model in Cartesian coordinates. . . . 15

2.1 Sensitivity study with varying κ . . . 28
2.2 Summary of the boundary conditions used in the numerical simulations. Subscript *in* and *out* is defined as the inlet and outlet patch, respectively. Δp is the pressure drop specified, which for our set-up simplifies to be $\Delta P = |\Delta x|$. . . . 32

3.1 Independent DNS data for turbulent channel flow of FENE-P fluids at $\beta = 0.9$, with DR model predictions. . . . 39

4.1 Independent DNS data of fully-developed turbulent channel flow for FENE-P fluids with DR model predictions. . . . 63
4.2 Sensitivity study of drag reduction value with variations in f_μ parameters C_A and C_B by $\pm 10\%$ and $\pm 20\%$. . . . 69

5.1 List of model Newtonian and viscoelastic coefficients. . . . 97

Chapter 1

Introduction

1.1 Drag reducers and turbulent control

Turbulent flow can be characterised by the chaotic motion of velocity and pressure fields within a fluid flow system, differing from laminar flow in which fluid flows in parallel layers with no disruption between those layers.

Turbulent flow occur throughout nature, such as the plume of a candle flame (Figure 1.1a); the wake formation from air flowing over objects; atmospheric and sea currents; and volcanic eruptions. Although there is no exact definition of turbulent flow, it has a number of characteristic features such as:

- Irregularity: Turbulent flows are always highly irregular, and are treated statistically as a result of their chaotic nature.
- Diffusivity: Turbulent flows are highly diffusive, which gives rise to enhanced mixing and increased rates of momentum and energy transfer.
- Rotationality: Turbulent flows have non-zero vorticity with strong 3-dimensional vortex generation known as vortex stretching. This is the principle mechanism on which the turbulent energy cascade relies to establish and maintain identifiable structure function. The spatial structures are known as *eddies* and can loosely be defined as coherent patterns of flow velocity and pressure at varying length scales. Turbulent flows can be viewed as the entire hierarchy of eddies with distinct energy spectra.
- Dissipation: Sustaining turbulent flow requires a consistent energy source as turbulence dissipates rapidly by converting kinetic energy to thermal energy. The energy cascades from large eddies (containing most of the kinetic energy) to small eddies where they are destroyed by viscous forces and dissipated into thermal energy (Figure 1.1b). This process of energy transfer from larger to smaller eddies is known as the *energy cascade*.

In the transport of fluids, turbulence typically hinders flow due to interacting eddies that induce turbulent drag in the form of frictional forces in the domain. Formulating efficient drag reducing technologies for transport systems is economically and ecologically advantageous. Examples include the topology of wings on an aircraft; or a turbulent channel flow, where the goal is to minimise the work required to transport the fluid. In the current study, turbulence is generated by high shearing forces within wall bounded pressure driven flow, which has steady mean fields, fully developed and incompressible.

The methods employed to reduce the drag in channel flow transport systems include passive and active control. Passive control involves techniques which do not require direct energy input, typically by a surface or geometrical modification. Such examples are riblets and liquid infused fluid films. Active control requires direct energy input by additives or

(a)

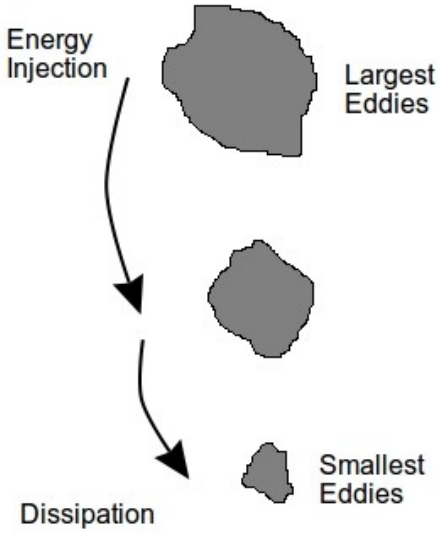

(b)

Figure 1.1: Heuristic diagram on the nature of turbulence with (a) the transition from laminar to the turbulent regime of a candle plume [1] [photograph by Gary Settles, distributed under a CC BY-SA 3.0 license.] and (b) the energy cascade mechanism of turbulence.

by body forces such as near-wall flow disturbances with Lorentz forces [2]; blowing and suction techniques [3]; cross-flow pressure gradients and wall motion to disrupt the self-sustaining turbulence production mechanisms – typically with transverse-travelling waves [4], spanwise or streamwise oscillations [5], and streamwise-travelling waves of spanwise wall velocity [6]; surfactants [7]; fibres (rigid polymer additives) [8]; and elastic polymer additives [9]. The latter is considered in this thesis, specifically high molecular weight dilute polymer additives.

Toms [10] discovered that minute amounts of long-chain polymer additives reduce the pressure losses in turbulent flow. Drag reduction by additives was already known with the use of fibres in the paper making processes, however polymer additives showed the same drag reducing effects with concentrations two orders of magnitude lower (roughly 10 parts per million (ppm) or gm^{-3}). This discovery clearly demonstrates potential for industrial application in energy saving solutions. To this day, polymer additives remain the most efficient way to reduce drag in the industrial processes, along with relatively low environmental and health impacts compared to other materials such as asbestos fibres [11].

A good example of the use of drag reducing polymer additives is in the Trans-Alaska Pipeline System and their installed pumps. The addition of polymers to crude oil in this pipeline started in 1979. The desired discharge of two million barrels per day could be obtained without the construction of two additional pumping stations planned [12]. The performance of the polymers was later increased by a factor of 12 by increasing the

molecular weight of the polymers. However, this led to greater sensitivity to mechanical degradation which required sophisticated injection points downstream to minimise these effects. Nowadays the polymer concentration is of order 1 ppm, resulting in an increased flow rate of 33%. Furthermore, the use of drag reducing polymers is accompanied by a decrease in the heat exchange. Consequently, the crude-oil can be kept at higher temperatures which naturally decreases the viscosity, resulting in higher flow rates for an equivalent pumping power. Other notable examples of drag reducing polymers for industry application include: sewer flow systems, especially during increased levels of heavy rainfall; central heating systems such as the primary flow circuits of large heating systems, cooling flow circuits and air conditioning; and ships and submerged bodies, where the drag reducing particles are added to the turbulent boundary layer.

With the rise of computational power over the last few decades, numerical simulations allow researchers to better understand the mechanics and turbulent statistics that underpin the interactions between the polymer chains and turbulent structures. The physics are examined with Direct Numerical Simulations (DNS) which can provide insight into the mechanisms of drag reduction. More details of DNS is presented in section 1.2.1. Owing to the large simulation times of DNS, there is a need to capture mean flow features at a fraction of the computational cost. Sophisticated mathematical models can be formulated from *a priori* analysis of the DNS data, which are able to predict drag reducing features for a given system. The focus of this thesis is the development of such mathematical models to predict the effects of enhancements to flow rate produced by drag reducing polymers within wall bounded turbulent flows.

1.2 Mathematical modelling

Throughout this thesis, tensor notation is applied to all quantities, such that — for a general field, a — a scalar, vector, and 2-rank tensor are denoted by a, a_i and a_{ij}, respectively. Some scalars have subscripts for descriptive purposes and are defined accordingly (e.g a scalar a_s for solvent part). Repeating indies on 2-rank tensors represent the trace component, e.g $a_{kk} = a_{11} + a_{22} + a_{33}$. It is convention that 2 indies cannot appear twice, such that for multiple trace terms, an equation may contain a_{kk}, a_{mm}.. etc. Cartesian coordinates are applied with defined position vectors $x_i = (x, y, z)$, and velocity vectors $u_j = (u, v, w)$, moving with time t.

Modelling turbulent viscoelastic flows requires an understanding of the mathematical framework in order to obtain feasible numerical predictions. The concepts developed within continuum mechanics over the last half-century build a modelling map to achieve this. The governing equations of fluid flow represent mathematical statements of the conservation laws of physics. The general transport equation for a fluid flow variable, Φ,

is given by [13],

$$\frac{D(\rho\Phi)}{Dt} \equiv \underbrace{\frac{\partial(\rho\Phi)}{\partial t}}_{\substack{\text{Rate of change} \\ \text{of } \Phi}} + \underbrace{\frac{\partial}{\partial x_i}(\rho\Phi\hat{u}_j)}_{\substack{\text{Convective transport} \\ \text{of } \Phi}} + \underbrace{\frac{\partial}{\partial x_i}(J_\Phi)}_{\substack{\text{Diffusive transport} \\ \text{of } \Phi}} = \underbrace{S_\Phi}_{\substack{\text{Production or} \\ \text{destruction of } \Phi}}, \tag{1.1}$$

where ρ is fluid density and $\hat{u}_j$ is the instantaneous fluid velocity. For $\Phi = 1$, the conservation of mass arises - which for constant density (incompressible flow), reads

$$\frac{\partial \hat{u}_j}{\partial x_j} = 0. \tag{1.2}$$

For $\Phi = \hat{u}_i$, the conservation of momentum arises such that

$$\rho\frac{\partial \hat{u}_i}{\partial t} + \rho\hat{u}_j\frac{\partial \hat{u}_i}{\partial x_j} = -\frac{\partial \hat{p}}{\partial x_i} + \frac{\partial}{\partial x_j}\hat{\tau}_{ij}, \tag{1.3}$$

where $\hat{p}$ is the instantaneous pressure, and $\hat{\tau}_{ij}$ is the instantaneous stress tensor. - which describes the rheology of the fluid. $\hat{\tau}_{ij}$ is comprised of a solvent ($\hat{\tau}_{ij,\mathrm{s}}$), polymer ($\hat{\tau}_{ij,\mathrm{p}}$), and turbulent ($\hat{\tau}_{ij,\mathrm{t}}$), part:

$$\hat{\tau}_{ij} = \hat{\tau}_{ij,\mathrm{s}} + \hat{\tau}_{ij,\mathrm{p}} + \hat{\tau}_{ij,\mathrm{t}}. \tag{1.4}$$

The stress of the solvent obeys Newton's law of viscosity,

$$\hat{\tau}_{ij,\mathrm{s}} = \mu_\mathrm{s}\hat{s}_{ij} \equiv \frac{\mu_\mathrm{s}}{2}\left(\frac{\partial \hat{u}_i}{\partial x_j} + \frac{\partial \hat{u}_j}{\partial x_i}\right), \tag{1.5}$$

where μ_s is the solvent viscosity coefficient, and $\hat{s}_{ij}$ is the instantaneous strain rate. The mathematical representation of the turbulent and polymer stresses components are described in further sections.

Drag reduction (DR) of turbulent polymer flow occurs when $\hat{\tau}_{ij,\mathrm{t}}$ decreases with increasing $\hat{\tau}_{ij,\mathrm{p}}$. This can be viewed in Figure 1.2, which shows a schematic of DR in turbulent polymer channel flow with a constant pressure drop — laminar ($\hat{\tau}_{ij,\mathrm{t}} = 0, \hat{\tau}_{ij,\mathrm{p}} = 0$), Newtonian turbulence ($\hat{\tau}_{ij,\mathrm{p}} = 0$, denoted 'N'), and polymeric turbulence (denoted 'V' or 'p'). The scaled wall direction is given by $y^+ = (y/h)\cdot Re_{\tau_0}$, where h is the channel half-height, and $Re_\tau = \rho h u_\tau/\mu_0$ is the friction Reynolds number, μ_0 is the total viscosity, $u_\tau = \sqrt{\tau_w/\rho}$ is the friction velocity, and τ_w is the wall shear stress.

1.2.1 Turbulence

DNS

Direct Numerical Simulations are used within Computational Fluid Dynamics (CFD) to obtain numerical insight into the governing dynamics of a turbulent system (Figure 1.3).

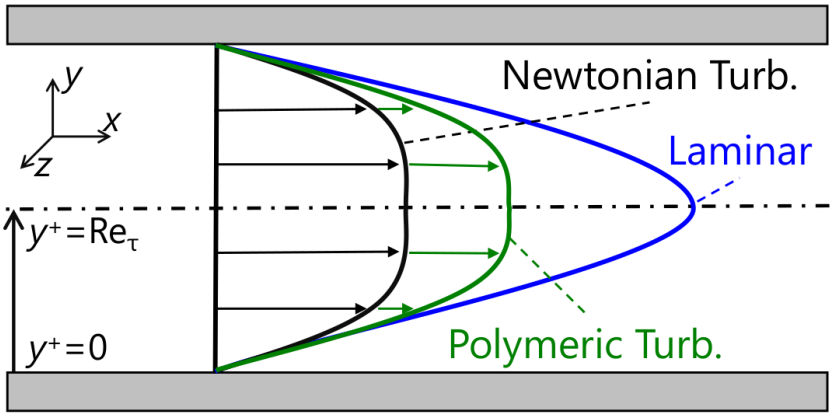

Figure 1.2: Drag reduction in turbulent channel flow under constant pressure gradient (thus same wall shear stress) [9]. [Reprinted with permission from L. Xi, "Turbulent drag reduction by polymer additives: Fundamentals and recent advances", Physics of Fluids **31**, 121302 (2019). Copyright (2019) AIP Publishing.]

The procedure involves solving the continuity and Navier-Stokes equations (1.2) and (1.3) numerically without any turbulence model. This is achieved by resolving the computational mesh to capture the smallest spatial scales (Kolmogorov scales) and smallest temporal scales, meaning DNS has a high computational demand. The Reynolds numbers within typical industrial systems (e.g. pipeline systems) are too large to simulate at this resolution with the current computational power available. At lower Reynolds numbers, it is possible to resolve these systems, although the computational demand is still high. This provides the ability to perform *numerical experiments* to gain insight into the mechanics of the system where experiments are not feasible or impossible to extract the required data. DNS is a useful tool in the development and performance testing of turbulence models in practical applications. This is achieved by *a priori* tests in which the DNS data is used exclusively as input data to analyse a pre-simulation hypothesis; or *a posteriori* where the DNS data is used to compare with the results obtained post-simulation for accurate modelling. DNS data from studies on Newtonian flows [14] and viscoelastic flows [15, 16] are used throughout this thesis to ascertain model performance.

LES

Large eddy simulation (LES) is a mathematical model used for turbulence. It was first applied by Smagorinsky [17] to study atmospheric currents, then formulated by Deardorff [18]. The principal idea behind LES is to reduce the computational cost of DNS by ignoring the smallest length scales, which are the most computationally expensive to resolve, via low-pass filtering of the Navier–Stokes equations. Such a low-pass filtering, which can be viewed as a time- and spatial-averaging, effectively removes small-scale information from the numerical solution.

Complexity arises when considering closure models for LES of turbulent viscoelas-

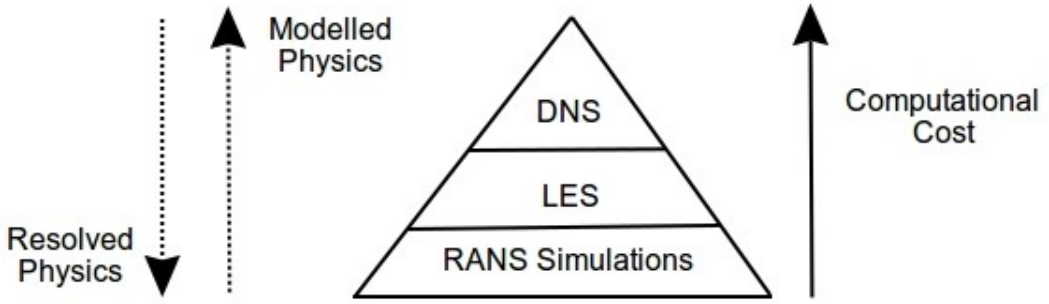

Figure 1.3: A schematic representation of the hierarchy of turbulence modelling.

tic fluids, due to the changes in time and spatial scales with the presence of polymers. LES for Newtonian fluids deploy subgrid-scale (SGS) closures that are statistically independent. For viscoelastic fluids, the scales of motion are much more involved and thus hamper the development of adequate SGS closure models for LES of turbulence with polymer additives [19]. Only a handful of researchers have studied this problem by attempting to construct a workable mixed SGS model suitable for turbulent viscoelastic flows. Thais et al. [20] was the first to adopt a temporal approximate deconvolution model (TADM) to perform LES on turbulent viscoelastic channel flow, in which they derived the filtered governing equations. The main idea of TADM is to perform spatial filtering for the momentum equation and temporal filtering for the conformation tensor transport equation respectively. Feng-Chen et al. [21] developed a new mixed sub-grid model based on coherent structures and TADM. It was found that TADM was better suited for turbulent viscoelastic channel flow. The model shows excellent agreement with DNS data for Reynolds shear stress, friction factor and DR% for polymer additives and surfactants in turbulent channel flow. However, the spatial filtering is limiting — showing an excess of the energy dissipation near the channel wall. Further improvements on the spatial filtering were made by Li et al. [22] for surfactants. These results showed promise for high Reynolds number but performed poorly for low Reynolds number against DNS data in turbulent channel flow. More work by Li et al. [23] develops an N-parallel FENE-P constitutive model for polymer additives based on multiple relaxation times with an improved mixed SGS model. With this parallel FENE-P model, stress-strain relationships of different micro-structures are more truly modelled than with a standard FENE-P model. The results show improvement to the low Reynolds number regime of DR parameters against DNS turbulent channel flow. Due to the infancy of the research area, there is a lack of reports for the mixed SGS model's performance in complex industrial geometries using a finite volume approach. More of these studies are required in the field for a fully reliable LES turbulent viscoelastic model applicable to industrial flows.

In the context of this thesis, we will not focus on LES, but rather on Reynolds Averaged Navier-Stokes (RANS) modelling, which is the topic of the following sub sections.

RANS

The Reynolds averaging procedure employs what is known as a Reynolds decomposition, which defines the instantaneous field by their average and fluctuating components. The decomposition takes the form,

$$\hat{u}_i(x_i,t) = \underbrace{U_i(x_i)}_{\text{mean}} + \underbrace{u_i'(x_i,t)}_{\text{fluctuating}} \quad \text{and} \quad \hat{p}(x_i,t) = P(x_i) + p'(x_i,t). \tag{1.6}$$

Here, mean averages are time averages such that

$$U_i(x_i) = \langle \hat{u}_i(x_i,t) \rangle = \frac{1}{2T} \int_{-T}^{T} \hat{u}_i(x_i, t+t')dt', \tag{1.7}$$

where T is an averaging time. It follows from Equation (1.7) that the fluctuations have zero mean,

$$\langle u_i'(x_i,t) \rangle = 0 \quad \text{and} \quad \langle p'(x_i,t) \rangle = 0. \tag{1.8}$$

Throughout this thesis when considering turbulent flow, Reynolds-averaged quantities are represented by upper-case (A) or overbars ($\overline{A}$), whereas fluctuating terms are represented by primes. Upon substitution of Equation (1.6) into Equation (1.2) & Equation (1.3) and after some algebra, the RANS equations are obtained (see [24] for a more detailed derivation):

$$\frac{\partial U_j}{\partial x_j} = 0, \tag{1.9}$$

$$\rho \frac{\partial U_i}{\partial t} + \rho U_j \frac{\partial U_i}{\partial x_j} = -\frac{\partial P}{\partial x_i} + \frac{\partial}{\partial x_j} \left(\mu_s S_{ij} - \rho \overline{u_i' u_j'} + \overline{\tau}_{ij,\mathrm{p}} \right), \tag{1.10}$$

where S_{ij} is the mean strain rate, $\overline{\tau}_{ij,\mathrm{t}} = -\rho \overline{u_i' u_j'}$ is the *Reynolds stress tensor*, and $\overline{\tau}_{ij,\mathrm{p}}$ is the mean polymer stress tensor — prescribed in later sections.

In RANS modelling, the governing equations require *closure* by replacing the fluctuating quantities with suitable models based on mean field quantities. For the Reynolds stress tensor, the objective is to capture the Reynolds stress components relevant to the physical system of interest. There are three main categories of RANS models (see [13] for more details):

- Linear eddy viscosity models (including algebraic models, one- and two-equation models)
- Non-linear eddy viscosity models (including an explicit nonlinear constitutive relation model and $v^2 - f$ model)
- Reynolds stress model (in which each Reynolds stress component is directly computed)

where those underlined are the focus of this thesis. This thesis will focus on *eddy viscosity models*. They are based on the Boussinesq hypothesis which presumes that there exists an analogy between the action of the viscous stresses and the Reynolds stresses on the mean flow:

$$-\rho\overline{u_i'u_j'} = \mu_t S_{ij} - \frac{2}{3}k\delta_{ij}, \tag{1.11}$$

where μ_t is the turbulent/eddy viscosity (or $\nu_T = \mu_T/\rho$ for kinematic eddy viscosity), and $k = \frac{1}{2}(\overline{u'^2} + \overline{v'^2} + \overline{w'^2})$ is the turbulent kinetic energy. Note that this relationship is linear (and thus a linear eddy viscosity model). More generally for non-linear models, this expression is given by

$$-\rho\overline{u_i'u_j'} = \mu_T F_{nl}(S_{ij}, \Omega_{ij}, ...), \tag{1.12}$$

where $\Omega_{ij} = \frac{1}{2}(\frac{\partial U_i}{\partial x_j} - \frac{\partial U_j}{\partial x_i})$ is the mean vorticity, and F_{nl} is some non-linear function dependent on turbulence variables. There are a variety of models available for ν_T depending on the features of a particular flow, or precision required for a given canonical system. There are two-equation models ($k-\varepsilon$ and $k-\omega$) along with a four-equation model ($k-\varepsilon-v^2-f$), to describe the eddy viscosity (not exclusively). This is accompanied by a transport equation for the turbulent kinetic energy, $k = \frac{1}{2}(\overline{u'^2} + \overline{v'^2} + \overline{w'^2})$, the rate of dissipation of turbulent kinetic energy, $\varepsilon = 2\nu\overline{s_{ij}' \cdot s_{ij}'}$, the specific dissipation rate $\omega = \varepsilon/k$, and the near wall scalar Reynolds stress scaling, v^2. In the context of the $v^2 - f$ model [25], the anisotropic wall effects are modelled through the elliptic relaxation function f, by solving a separate elliptic equation of the Helmholtz type via

$$f - L_t^2\nabla^2 f = \frac{1}{T_t}\left(\frac{2}{3}(C_1 - 1) - (C_1 - 6)\frac{\overline{v'^2}}{k}\right) + C_2\frac{P_k}{k}, \tag{1.13}$$

where $P_k = \overline{u_i'u_j'}\frac{\partial U_i}{\partial x_j}$ is the production term, the turbulent length scale,

$$L_t = C_L \max\left[\frac{k^{3/2}}{\varepsilon}, C_\eta\left(\frac{\nu_0^3}{\varepsilon}\right)^{1/4}\right], \tag{1.14}$$

and the turbulence time scale,

$$T_t = \max\left[\frac{k}{\varepsilon}, C_T\left(\frac{\nu}{\varepsilon}\right)^{1/2}\right]. \tag{1.15}$$

On dimensional grounds, we assume that the kinematic turbulent viscosity can be expressed as a product of a turbulent energy scale, ϑ [m^2/s], and a turbulent time scale, T_t [s] (one can also assume a turbulent velocity and length scale respectively),

$$\nu_T = C_\mu \vartheta T_t, \tag{1.16}$$

where C_μ is a dimensionless constant of proportionality. Table 1.1 shows the various scales used throughout this thesis. The term, f_μ, is a damping function to account for the near wall effects of turbulence.

RANS Model	Reynolds number regime	ϑ [m^2/s]	T_t [s]
$k-\varepsilon$	High	k	k/ε
	Low	$f_\mu k$	k/ε
$k-\omega$	High	k	$1/\omega$
	Low	$f_\mu k$	$1/\omega$
$k-\varepsilon-\overline{v^2}-f$	All	$\overline{v^2}$	$\max\left\{\frac{k}{\varepsilon}, 6\sqrt{\frac{\nu}{\varepsilon}}\right\}$

Table 1.1: Energy and time scales for eddy viscosity models used in this thesis.

1.2.2 Polymers

Modelling polymer chains in the context of drag reducing turbulent flows requires careful examination of the rheological features that need to be captured. In this thesis, we examine dilute homogeneous polymeric solutions which are polymer macromolecules in a solvent where the distance between each molecule is much greater than the molecule length.

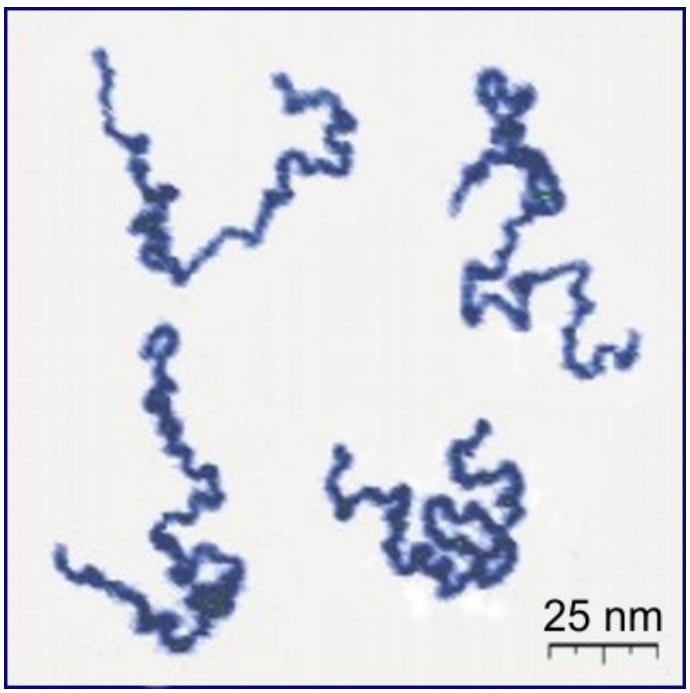

Figure 1.4: Real linear polymer chains. Recorded using an atomic force microscope on a surface, under liquid medium [26] [photograph by Yuri Roiter & Sergiy Minko, distributed under a CC BY-SA 3.0 license.]

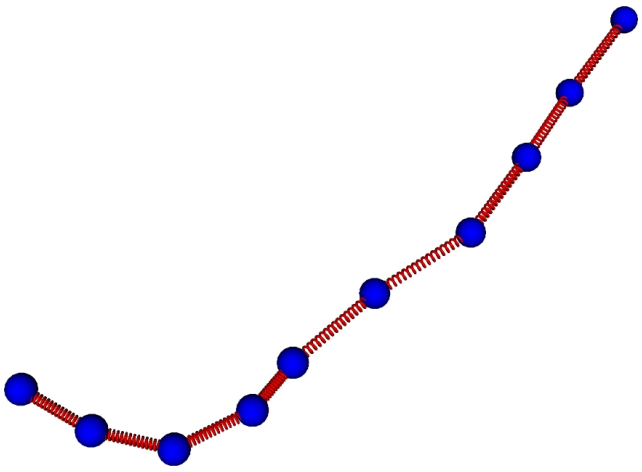

Figure 1.5: Polymer representation by $N = 10$ beads connected by non-linear springs.

An example of a real linear polymer chain can be viewed in Figure 1.4. Due to a polymers' complex molecular structure, it can have a broad range of time and length scales. Simulation techniques based on an atomistic representation of polymers, such as Monte-Carlo (MC) and molecular dynamics (MD), have been widely used to study polymers within DNA and proteins [27, 28]. However, the atomistic approach is very expensive and is suited more for understanding chemical interactions with solvent molecules. Further, MD and MC are only able to capture pico- to nano- seconds, and hence not suitable for hydrodynamics study.

To achieve the long time scales required for hydrodynamic fluid flow modelling, the atomistic approach is 'coarse-grained' to consider only the longer relaxation times of the polymer [29, 30]. One such coarse-grained application is the FENE model which stands for *Finitely Extensible Non-linear Elastic*. This uses beads to represent an inflexible monomer in the polymer chain and uses non-linear springs to model interactions between each bead. The coarse graining occurs by applying N beads such that for M monomers (typically $M = O(10^6 - 10^7)$), $N \ll M$ (Figure 1.5). However, introducing N beads, where N is substantial, means it is computationally expensive to integrate the FENE-N model into CFD solvers for turbulent hydrodynamic study.

A dumbbell version was introduced based on the statistical closures of Peterlin [31] (FENE-P), which models the polymers as a spring connected by two beads or end vectors. The polymer dynamics are then entirely described by the evolution of the two end vectors, which is represented by a conformation tensor defined as $\hat{c}_{ij} = \langle q_i q_j \rangle$. In a shear flow, the evolution of $\hat{c}_{ij}$ is governed by the stretching and restoring forces acting on the dumbbell (Figure 1.6). The FENE-P model is the closed version of the FENE-2 by defining the restoration force in terms of an average stretch. The restoring force is identically the polymer stress, so the evaluation of the configuration tensor provides a direct measure of the modelled polymer stress tensor. The definition of the instantaneous polymer

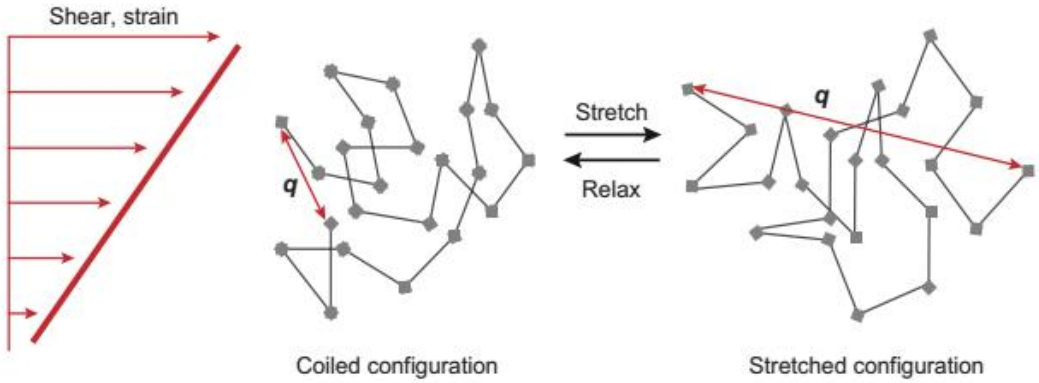

Figure 1.6: The end-to-end vector of the molecule is denoted as q. Schematic of polymer stretch (and relaxation) in shear flow. Polymer stretch is characterised by the change in q [32]. [Reprinted with permission from Christopher M. White and M. Godfrey Mungal, "Mechanics and Prediction of Turbulent Drag Reduction with Polymer Additives", Annu. Rev. Fluid Mech., **40**, 235–56 (2008). Copyright (2008) Annual Reviews.]

stress, $\hat{\tau}_{ik,\mathrm{p}}$, based on the FENE-P closure [29] is given as a function of the instantaneous conformation tensor $\hat{c}_{ij}$,

$$\hat{\tau}_{ij,\mathrm{p}} = \frac{\mu_p}{\lambda}\left(f(\hat{c}_{kk})\hat{c}_{ij} - f(L)\delta_{ij}\right), \tag{1.17}$$

with

$$f(\hat{c}_{kk}) = \frac{L^2-3}{L^2-\hat{c}_{kk}} \quad \text{and} \quad f(L) = 1, \tag{1.18}$$

where $\hat{c}_{kk}$ is the trace of the instantaneous conformation tensor, and the other parameters are associated to the rheological model: L^2 denotes the maximum molecular extensibility of the model dumbbell; λ is the relaxation time of the fluid and μ_p is the polymer viscosity coefficient. The instantaneous conformation tensor behaviour obeys the following hyperbolic differential equation:

$$\frac{\partial \hat{c}_{ij}}{\partial t} + \hat{u}_k\frac{\partial \hat{c}_{ij}}{\partial x_k} - \left(\hat{c}_{kj}\frac{\partial \hat{u}_i}{\partial x_k} + \hat{c}_{ik}\frac{\partial \hat{u}_j}{\partial x_k}\right) = \overset{\nabla}{\hat{c}}_{ij} = -\frac{\hat{\tau}_{ij,\mathrm{p}}}{\mu_p}. \tag{1.19}$$

The $\overset{\nabla}{\hat{c}}_{ij}$ term denotes Oldroyd's upper convective derivative of the instantaneous conformation tensor. The first two terms are the material derivative and represent the local and advective derivatives, and the terms in brackets account for the polymer stretching by the instantaneous flow.

The FENE-P model is one of few models that can be used in CFD since it removes statistical averaging at each grid point. However, due to its simplification, the FENE-P is not able to capture the hysteresis effects that the FENE model can. In order to capture the hysteresis effects, the FENE-LS model was developed [33]. The FENE-LS is more accurate in correcting the limitations of the FENE-P model to reproduce hysteresis behaviour

in strong flows involving stress growth and subsequent relaxation. However, the equations to model are much more numerically complex and have no suitable closure models for drag reducing flows [34]. The issue of whether the FENE-P model is an accurate representation of the FENE model for turbulent flow was studied by Zhou et al. [35], who concluded that the FENE-P is accurate only in the steady state, incurring large errors for transient flow. In this thesis, the DNS data for turbulent viscoelastic flows are time averaged — with the mean data taken as a steady state solution. The FENE-P can adequately capture important rheological parameters suitable for drag reducing flows (polymer relaxation time, λ, and viscosity ratio, $\beta = \nu_p/\nu_0$, and is relatively simpler to model than its FENE-N counterpart — a result of the lack of configurational degrees of freedom. The FENE-P model is the most widely used model for studying turbulent viscoelastic flows via DNS studies [15, 36] and will be the focus of this study.

Transport equations for a RANS FENE-P fluid

In earlier sections, the RANS prescription of a turbulent polymeric fluid was identified (Equation 1.9 and 1.10):

$$\frac{\partial U_j}{\partial x_j} = 0 \tag{1.20}$$

$$\rho \frac{\partial U_i}{\partial t} + \rho U_j \frac{\partial U_i}{\partial x_j} = -\frac{\partial P}{\partial x_i} + \frac{\partial}{\partial x_j}\left(\mu_s S_{ij} - \rho \overline{u_i' u_j'} + \overline{\tau}_{ij,\mathrm{p}}\right). \tag{1.21}$$

After applying Reynolds decomposition to Equations 1.17, 1.18, and 1.19, one obtains the mean polymer stress tensor

$$\overline{\tau}_{ij,\mathrm{p}} = \frac{\mu_p}{\lambda}\left[\overline{f(C_{kk}+c_{kk}')(C_{ij}+c_{ij}')} - f(L)\delta_{ij}\right], \tag{1.22}$$

and Reynolds averaged conformation evolution (RACE):

$$\frac{DC_{ij}}{Dt} - M_{ij} + CT_{ij} - NLT_{ij} = \frac{\overline{\tau}_{ij,\mathrm{p}}}{\mu_p}, \tag{1.23}$$

$$M_{ij} = C_{jk}\frac{\partial U_i}{\partial x_k} + C_{ik}\frac{\partial U_j}{\partial x_k}, \tag{1.24}$$

$$CT_{ij} = \overline{u_k' \frac{\partial c_{ij}'}{\partial x_k}}, \tag{1.25}$$

$$NLT_{ij} = \overline{c_{jk}' \frac{\partial u_i'}{\partial x_k}} + \overline{c_{ik}' \frac{\partial u_j'}{\partial x_k}}, \tag{1.26}$$

where M_{ij} is the mean flow distortion term, which is non-zero, but requires no closure. The remaining two terms are related to turbulent correlations and, following the analysis and nomenclature of Li et al. [15] and Housiadas et al. [37] are labelled with CT_{ij}, representing the contribution to the transport of the conformation tensor due to the fluctuating

advective terms, and NLT_{ij} which accounts for the interactions between the fluctuating components of the conformation tensor and the velocity gradient tensor.

The mean polymer stress tensor (Equation 1.22) can be represented with the following expansion:

$$\overline{\tau}_{ij,\mathrm{p}} = \underbrace{\frac{\mu_p}{\lambda}\left[f(C_{kk})C_{ij} - f(L)\delta_{ij}\right]}_{I} + \underbrace{\frac{\mu_p}{\lambda}\left[\overline{f(C_{kk}+c'_{kk})(C_{ij}+c'_{ij})} - f(C_{kk})C_{ij}\right]}_{II}. \quad (1.27)$$

The magnitude of terms I and II on the RHS of Equation (1.27) were analysed *a priori* using DNS data by Pinho et al. [38]. They showed that at different values of L^2 and Wi_{τ_0}, term I is nearly 20 times larger at LDR and HDR, regardless of the rheological parameters. In this work, the mean polymer stress is approximated by term I, as with other models [16, 39–41], hence given by

$$\overline{\tau}_{ij,\mathrm{p}} \approx \frac{\mu_p}{\lambda}\left[f(C_{kk})C_{ij} - f(L)\delta_{ij}\right]. \quad (1.28)$$

The CT_{ij} term (Equation 1.25) is omitted for all DR regimes following a budget analysis of the RACE carried out by Housiadas et al. [37] and Li et al. [15]. The NLT_{ij} term cannot be neglected since it is a significant contributor to the RACE and therefore requires a suitable closure.

The RANS FENE-P transport equations for k, ε and $\overline{v^2}$ contain fluctuating viscoelastic turbulent parts (see derivations in Appendix of [38]). For the k transport they are denoted:

$$Q^V = \frac{\partial \overline{\tau'_{ij,\mathrm{p}} u'_i}}{\partial x_j} \quad \text{and} \quad \varepsilon^V = \frac{1}{\rho}\overline{\tau'_{ij,\mathrm{p}}\frac{\partial u'_i}{\partial x_j}}, \quad (1.29)$$

which are the viscoelastic turbulent transport and the viscoelastic stress work, respectively. For the $\overline{v^2}$ transport they are analogous to Equation (1.29) but are the transverse counterparts $Q^V_{v^2}$ and $\varepsilon^V_{v^2}$, respectively. The viscoelastic contribution to the dissipation equation is denoted as,

$$E^V = 2\nu_s \overline{\frac{\partial u'_i}{\partial x_k}\frac{\partial}{\partial x_k}\left(\frac{\partial \tau'_{ij,p}}{\partial x_j}\right)} \quad (1.30)$$

The summary of the transport equations can be viewed in Table 1.2.

Equation	Φ	J_Φ	S_Φ
Mass Conservation	1	0	0
Momentum			
x-axis	U	$P\delta_{1j} - \overline{\tau}_{1j}$	0
y-axis	V	$P\delta_{2j} - \overline{\tau}_{2j}$	0
z-axis	W	$P\delta_{3j} - \overline{\tau}_{3j}$	0
Turbulent kinetic energy	k	- $\frac{\nu_T}{\sigma_k}\frac{\partial k}{\partial x_j}$	$P_k - \varepsilon + Q^V + \varepsilon^V$
Dissipation rate	ε	- $\frac{\nu_T}{\sigma_\varepsilon}\frac{\partial \varepsilon}{\partial x_j}$	$C_{\varepsilon 1}\frac{\varepsilon}{k}P_k - C_{\varepsilon 2}\frac{\varepsilon^2}{k} - E^V$
Turbulent wall scaling	$\overline{v^2}$	- $\frac{\nu_T}{\sigma_{v^2}}\frac{\partial \overline{v^2}}{\partial x_j}$	$kf - 6\frac{\varepsilon}{k}\overline{v^2} + Q^V_{v^2} + \varepsilon^V_{v^2}$

Table 1.2: Terms appearing in the governing transport equations (Equation (1.1)) for fully developed turbulent flow described by a RANS FENE-P model in Cartesian coordinates.

1.3 Literature review

1.3.1 Drag reduction and mechanisms

Predicting the behaviour of turbulent flows containing drag reducing polymer additives has been an active area of research since the experimental discovery of Toms et al. [10], who demonstrated that dilute solutions of flexible high-molecular weight polymers can drastically reduce the transport energy in channel flows. The logarithmic velocity profile in turbulent polymer flow increases with respect to turbulent Newtonian flow (Figure 1.7). The enhanced velocity profile reaches a maximum drag reducing (MDR) limit [42], up to 80%, where the addition of more polymers does not lead to a complete laminar flow state.

There is an acute difference in the near-wall turbulent structure between Newtonian and viscoelastic flows. The nature and strength of the vortices formed in the so-called buffer layer are altered as a result of polymer interactions with the fine-scale turbulence. Experimentally this has been performed using PIV [32] showing a reduction in the near wall vortex structures, leading to an increase in the high-speed velocity streaks (Figure 1.8).

The interaction between the fine-scale turbulence and the polymer induces an extensive elongation of the molecular chain which then has an impact on the turbulent energy cascade which reduces the drag. The resulting effect is a reduction in the turbulent shear stress contribution and thus a reduction in the pressure drop in channel flows. However, an underlying detailed physical mechanism for the dynamical interactions between polymers and turbulence has been an enigma for over 60 years. There are two divisions of argu-

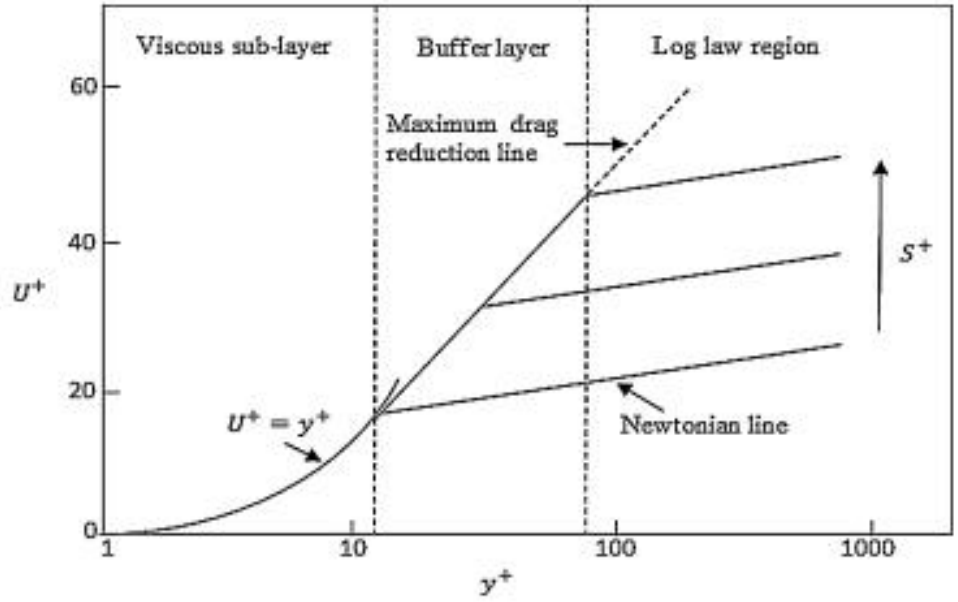

Figure 1.7: Semi-log plot of u^+ and y^+ from Abubakar et al. [43] showing with varying S^+ up to the maximum drag reduction line. [Reprinted with permission from A. Abubakar et al., "Roles of drag reducing polymers in single- and multi-phase flows", Chemical Engineering Research and Design **92**, 2153–2181 (2014). Copyright (2014) Elsevier.]

ments put forward over the years for the mechanisms of drag reduction; viscous effects, and more recently elastic effects. The basic premise of the viscous explanation is that the effect of polymer stretching in a turbulent flow produces an increase in the *effective viscosity* [44, 45]. The polymers are believed to be stretched in the buffer layer. In this region, the strain rate and vorticity fields are of suitable magnitude to cause full extension of the polymer, leading to an increase in effective viscosity and a suppression of the turbulent fluctuations [46]. Ryskin [47] derived an expression for the extensional viscosity as a function of polymer concentration and the maximum extensibility of a polymer solvent pair. For the elastic arguments, Virk's [48] extensive experimental data analysis introduced the concept of an elastic sublayer existing between the laminar sublayer and the logarithmic layer – were the author suggests that this layer plays a crucial role in drag reducing flows. Tabor & De Gennes [49] argue that the viscous theory cannot hold in a wall-bounded turbulent shear flow as the strain rates fluctuate in both space and time and can only produce partial stretching of the polymers. The elastic theory proposed postulates that the elastic energy stored by the partially stretched polymers is an important variable for drag reduction and the increase in the effective viscosity is small and inconsequential. The elastic theory predicts that the onset of drag reduction occurs when the cumulative elastic energy stored by the partially stretched polymers becomes comparable with the kinetic energy in the buffer layer at some turbulent length scale larger than the Kolmogorov scale. The turbulent energy cascade is then terminated prematurely, and scales below this cut-off behave elastically [50]. It is argued that these effects yield a

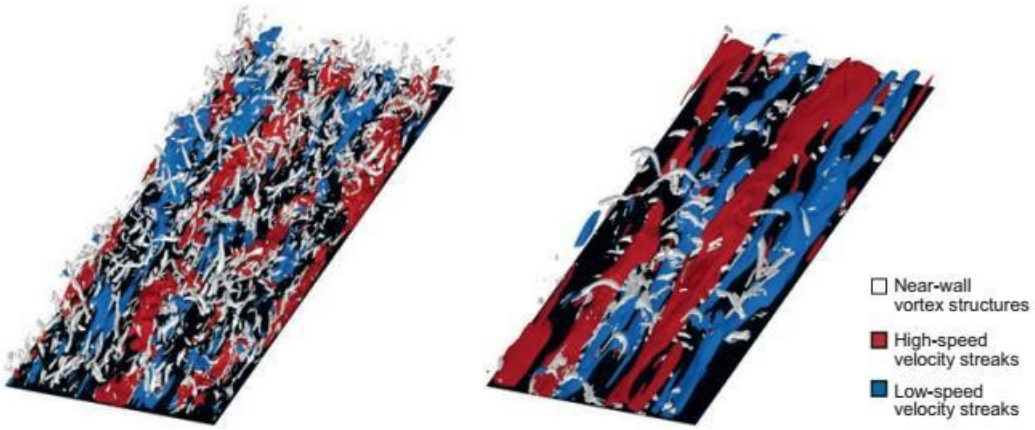

Figure 1.8: PIV of turbulent shear flow near the wall region captured by Dubief [32]: Newtonian fluid (left) and viscoelastic fluid of drag reduction 60% (right). [Reprinted with permission from Christopher M. White and M. Godfrey Mungal, "Mechanics and Prediction of Turbulent Drag Reduction with Polymer Additives", Annu. Rev. Fluid Mech., **40**, 235–56 (2008). Copyright (2008) Annual Reviews.]

thickened buffer layer and subsequent drag reduction.

Several DNS investigations were carried out with various rheological models [36, 51–56], along with experiments [57], to understand the complex interactions between the polymer chains and turbulent shears within channel flows, most notably with the FENE-P dumbbell constitutive model because of its molecular roots in kinetic theory [29, 58]. The FENE-P model can predict the effects on turbulent shear stresses via the polymer relaxation time, polymer chain extensibility and the polymer/solvent viscosity ratio. The numerical simulations concur that polymers disrupt the near wall turbulence and reduce the turbulent friction drag by directly interacting with and dampening the quasi streamwise vortices. The evidence for this is in two parts: the polymer body force ($\partial \tau_{ij,p}/\partial x_j$) in the momentum equation) opposes the motion of the vortices [55], and in turn; the polymer stress work (ε^V in the turbulent kinetic energy equation) transfers energy from the vortices to the polymers [57]. These forces are also accompanied by a substantial reduction in the velocity-pressure gradients in the Reynolds stress transport [59], leading to strong flow anisotropy. It is now accepted that drag reduction is strongly associated with the inhibition of near-wall turbulent vortical dynamics by the extensional motion of the polymer chains [60], inducing a redistribution of the turbulent energy scales and a global reduction in mean turbulent structures. This is essentially in agreement with the original proposals of Lumley [45].

1.3.2 Models for drag reducing turbulent channel flow

DNS is a great resource to explore the underlying mechanics of drag-reducing viscoelastic turbulent flows. However, for the majority of engineering motivations, DNS is not practical because of the high number of variables which requires a substantial expense of

memory and CPU-time. This cost is more significant in high DR (HDR) schemes in which the near-wall velocity streaks become more elongated, requiring an increased demand on computational resources.

The abundance of DNS data [16, 36, 54, 57, 61] for Reynolds-averaged quantities in fully-developed channel flow allows for the development of closure models, which substantially reduces the high CPU resource demands. This is ideal for engineering pursuits, and consequently Reynolds-Averaged-Navier-Stokes (RANS) turbulent viscoelastic models have been developed in order to capture important mean flow properties.

One of the original implementations of elastic effects within turbulence models was achieved by Pinho [62] and Cruz et al. [63, 64]. Their work focused on low-Reynolds number $k-\varepsilon$ turbulence models, applying a Generalised Newtonian Fluid (GNF) constitutive equation involving dependency of the fluid strain hardening on the third invariant of the rate of deformation tensor. Following these studies, an anisotropic version was also developed which included an increased Reynolds stress anisotropy [65], along with a Reynolds stress turbulence model [66], both able to satisfactorily predict drag-reducing behaviour. Nevertheless, the models are constrained because of the inelastic formulation of the GNF constitutive equations.

Further developments in viscoelastic RANS models became possible owing to the emergence of DNS data regarding turbulent viscoelastic fluids. The first elastic model was developed by Leighton et al. [67], which was based on the FENE-P dumbbell constitutive equation model. Their study involved the development of a polymer strain–stress coupling based on the tensor expansion, which incorporated the conformation tensor and Reynolds stress. From this work, more attention arose to the FENE-P model given the molecular roots of the equations. Later, based on *a priori* analysis of DNS data, Pinho et al. [38] developed a low-Reynolds number $k-\varepsilon$ model for FENE-P fluids which could predict flow features up to the low drag reduction regime (LDR $< 20\%$). Turbulent viscoelastic closures were proposed, including the non-linear term involving the conformation tensor and the strain rate fluctuations within the conformation tensor equation (denoted NLT_{ij} following the nomenclature of Housiadas et al. [37] and Li et al. [15]), along with the viscoelastic turbulent transport term of the turbulent kinetic energy. One of the key difficulties that arose in this initial study was the decrease in the magnitude of turbulent kinetic energy as viscoelasticity increased, opposite to that found in the DNS literature [61]. Subsequently, the model closures was improved by Resende et al. [68] and the capacity of the model predictions were extended to the intermediate drag reduction regime ($20\% <$ IDR $< 40\%$). However, the model closures involved complex damping functions and model constants which gave spurious results for the high drag reduction regime (HDR $> 40\%$). Resende et al. [41] applied the same viscoelastic closures to a low-Reynolds number $k-\omega$ model with only a mathematical transformation of the governing terms involving ω. The closures had identical limitations as the $k-\varepsilon$ model for predicting DR behaviour but demonstrated great versatility and robustness given its application to alternative two-

equation models.

During this time, a $k-\varepsilon-\overline{v^2}-f$ model for FENE-P fluids in fully developed channel flow was proposed by Iaccarino et al. [39], following the initial studies of Dubief et al. [60]. They introduced the idea of a *turbulent polymer viscosity* which accounts for the effects of viscoelasticity and turbulence on the polymer stress within the momentum equation. The reduction in the Reynolds shear stress is assumed by *a priori* DNS data analysis from the decreasing v^2 shown within the DNS studies [55]. The model closure for the NLT_{ij} is much simpler than the one developed by Resende et al. [68], but contains only the trace and not the individual components. The model was later improved by Masoudian et al. [16] and can predict flow features up to maximum DR (MDR). The key advancement of the closures were an NLT_{ij} closure based on DNS analysis and comparisons to the local eddy viscosity peaks; the viscoelastic stress work in the turbulent kinetic energy equations; viscoelastic stress in the momentum equation; and a viscoelastic destruction term in the dissipation transport equation. The viscoelastic turbulent closures within the v^2 equation (transverse viscoelastic stress work, ε^V_{yy}) should be strictly a function of NLT_{yy}, which is a key component in the formulation of an effective polymer viscosity. However, because only the trace of the NLT_{ij} term is present within the model, the closure had to be formulated using DNS analysis of alternative parameters.

After the above study, a second-order Reynolds stress model for FENE-P fluids was proposed by Masoudian et al. [69], extending on the idea of a correlation between the Reynolds stresses and the NLT_{ij} components, similar to Leighton et al. [67]. The model can predict all DR regimes but is generally unattractive due to the higher number of Newtonian terms resulting from higher-order modelling. Masoudian et al. [40] then further improved the $k-\varepsilon-\overline{v^2}-f$ model capabilities via the NLT_{ij} term by introducing a simple extension to include heat transfer, along with removing wall dependence via the friction velocity. There are concerning features when one examines the Boussinesq-type NLT_{ij} term, which has a zero NLT_{yy} component, along with an opposite sign for NLT_{xy}, both terms being crucial for the polymer shear stress in the momentum balance (see Appendix 1 in Pinho et al. [38]). Further, the increase of k in the buffer layer is small, meaning the decoupling of the v^2 component may not be enough to decrease the eddy viscosity. This is compensated by an opposite trend in the dissipation rate, ε, for increasing DR, which subsequently balances the momentum equations and causes the necessary increase in the velocity profiles.

Most recently, Resende et al. [70] improved upon the $k-\varepsilon$ model [68] via a modified damping function able to predict the turbulent redistribution process and thickening of the buffer layer. The correct increase of the turbulent kinetic energy was the first of the model's kind, achieved by analysing the production term behaviour near the wall [71], and by developing new eddy viscosity and NLT_{ij} closures using strictly DNS data [72]. In their work [70], they also improved significantly on the NLT_{ij} closure and incorporated small concentration variation via the solvent ratio. The model can predict most ranges

of DR well, but still requires complex un-physical modelling containing bulk Reynolds number and friction velocity dependence. This occurs predominately within the NLT_{xx} term which accounts for the dominant stretch of polymer chains from turbulent shear stresses, which fails at higher Reynolds numbers.

Earlier proposals of a modified damping function came from Pinho et al. [62] with a GNF model for the fluid; and Tsukahara et al. [73] with a Giesekus model. In the latter study, the turbulent kinetic energy was largely over-predicted which was compensated for by a lack of closure for the viscoelastic destruction term within the ε transport equation. In some instances, the model demonstrated instabilities, predicting a 1% DR for a DNS result of 23% DR.

Models for square ducts

Turbulent viscoelastic models for fully-developed channel flows are well documented, but numerical simulations for other canonical systems are scarce, with some recent work for turbulent viscoelastic jets [74], and square ducts [75]. There exists some experimental studies of polymer turbulent flows with a variety of polymers in the backwards facing step [76, 77]. However, there are currently no DNS studies with the FENE-P model for the backward facing step — therefore a complete validation of the closure model is difficult to obtain.

The enhanced streamwise features of turbulent polymer flows in square ducts are similar to those documented in channel flow, showing an increase in the mean velocity profile and thickening of the buffer layer, with a decrease in the wall normal Reynolds stresses [75]. One of the key features of Newtonian turbulent flow in square ducts (not present in channel flows) is the existence of secondary flow of the second kind [78], predominantly generated from the production of Reynolds stress gradients [79]. The secondary flow in the cross-stream plane gives rise to bending of the mean streamwise velocity isolines towards the duct corners [80], along with eight counter-rotating vortices. Although the intensity of the secondary motion is small compared to the streamwise motion (usually a few percent), it is generally assumed to have some important practical impact in redistributing friction and heat flux along the duct perimeter [81]

Early experimental studies on duct flow were carried out by Brundrett et al. [82] and Gessner et al. [83], detailing that the convection of mean streamwise vorticity plays a critical role within the vorticity balance. Gessner et al. [83] concluded that convection is one order of magnitude less than the other terms within the vorticity balance. Brundrett et al. [82] concluded that the secondary motion is not influenced by the Reynolds number, while Gessner et al. [83] found that the intensity diminishes with Reynolds number when scaled with the bulk speed and it remains nearly unaltered when scaled with the friction velocity. The same trend was observed for rough walls also by Launder et al. [84]. From the studies outlined, it appears that no firm conclusions have been drawn from experimental tests, thus DNS may be a valuable instrument to shed light on the role of

secondary flow.

Early experimental studies of polymers in square ducts reported limited measurements of mean turbulent flow data, with relatively low polymer concentrations and no reports on the secondary flow [85]. More recently, Escudier et al. [86] provided a more extensive database of experimental studies, showing limitations to the turbulent data collection at low polymer concentration — although the study does quantify the anisotropy of the Reynolds stresses.

In the presence of polymers, the reduction in the wall normal Reynolds stresses (or normal stress anisotropy) results in a shift of the maximum vorticity, moving towards the centre of the duct, according to DNS studies [75]. The vorticity behaviour is concurrent with the streamwise enstrophy budget in turbulent channel flows [59]. Predicting these features is of great interest for engineering purposes, and towards a more general viscoelastic turbulence model for more complex wall bounded flows.

Many attempts have been made to predict the secondary flow features of Newtonian turbulent square duct flow in the context of Reynolds Averaged Navier-Stokes (RANS) modelling. It is well known that classical isotropic eddy viscosity models fail to capture the self-sustained secondary motion [87]. This necessitated the use of non-linear eddy viscosity models (NLEVM) [88, 89], in which the Boussinesq hypothesis is extended to have higher order dependence on the strain and vorticity rates, based on the polynomial tensor basis of Pope [90]. More recently, Pecnik & Iaccarino [91] developed the isotropic $k-\varepsilon-v^2-f$ model of Lien et al. [92] to predict normal stress anisotropy, and thus secondary flow features. The model obeys the linear eddy viscosity hypothesis, whilst introducing a non-isotropic contribution, N_{ij}, based on the wall Reynolds stress scalar, v^2, without relying on additional nonlinear terms. Modesti [93] performed *a priori* DNS tests on eddy viscosity models by quantifying their accuracy in predicting the wall normal and shear Reynolds stress components in Newtonian turbulent square ducts. They concluded that the anisotropic v^2-f model performed best for both components, although it is not based on the nonlinear expansion [90].

1.3.3 Summary of literature, aims and objectives

The accuracy of the current $k-$ type models in fully developed channel flows is limiting, with dependence on the friction velocity and complex modelling. The need for a simple model in channel flows is paramount for the development of robust predictions in more complex geometries. This work aims to seek out reduced complexity for a $k-\varepsilon$ and $k-\omega$ model which can predict a larger range of flow features with good performance in channel flows. The modified damping function aims to mimic the anisotropic models, where the eddy viscosity is given as $\nu_t^{\text{ani}} \approx v^2/T_t$, and for isotropic models $\nu_t^{\text{iso}} \approx f_\mu k/T_t$. The aim is to have a simple ad-hoc model that does not require an additional transport equations, and to better capture the turbulent kinetic energy. The focus on a robust NLT_{ij} closure is highlighted, along with a modified dampening function able to capture the

reduced turbulent shear stresses in turbulent viscoelastic flow. Further, the first anisotropic $k-\varepsilon-v^2-f$ model is proposed for channel flows and square ducts. The model attempts to give more generality to duct flows with the developed closure models, by applying some principles from the current leading models. The code generated throughout is applied in OpenFOAM, with newly formulated boundary conditions for the conformation tensor.

1.4 Contributions of this thesis

- Chapter 2 develops OpenFOAM code within foamextend/4.0 which embeds the FENE-P model within the pre-existing turbulence framework via the RASModel class. This is accomplished by the conformation tensor equation being integrated as an 'effective' turbulence field in the source code, which can be solved alongside the additional turbulent transport equations (k, ε, ω, v^2, f). A newly defined transportProperties dictionary (named 'Viscoelastic' instead of 'Newtonian') is defined in the USER directory, which incorporates the polymer rheological properties (λ, L^2, ν_p) along side the pre-existing solvent viscosity (ν_s). A case file is generated for each model containing a developed geometry and mesh and finite volume schemes with the additional conformation tensor field. The boundary condition for the dissipation rate and conformation tensor is generated using the *groovyBC* functionality within the *swak4foam* library. DNS data of mean field values from independent sources are collated into CSV files and the rheological parameters associated with each unique case are listed. Python and Bash scripts are developed to facilitate series simulations of the listed DNS cases towards model testing and calibration. z

- Chapter 3 presents an improved $k-\varepsilon$ model for FENE-P fluids in fully developed channel flow. Closure models for the non-linear terms in the transport equations are developed via careful mathematical modelling, using *a posteriori* and *a priori* DNS data. The model includes a new damping function capable of mimicking the viscoelastic effects and reducing the eddy viscosity, along with a more robust formulation of the dominant NLT_{ij} component which captures the polymer stretching terms. All friction velocity dependence is removed which is crucial for the examination of more complex geometries. The model predicts a wide range of flow features found in the DNS data of turbulent viscoelastic channel flow such as: the conformation tensor components; eddy viscosity; turbulent kinetic energy; dissipation rate; and mean velocity profiles. The predictions span the whole range of rheological parameters available in the DNS literature (low, intermediate and high drag reduction). This includes friction Reynolds numbers ($Re_{\tau_0} = 125$ to $Re_{\tau_0} = 1000$); friction Weissenberg number ($Wi_{\tau_0} = 25$ to $Wi_{\tau_0} = 200$); and maximum extensibility of the dumbbell chain ($L^2 = 900$ to $L^2 = 14,400$).

- Chapter 4 describes a new $k-\omega$ model for FENE-P fluids in fully developed chan-

nel flow. The Newtonian model is adjusted to include the Van-driest type damping function developed in Chapter 3. The robustness of the damping function model is assessed with a sensitivity study and is shown to be stable. Viscosity ratio (β) variation is integrated within the model via the damping function and the polymer stretching term, where concentration changes are most effective. The model is tested for the full range of rheological parameters, similarly as Chapter 3, but along with a range of β variation ($\beta = 0.6, 0.8, 0.9$) within the confines of the FENE-P limitations. The model predicts well the flow features exhibited in the DNS, and has naturally more stability than the $k-\varepsilon$ counterpart.

- Chapter 5 presents an anisotropic $k-\varepsilon-v^2-f$ model for FENE-P fluids in fully developed channel and square duct flows. The model proposes a new closure for the NLT_{ij} term based on robust *a priori* DNS data, which redistributes the trace component, NLT_{kk}, to the streamwise component, NLT_{xx}, and transverse component, NLT_{v^2}, in a similar manner to the redistribution terms found in the normal Reynolds stress model of the Newtonian part — namely the mean vorticity direction, t_i, and wall normal direction, n_i. Simple *ad hoc* closure models are developed for the elliptic function, f, along with the spanwise Reynolds stress component. The model can predict flow features for low drag reduction in fully developed channel and square duct flow. This includes the conformation tensor stretching and shear terms; the Reynolds stress normal and shear components; the mean velocity and the bending of the isolines in square ducts; and shift of the mean vorticity centre towards the centre of the square duct for increasing viscoelasticity. The power of the model is the simplicity and robustness of the modelled non-linear terms, which are easily implemented into 3D codes like OpenFOAM, for future developments in more complex geometries.

Chapter 2

Numerical Procedure

2.1 OpenFOAM viscoelastic turbulence code

In this work, the open-source CFD software OpenFOAM is used. More specifically, the foam-extend.4.0 package is used. There are three mathematical concepts in determining the success of a case directory:

- Convergence - Case solutions approach the exact solution of the governing equations being modelled as the control volume is reduced to zero.
- Consistent - Numerical schemes produce systems of algebraic equations which can be demonstrated to be equivalent to the original governing equation as the control volume tends to zero.
- Stability - Damping of errors as the numerical method proceeds.

The governing equation central to the finite volume CFD method for steady state uses (1.1) in the integral form,

$$\underbrace{\int_A \hat{e}_i(\rho\Phi u_i)dA}_{\substack{\text{Convective transport} \\ \text{of } \Phi \text{ across boundaries}}} = \underbrace{\int_A \hat{e}_i(\Gamma\partial_i\Phi)}_{\substack{\text{Diffusive transport} \\ \text{of } \Phi \text{ across boundaries}}} + \underbrace{\int_{CV} S_\Phi dV}_{\substack{\text{Production or} \\ \text{destruction of } \Phi \\ \text{in control volume}}} , \tag{2.1}$$

where A is the bounding surface of a control volume (CV) and $\hat{e}_i$ is the ith component of the normal vector on the bounding surface.

The system of equations for viscoelastic turbulence presented in section (1.2.2) are developed with a new finite volume C++ computational code within the turbulence class structure. The choice of OpenFOAM is inspired by the fact that no turbulent viscoelastic class structure exists, that is widely available in new OpenFOAM builds. There is also limited availability in commercial CFD software. As turbulent viscoelastic models become more robust and readily available for complex geometries, a full scale integrated code is sought after by industry and research personnel. Turbulence itself is well founded in the context of OpenFOAM packages. More recently, laminar viscoelastic models have been integrated, along with RheoTool [94]. Previous codes in the context of turbulent viscoelastic models have been developed as FORTRAN codes by the group of Pinho et al. [38] exclusively for fully developed channel flow. Here we develop the code necessary to perform a full numerical analysis of the models adapted in subsequent chapters.

We begin our development with the simpleFOAM or pisoFOAM solver which is designed for incompressible flows with turbulence modelling. The momentum equation reads:

```
tmp<fvVectorMatrix> UEqn
  (
    fvm::ddt(U)
    + fvm::div(phi, U)
    + turbulence->divDevReff()
  );
    UEqn().relax();
    solve(UEqn() == -fvc::grad(p));
```

For steady state, fully developed flow, this is represented as

$$\frac{\partial P}{\partial x_i} = \frac{\partial \overline{\tau}_{ij}}{\partial x_j}. \tag{2.2}$$

The pointer 'turbulence→divDevReff()' represents the combined viscous and turbulent stress gradients, which are modelled within the src/turbulenceModels class structure. Under the RANS formulation, the source code for the standard $k-\varepsilon$ model (/incompressible/RAS/kEpsilon.C) is used as a starting position to add the viscoelastic effects. The idea here is that the viscoelastic effects can be thought of as an 'effective' turbulent field, or as a source term that opposes turbulence. The polymer shear stress is added to the momentum equation within the source code via the divDevReff() member function as:

```
tmp<fvVectorMatrix> MODEL::divDevReff() const
{
    return
    (
      - fvm::laplacian(nuEff(), U_)
      - fvc::div(nuEff()*dev(T(fvc::grad(U_))))
      - fvc::div(tauP_)
    );
}
```

The right-hand side of equation Equation (2.2) now reads as

$$\frac{\partial \overline{\tau}_{ij}}{\partial x_j} = \frac{\partial}{\partial x_j}\left(\underbrace{(\nu_s+\nu_T)}_{\text{nuEff()}} \frac{\partial U_i}{\partial x_j} + \underbrace{\frac{\nu_p}{\lambda}(f(C_{mm})C_{ij}-\delta_{ij})}_{\text{tauP}} \right). \tag{2.3}$$

The advantage of this approach is that the underlying solver does not need changing, because the polymer components are contained within divDevReff(). Adding the turbulence functionality to the laminar viscoelastic class structure was considered (i.e the opposite way). But because the turbulence structure is well founded within all OpenFOAM ver-

sions, the former was applied. The conformation tensor, C_{ij}, has its own transport equation which is added under the k and ε transport equations via

```
tmp<fvSymmTensorMatrix> CEqn
    (
        fvm::ddt(C_)
        + fvm::div(phi_, C_)
        - twoSymm(C_ & fvc::grad(U_))
        - NLT_
        - fvm::laplacian(kappa_, C_)
        ==
        - tauP_/nuP_
    );
CEqn().relax();
solve(CEqn);
```

This equation reads:

$$\frac{DC_{ij}}{Dt} - M_{ij} - NLT_{ij} - \kappa\frac{\partial^2 C_{ij}}{\partial x_k^2} = \frac{\overline{\tau}_{ij,\mathrm{p}}}{\nu_p}. \tag{2.4}$$

The models for NLT_{ij} and for all other closures are presented as constructors or private member functions within the code. An additional boundary condition is required with the introduction of the conformation tensor, as reported in later subsections.

The artificial diffusion term, $\kappa\partial_k^2 C_{ij}$, is added for numerical stability, where κ denotes a constant, isotropic, artificial numerical diffusivity. In earlier DNS studies [36, 56, 61], the dimensionless artificial numerical diffusivity is taken to be $\kappa/hu_\tau \sim O(10^{-2})$. A parametric study of a turbulent viscoelastic model performed in OpenFOAM, found that $\kappa \sim 10^{-3} - 10^{-5}$ [95]. This ensures the gradients are smoothed out sufficiently to not cause floating point errors, but does not have a large effect on mean velocity calculations.

To examine the sensitivity of κ, the model of Chapter 5 is tested with rheological parameters (DR=18%, Re_{τ_0}, $L^2 = 900$, $Wi_{\tau_0} = 25$), with ranging κ values $10^{-2} - 10^{-6}$. Table 2.1 shows the variations in DR%, $U^+_{\max}$, $k^+_{\max}$, $NLT^+_{\max}$ and $\kappa\frac{\partial^2 C_{mm}}{\partial x_k^2}$. From this $\kappa = 10^{-5}$ is applied throughout this thesis. The same conclusions can be drawn for the models within Chapter 3 and 4.

The FORTRAN code used by the group of Pinho [38], Resende [68, 70] and Masoudian et al. [16, 40], evaluates the analytic solution of FENE-P turbulence in fully developed channel flow ([38], Appendix 1), with no artificial diffusion required as the code is not finite volume.

κ	**DR%**	$U^+_{\mathbf{max}}$	$k^+_{\mathbf{max}}$	$NLT^+_{\mathbf{max}}$	$\kappa\frac{\partial^2 C_{mm}}{\partial x_k^2}$
10^{-6}	18.26	21.68	4.39	7.96	0.34
10^{-5}	18.26	21.68	4.39	7.96	3.35
10^{-4}	18.14	21.64	4.39	7.95	31.0
10^{-3}	17.01	21.48	4.40	7.75	292
10^{-2}	14.73	21.16	4.51	6.76	1170

Table 2.1: Sensitivity study with varying κ

2.2 Case set-up

Mesh generation and system of equations

To assess the performance of the models presented later in this thesis, a case is generated in the user run directory of OpenFOAM. The geometry and mesh are generated within the polyMesh directory using the blockMesh functionality. For both Newtonian and polymeric flows, a fixed pressure gradient (ex post facto [9]) is applied in the streamwise (x) direction, such that

$$\frac{\mathrm{d}P}{\mathrm{d}x} \equiv \frac{\Delta P}{\Delta x} = \frac{\langle \tau_w \rangle}{R_h}, \tag{2.5}$$

where $R_h = A_h/P_h$ is the hydraulic radius, A_h is the cross-sectional area of the geometry, P_h is the 'wetted' perimeter, and $\langle \tau_w \rangle$ is the average wall shear stress. For channel flow, $R_h = 4h^2/4h = h$, where h is the channel half-height. For square duct flow, $R_h = 4h^2/8h = h/2$. Here h is set to 1 for simplicity. The mesh generated for the channel has a symmetry plane at the centre-line (middle) $y = h = 1$, and at both $y = h = 1$ and $z = h = 1$ for the square duct (Figure 2.1). A total of 50 cells are assigned in the wall normal directions with approximately 10 cells located inside the viscous sub-layer ($y^+ \sim 10$). This ensures mesh independence as shown in [16].

Assigning the fixed pressure drop a value of $1/R_h$ allows for easier calculations — with wall friction $u_{\tau_0} = 1$, and $h = 1$, the dimensionless field parameters become:

$$\begin{aligned} &y^+ = y \cdot Re_{\tau_0}, \quad U^+ = U, \quad k^+ = k, \quad \varepsilon^+ = \frac{\varepsilon}{Re_{\tau_0}}, \quad \overline{v^2}^+ = \overline{v^2}, \\ &NLT^+_{ij} = \frac{NLT_{ij}}{Re_{\tau 0}}, \quad C^+_{ij} = C_{ij}, \quad \overline{\tau}^+_{ij,\mathrm{p}} = \frac{1-\beta}{Wi_{\tau_0}}\overline{\tau}_{ij,\mathrm{p}}, \end{aligned} \tag{2.6}$$

where subscript τ_0 means zero-shear rate value. The rheological parameters that determine a unique DNS data set are the friction Reynolds number, $Re_{\tau_0} = hu_\tau/\nu_0$, the friction

Weissenberg number, $Wi_{\tau_0} = \lambda u_\tau^2/\nu_0$, the ratio of solvent to total viscosity, β, and the maximum extension of the dumbbell model, L^2. A new transport properties dictionary is built within OpenFOAM to account for fluid rheology based on these terms. The dictionary mimics the 'viscosityModel/Newtonian' class, but here renamed 'viscosityModel/Viscoelastic' with the definitions:

$$\nu_0 = \frac{1}{Re_{\tau_0}}, \quad \lambda = \frac{Wi_{\tau_0}}{Re_{\tau_0}}, \quad \beta, \quad L^2. \tag{2.7}$$

Combinations of the 4 rheological and flow parameters give a unique DNS data case. A bash script with 'for loops' is written to run each case in series with the variable named $DR[\nu_0, \lambda, \beta, L^2]$. For example, case 5 could be DNS data for 37% drag reduction at $Re_{\tau_0} = 395$. This would lead to the 5th element of DR to be: $DR[4] = [1/395,\ 100/395,\ 0.9,\ 900]$.

The estimation of the DR% of a case is given by [96]

$$DR(\%) = 1 - (\nu_0)^{2(1-n)/n} \left(\frac{U_{\max}^{+(V)}}{U_{\max}^{+(N)}} \right)_{Re_{\tau_0}}^{-2/n}, \tag{2.8}$$

where $n = 1.148$, with $U_{\max}^{+(N)}$, and $U_{\max}^{+(V)}$ representing the maximum (bulk) value at Re_{τ_0} for Newtonian turbulence and polymeric turbulence, respectively.

Boundary conditions

For wall bounded turbulent channel flow under a RANS description, the boundary conditions are well studied [13]. For our simulations, the inlet and outlet boundaries have a fixed gradient pressure field with Equation (2.5), and is generated using the 'fan' condition.

```
boundaryField
{
    inletoutlet
    {
    type fan;
    patchType cyclic
    f        (-0.1); // (Delta x / R_h)
    jump     uniform -0.1; // (Delta x / R_h)
    }
}
```

All other fields have a cyclic condition. The boundary conditions imposed on the solid wall include a no-slip (or zero) velocity field U, along with the turbulent kinetic energy, k, set to zero (or very small, $\sim 10^{-10}$ to ensure no floating point errors). The eddy viscosity, ν_T, is also set to zero by using the nutLowReWallFunction. This functionality is

a place holder which allows one to ascertain the first cell distance to ensure $y_w^+ \sim 1$. The boundary condition for the dissipation rate, ε, is given by the asymptotic relationship, $\varepsilon_w = 2\nu_s \left(\frac{\partial \sqrt{k}}{\partial x_i}\right)^2$. This conditions is generated using the groovyBC functionality via:

```
boundaryField
{
    wall
    {
    type groovyBC;
    valueExpression
    "2*nu*internalField(k)/sqr(mag(delta()))";
    value    uniform 1e-10;
    }
}
```

The conformation tensor, C_{ij}, in the governing equations necessitates an additional boundary condition. This can be achieved by a zero-gradient Neumann condition. However, this approach can lead to numerical instability if the near-wall values are not constant. The best option within the literature is a Dirichlet condition that accounts for the analytic laminar solution in the near wall region [39, 97]. This condition is not readily available within the OpenFOAM software and so the following proceeds to create a novel boundary condition file.

The laminar form of Equation (2.4) is given by,

$$C_{jk}\frac{\partial U_i}{\partial x_k} + C_{ik}\frac{\partial U_j}{\partial x_k} = \frac{1}{\lambda}\left(f(C_{kk})C_{ij} - \delta_{ij}\right). \tag{2.9}$$

Within the laminar sublayer (or very near-wall), the velocity gradient has a linear form such that $U^+ = y^+$, where $U^+ = \frac{U}{u_\tau}$ and $y^+ = \frac{y u_\tau}{\nu_w}$. Here U is the mean velocity, y is the wall distance, u_τ is the friction velocity and ν_w is the wall viscosity. With the knowledge that $\frac{dU^+}{dy^+} = 1$, the individual components (xx, yy, zz, xy) of Equation (2.4) after some algebra become,

$$2Wi_\tau C_{xy}^{lam} = \left(f(C_{kk}^{lam})C_{xx}^{lam} - 1\right), \tag{2.10}$$

$$0 = \frac{1}{\lambda}\left(f(C_{kk}^{lam})C_{yy}^{lam} - 1\right), \tag{2.11}$$

$$0 = \frac{1}{\lambda}\left(f(C_{kk}^{lam})C_{zz}^{lam} - 1\right), \tag{2.12}$$

$$Wi_\tau C_{yy}^{lam} = f(C_{kk}^{lam})C_{xy}^{lam}, \tag{2.13}$$

where $Wi_\tau = \frac{\lambda u_\tau^2}{\nu_w}$ is the friction Weissenberg number, and '*lam*' refers to the laminar region $0 < y^+ < 5$ in which these equations hold. After some algebra and substitutions,

one finds the following cubic equation for $f(\equiv f(C_{kk}^{lam}))$:

$$f^3 - f^2 - \frac{2Wi_\tau^2}{L^2} = 0. \tag{2.14}$$

This admits one real solution, f_R, such that

$$\boxed{f_R = \frac{1}{3}\left(\frac{B}{2^{1/3}} + \frac{2^{1/3}}{B} + 1\right)} \tag{2.15}$$

with

$$B = (A + ((A+2)^2 - 4)^{1/2} + 2)^{1/3} \quad \text{and} \quad A = 54(Wi_\tau/L)^2, \tag{2.16}$$

and satisfies the laminar sublayer equations:

$$\boxed{\begin{aligned} C_{xx}^{lam} &= \frac{1}{f_R}\left(\frac{2Wi_\tau^2}{f_R^2} + 1\right) && \text{(2.17a)} \\ C_{yy}^{lam} &= \frac{1}{f_R} && \text{(2.17b)} \\ C_{zz}^{lam} &= \frac{1}{f_R} && \text{(2.17c)} \\ C_{xy}^{lam} &= \frac{Wi_\tau}{f_R^2} && \text{(2.17d)} \end{aligned}}$$

Note that the dependence of these wall conditions are with Wi_τ and L^2 only, given that $f_R \equiv f_R(Wi_\tau, L^2)$. Equation 2.14 can be rearranged in the form

$$f^2(f-1) = \frac{2Wi_\tau^2}{L^2}. \tag{2.18}$$

One can observe that as $\frac{Wi_\tau}{L} \to 0$, $f \to 1$. Note that $f \geq 1$ because the elasticity and maximum extensibility of the dumbbell model are strictly positive. Physically, this means that the polymer coil reaches equilibrium as the elasticity over polymer length (or elastic line density) approaches zero. Equations 2.17 are developed within OpenFOAM under the *swak4Foam* library using the *groovyBC* functionality developed by Gschaider [98], viz:

```
boundaryField
{
    wall
    {
    #include "$FOAM_CASE/constant/transportProperties"
    type groovyBC;

```

```
        variables (
        "dudy@wall=dudy;"
        "tauPw@wall=tauPw;"
        "utau2=($[(dimensionedScalar)nu]+tauPw)*dudy;"
        "WiTau=$[(dimensionedScalar)lambda]*dudy;"
        "L=$[(dimensionedScalar)L];"
        "A=54*pow(WiTau,2)/L;"
        "B=pow((A+pow((pow((A+2),2)-4),1/2)+2),1/3);"
        "fR=(1/3)*((B/pow(2,1/3))+(pow(2,1/3)/B)+1);"
        );
        valueExpression
        "symmTensor((2*pow(WiTau/fR,2)+1)/fR, WiTau/pow(fR,2),
            0, 1/fR, 0, 1/fR)";
        value    uniform (0 0 0 0 0 0);
    }
}
```

The summary of the boundary conditions are found are Table 2.2

Field	**Boundary**			
	Inlet	Outlet	Wall	Middle
P	$P_{out} = P_{in} + \Delta P$		$n_i \partial_i P = 0$	$\partial_i P = 0$
U	$U(x_{in}) = U(x_{in} + \Delta x) \equiv U(x_{out})$		0	$\partial_i U = 0$
k	$k(x_{in}) = k(x_{in} + \Delta x) \equiv k(x_{out})$		10^{-10}	$\partial_i k = 0$
ε	$\varepsilon(x_{in}) = \varepsilon(x_{in} + \Delta x) \equiv \varepsilon(x_{out})$		$2\nu_s \left(\frac{\partial \sqrt{k}}{\partial x_i}\right)^2$	$\partial_i \varepsilon = 0$
ω	$\omega(x_{in}) = \omega(x_{in} + \Delta x) \equiv \omega(x_{out})$		$\frac{2\nu_s}{C_\mu y^2}$	$\partial_i \omega = 0$
v^2	$v^2(x_{in}) = v^2(x_{in} + \Delta x) \equiv v^2(x_{out})$		10^{-10}	$\partial_i v^2 = 0$
f	$f(x_{in}) = f(x_{in} + \Delta x) \equiv f(x_{out})$		10^{-10}	$\partial_i f = 0$
C_{ij}	$C_{ij}(x_{in}) = C_{ij}(x_{in} + \Delta x) \equiv C_{ij}(x_{out})$		Equation (2.17)	$\partial_i C_{ij} = 0$

Table 2.2: Summary of the boundary conditions used in the numerical simulations. Subscript *in* and *out* is defined as the inlet and outlet patch, respectively. Δp is the pressure drop specified, which for our set-up simplifies to be $\Delta P = |\Delta x|$.

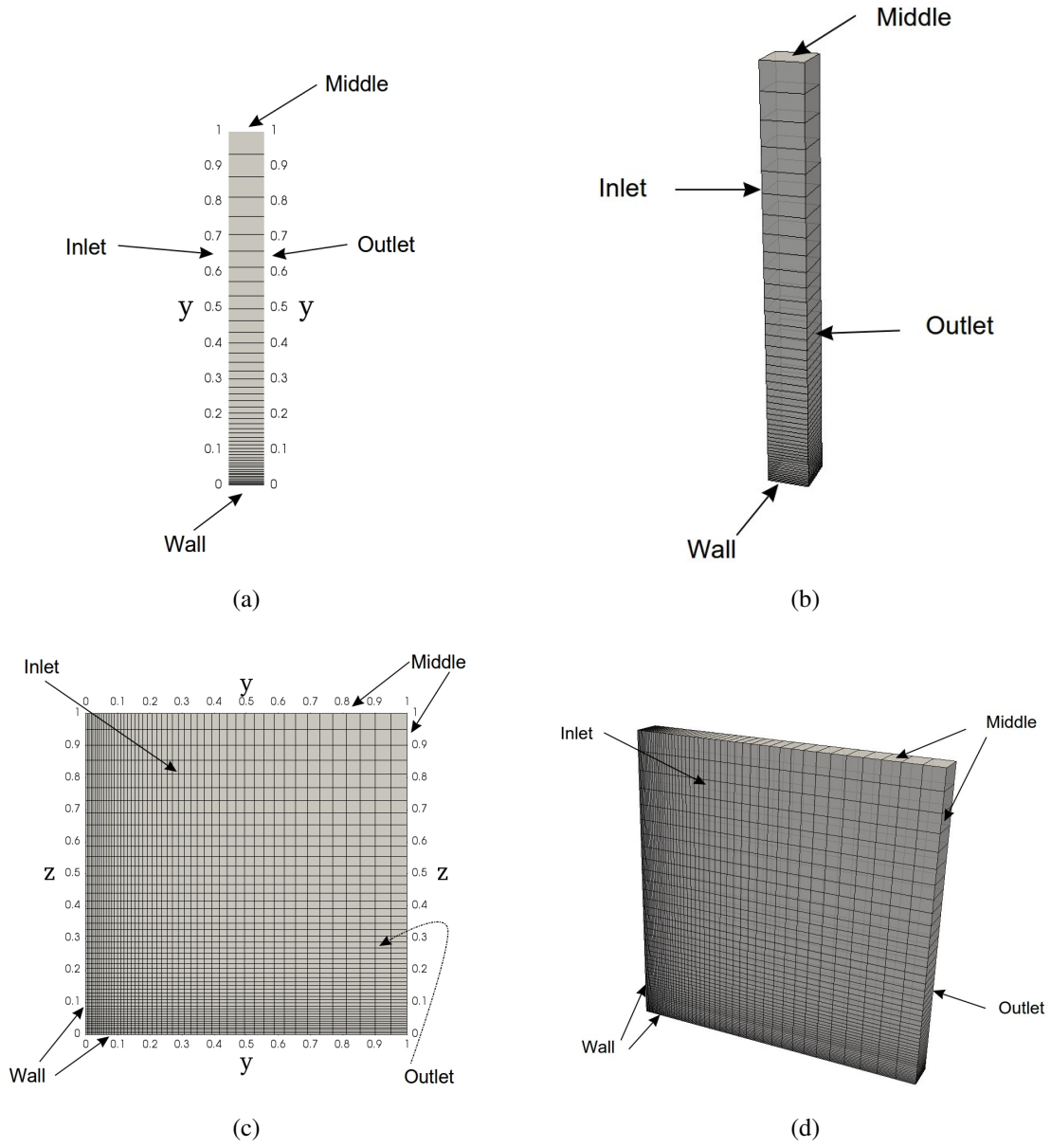

Figure 2.1: Computational domain and mesh for (a, b) channel ($x-y$ plane), and (c, d) square duct ($y-z$ plane). Figures (b, d) show an isometric view of the channel and square duct, respectively.

Chapter 3

A FENE-P $k-\varepsilon$ Viscoelastic Turbulence Model Valid up to High Drag Reduction without Friction Velocity Dependence

3.1 Introduction

In the present chapter, an new $k-\varepsilon$ model for FENE-P fluids is proposed, which improves on the previous models reviewed in chapter 1. The model is validated for all drag reduction regimes (low, intermediate, high) and up to the largest friction Reynolds number ($Re_{\tau_0} = 1000$) available in the DNS data. The important contributions to the current model are an improved and simplified NLT_{ij} term that removes complexity from the most recent model developed by Resende et al. [70]; along with a modified damping function which accurately predicts the viscoelastic contributions near and away from the wall, effectively reducing the eddy viscosity and thickening the buffer-layer as DR increases. Further, a reformulation of the viscoelastic contribution to the dissipation equation, E^V, is developed. The model is assessed against DNS data covering a wide range of flow conditions in terms of the friction Weissenberg number, Wi_{τ_0}, maximum polymer extension, L^2, viscosity ratio, β, and friction Reynolds number, Re_{τ_0}; along with comparisons against other turbulent FENE-P models within the literature. The main advantage is the capacity to predict all flow fields for low, intermediate and high friction Reynolds numbers, up to high drag reduction without friction velocity dependence.

This chapter is organised as follows: Section 3.2 introduces the instantaneous and time-averaged governing equations and identifies the viscoelastic terms that will require modelling; Section 3.3 explains in detail the development of the viscoelastic turbulent closures; Section 3.4 summarises the model; Section 3.5 presents the numerical procedure applied; Section 3.6 presents the results of the flow fields in fully developed channel flow, covering all range of DR and flow conditions; and finally in Section 3.7, the main conclusions are presented. The work developed in this chapter has been published in [99].

3.2 Governing Equations

The incompressible RANS equations for a FENE-P fluid were formulated in section 1, and are here summarised for the context of this chapter.

The Reynolds-averaged continuity and momentum equations are respectively:

$$\frac{\partial U_j}{\partial x_j} = 0, \tag{3.1}$$

$$\rho\frac{\partial U_i}{\partial t} + \rho U_j\frac{\partial U_i}{\partial x_j} = -\frac{\partial P}{\partial x_i} + \frac{\partial}{\partial x_j}\left(\mu_s S_{ij} - \rho\overline{u_i' u_j'} + \overline{\tau}_{ij,\mathrm{p}}\right), \tag{3.2}$$

where

$$\overline{\tau}_{ij,\mathrm{p}} = \frac{\mu_p}{\lambda}\left[f(C_{kk})C_{ij} - f(L)\delta_{ij}\right]. \tag{3.3}$$

and Reynolds averaged conformation evolution (RACE):

$$\frac{DC_{ij}}{Dt} - M_{ij} - NLT_{ij} = \frac{\overline{\tau}_{ij,\mathrm{p}}}{\mu_p}, \tag{3.4}$$

$$M_{ij} = C_{jk}\frac{\partial U_i}{\partial x_k} + C_{ik}\frac{\partial U_j}{\partial x_k}, \tag{3.5}$$

$$NLT_{ij} = \overline{c'_{jk}\frac{\partial u'_i}{\partial x_k}} + \overline{c'_{ik}\frac{\partial u'_j}{\partial x_k}}. \tag{3.6}$$

3.2.1 Model for the Reynolds Stress Tensor

The Reynolds stress tensor is computed by adopting the Boussinesq turbulent stress strain relationship,

$$-\rho\overline{u'_i u'_j} = 2\rho\nu_T S_{ij} - \frac{2}{3}\rho k\delta_{ij}, \tag{3.7}$$

where k is the turbulent kinetic energy, S_{ij} is the mean rate of strain tensor and $\mu_T = \rho\nu_T$ is the eddy viscosity. ν_T is modelled by the typical isotropic $k-\varepsilon$ turbulence model for low Reynolds numbers, which includes a damping function f_μ to account for near-wall effects:

$$\nu_T = C_\mu f_\mu \frac{k^2}{\tilde{\varepsilon}^N}, \tag{3.8}$$

where $\tilde{\varepsilon}^N = \nu_s\overline{\frac{\partial u_i}{\partial x_j}\frac{\partial u_i}{\partial x_j}}$ is the viscous dissipation of k by the Newtonian solvent. The damping function, f_μ, requires additional modelling to capture the anisotropy of the drag reducing flow as a result of viscoelastic flow effects — to be discussed further in this thesis. In the limit of zero Weissenberg number,

$$f_\mu \to \left[1 - \exp\left(-\frac{y^+}{a_\mu}\right)\right]^2, \tag{3.9}$$

and $a_\mu = 26.5$. The dimensionless wall scaling is $y^+ = u_{\tau_0} y/\nu_0$, where u_{τ_0} is the friction velocity, y is the distance to the nearest wall, and ν_0 is the sum of solvent and polymer viscosity coefficients ($\nu_0 = \nu_s + \nu_p$).

3.2.2 Transport Equation for the Turbulent Kinetic Energy

The governing transport equation for the turbulent kinetic energy of turbulent flow with FENE-P fluids is given by,

$$\begin{aligned}\rho\frac{\partial k}{\partial t} + \rho U_i\frac{\partial k}{\partial x_i} =& \rho\frac{\partial}{\partial x_i}\left[\left(\nu_s + \frac{f_t\nu_T}{\sigma_k}\right)\frac{\partial k}{\partial x_i}\right] + P_k - \rho(\tilde{\varepsilon}^N + D) \\ &+ Q^V - \rho\varepsilon^V,\end{aligned} \tag{3.10}$$

with

$$D = 2\nu_s \left(\frac{d\sqrt{k}}{dx_i} \right)^2 . \tag{3.11}$$

$P_k = -\rho \overline{u_i' u_j'} \frac{\partial U_i}{\partial x_j}$ is the rate of production of k.

The Newtonian closures of Equation (3.10) are those present in the Nagano et al. [100, 101] models. To increase numerical stability, a modified Newtonian rate of dissipation of k is applied instead of the true dissipation, which are related by $\varepsilon^N = \tilde{\varepsilon}^N + D$. For better model performance and to correct for the turbulent diffusion near walls, a turbulent variable Prandtl number is added of the form, $f_t/\sigma_k = 1 + 3.5\exp(-(Re_T/150)^2)$ with $Re_T = k^2/(\nu_s \tilde{\varepsilon})$ and model constant $\sigma_k = 1.1$. More details of the form of Equation (3.10) can be found in Pinho et al. [38] and Resende et al. [68].

The last two terms on the right side of the Equation (3.10) are:

$$Q^V = \frac{\partial \overline{\tau_{ij,\mathrm{p}}' u_i'}}{\partial x_k} \quad \text{and} \quad \varepsilon^V = \frac{1}{\rho} \overline{\tau_{ij,\mathrm{p}}' \frac{\partial u_i'}{\partial x_j}}, \tag{3.12}$$

which are the viscoelastic turbulent transport and the viscoelastic stress work, respectively. They represent the fluctuating viscoelastic turbulent part of the k transport equation and require suitable closure models.

A budget analysis for each term in the k transport equation was performed by Pinho et al. [38] for different regimes of DR. They demonstrated that the magnitude of Q^V has more impact on the overall budget in the intermediate drag reduction (IDR) regime, and also developed a closure. In the HDR, the amplitude of Q^V is the same as ε^V but has a different location in the buffer layer, in which the effects of Q^V are overcome by turbulent diffusion, thus, revealing negligible effects to overall flow predictions. Masoudian et al. [16] had chosen to neglect the Q^V contributions in the $k-\varepsilon-v^2-f$ model and is also not included here as well.

3.2.3 Transport Equation for the Rate of Dissipation of Turbulent Kinetic Energy

The corresponding governing transport equation for the modified Newtonian rate of dissipation of k is given by,

$$\begin{aligned} \rho \frac{\partial \tilde{\varepsilon}^N}{\partial t} + \rho U_i \frac{\partial \tilde{\varepsilon}^N}{\partial x_i} =& \rho \frac{\partial}{\partial x_i} \left[\left(\nu_s + \frac{f_t \nu_T}{\sigma_\varepsilon} \right) \frac{\partial \tilde{\varepsilon}^N}{\partial x_i} \right] + f_1 C_{\varepsilon_1} \frac{\tilde{\varepsilon}^N}{k} P_k \\ & - f_2 C_{\varepsilon_2} \rho \frac{(\tilde{\varepsilon}^N)^2}{k} + \rho E - E^V , \end{aligned} \tag{3.13}$$

with

$$E = \nu_s \nu_T (1 - f_\mu) \left(\frac{\partial^2 U_j}{\partial x_i \partial x_k} \right)^2 . \tag{3.14}$$

As mentioned in the previous sub-section, all terms are modelled in the Newtonian context (excluding E^V). The damping functions of Equation (3.13) are $f_1 = 1$ and $f_2 = 1 - 0.3\exp(-(Re_T)^2)$; with model coefficients $\sigma_\varepsilon = 1.3$, $C_{\varepsilon_1} = 1.45$ and $C_{\varepsilon_2} = 1.90$.

The last term in Equation (3.13) is the viscoelastic contribution to the overall $\tilde{\varepsilon}^N$ balance, given by

$$E^V = 2\nu_s \overline{\frac{\partial u_i'}{\partial x_k} \frac{\partial}{\partial x_k} \left(\frac{\partial \tau_{ij,p}'}{\partial x_j} \right)}, \tag{3.15}$$

It has non-negligible effects on flow predictions for all DR regimes and thus requires a suitable model.

3.3 Development of Viscoelastic Closures

In this section, the turbulent viscoelastic cross-correlations that were isolated in the previous section are presented with model closures. The closures are developed on the basis of the DNS data case (19) (Table 3.1), and then subsequently compared with other DNS data sets for accurate model predictions. The DNS data in Table 3.1 pertain to all DR regimes with a large variation in rheological parameters and fluid viscosity for fully-developed channel flow established by: Li et al. [61]; Thais et al. [54, 102]; Masoudian et al. [16, 40, 103] and Iaccarino et al. [39].

The non-dimensional numbers that define the different DNS data sets are defined as follows: the friction Reynolds number $Re_{\tau_0} = hu_\tau/\nu_0$ is based on the friction velocity (u_τ), the channel half-height (h), the zero shear-rate kinematic viscosity of the solution, which is the sum of the kinematic viscosity of the solvent and polymer ($\nu_0 = \nu_s + \nu_p$); The Weissenberg number $Wi_{\tau_0} = \lambda u_\tau^2/\nu_0$; and the ratio between the solvent viscosity and the solution viscosity at zero shear rate is $\beta = \nu_s/\nu_0$.

In the following sub-sections, closures are developed for: the NLT_{ij} term of Equation (1.23) with focus on the dominant NLT_{xx} component; a modification of the damping function f_μ (Equation (3.9)), named f_ν, which accounts for the reduction of the Reynolds shear stress due to viscoelastic effects; the viscoelastic stress work, ε^V of Equation (3.10); and the viscoelastic contribution to the dissipation equation (3.13), E^V.

Case	Reference	Rheological parameters			Drag reduction (%)		
		Re_{τ_0}	Wi_{τ_0}	L^2	DNS	Current Model	Model [70]
(1)	Li et al. [61]	125	25	900	19	20	-
(2)	Li et al. [61]	125	25	3600	22	23	-
(3)	Li et al. [61]	125	25	14400	24	25	-
(4)	Li et al. [61]	125	50	900	31	30	35
(5)	Li et al. [61]	125	100	900	37	36	39
(6)	Li et al. [61]	125	100	1800	45	43	-
(7)	Li et al. [61]	125	100	3600	56	51	51
(8)	Masoudian et al. [16]	180	25	900	19	19	-
(9)	Li et al. [61]	180	50	900	31	30	34
(10)	Masoudian et al. [16]	180	100	900	38	38	39
(11)	Masoudian et al. [16]	180	100	3600	54	53	51
(12)	Thais et al. [102]	180	116	10000	64	60	-
(13)	Iaccarino et al. [39]	300	36	3600	33	32	34
(14)	Iaccarino et al. [39]	300	36	10,000	35	35	32
(15)	Iaccarino et al. [39]	300	120	10,000	59	59	58
(16)	Masoudian et al. [40]	395	25	900	19	22	19
(17)	Masoudian et al. [40]	395	50	900	30	30	-
(18)	Masoudian et al. [40]	395	50	3600	38	38	-
(19)	Masoudian et al. [40]	395	100	900	37	37	38
(20)	Masoudian et al. [40]	395	100	3600	48	47	52
(21)	Masoudian et al. [103]	395	100	10000	55	55	-
(22)	Masoudian et al. [40]	395	100	14,400	61	60	62
(23)	Thais et al. [102]	395	116	10,000	62	60	-
(24)	Li et al. [61]	395	200	14,400	75	69	67
(25)	Masoudian et al. [40]	590	50	3600	39	40	64
(26)	Thais et al. [102]	590	116	10,000	61	59	74
(27)	Thais et al. [54]	1000	50	900	30	33	60

Table 3.1: Independent DNS data for turbulent channel flow of FENE-P fluids at $\beta = 0.9$, with DR model predictions.

3.3.1 Closure for NLT_{ij}

The NLT_{ij} exact transport equation is greatly simplified based on the DNS analysis of Pinho et al. [38]: Following the transport equation of $\overline{f(\hat{c}_{mm})c'_{kj}\frac{\partial u'_i}{\partial x_k}} + \overline{f(\hat{c}_{mm})c'_{ik}\frac{\partial u'_j}{\partial x_k}}$, it is assumed that

$$\overline{f(\hat{c}_{mm})c'_{kj}\frac{\partial u'_i}{\partial x_k}} + \overline{f(\hat{c}_{mm})c'_{ik}\frac{\partial u'_j}{\partial x_k}} \approx f(C_{mm})\left(\overline{c'_{kj}\frac{\partial u'_i}{\partial x_k}} + \overline{c'_{ik}\frac{\partial u'_j}{\partial x_k}}\right) = f(C_{mm})NLT_{ij}. \quad (3.16)$$

The full details of this approximation and the exact transport equation of NLT_{ij} can be found in Pinho et al. [38] and Resende et al. [68].

The complete closure of NLT_{ij} is presented below and was developed to improve model predictions based on better physical modelling compared with the most recent

model developed by Resende et al. [70].

$$\begin{aligned} NLT_{ij} &= \overline{c'_{kj}\frac{\partial u_i}{\partial x_k}} + \overline{c'_{ik}\frac{\partial u'_j}{\partial x_k}} \\ &\approx \underbrace{f_N C_{N1}\frac{\lambda\sqrt{\tilde{L}}\varepsilon^N}{\nu_0 f(C_{mm})}\delta_{ij}}_{I} - \underbrace{f_N^{1/4} C_{N2} M_{ij}}_{II} + \underbrace{C_{N3}\frac{k}{\nu_0}\sqrt{\frac{\tilde{L}M_{nn}}{\gamma}}\frac{\frac{\partial U_i}{\partial x_k}\frac{\partial U_j}{\partial x_k}}{\gamma^2}}_{III}, \end{aligned} \tag{3.17}$$

where $f_N = \nu_T/\nu_0$ is the local eddy viscosity, $\gamma = \sqrt{2S_{ij}S_{ij}}$ is the shear rate invariant, $\tilde{L} = \sqrt{L^2/900}$ is the normalised maximum extension with the lowest DR, with model constants $C_{N1} = 0.11$, $C_{N2} = 0.3$ and $C_{N3} = 0.3$.

The closure of Equation (3.17) is modelled in three parts: parts *I* and *II* are modelled in the same fashion as the model of Resende et al. [70], part *III* is greatly improved and is the main contribution to the NLT_{ij} closure.

Term 1 has adjustments $L^{0.42}$ to $\sqrt{L}$ and $f(C_{mm})^{0.8}$ to $f(C_{mm})$ for improved DR predictions.

Term *II* is primarily responsible for capturing the shear component, NLT_{xy}. The correlation here is with the exact term, M_{ij} (see Equation (1.24)), and by the local eddy viscosity, $f_N^{1/4}$. The $L^{0.15}$ variation is removed from the model developed by Resende et al. [70]. The negative part of the NLT_{xx} component is also captured here via the M_{xx} term, which according to Dubief et al. [60], is the region where polymers inject energy into turbulence.

Term *III* is developed to predict the NLT_{xx} component which is the dominant term in the trace of NLT_{ij}, responsible for the stretch of the polymer chains due to turbulent fluctuations. Following the same assumption as Masoudian et al. [69], one can see that $NLT_{xx} \sim \overline{u'_x u'_x} \sim k$. In physical terms, the turbulent stretching terms represent the ability of the turbulent fluctuations to act on the polymer chains. This stretching is effective if the polymer shear and maximum extensibility are large enough. So, $\sqrt{\tilde{L}M_{nn}/\gamma}$ is included here with k. Note that for fully developed channel flow, this term reduces to $\sqrt{\tilde{L}C_{xy}}$ which increases proportionally with drag reduction. This new term includes the same physical assumption as Masoudian et al. [16, 40], and is simplified from the very complex *ad hoc* approach of Resende et al. [70], viz

$$\begin{aligned} NLT_{III}^{\text{Resende}} =& f_N^{0.9}\exp\left(-\frac{-f_N}{1.05\sqrt{\beta}(10+0.3L+\tilde{L}-(\tilde{L}-1)^2)}\right) \\ &\times\left(\frac{C_{mm}}{(\beta/0.9)^{0.7\beta}}\left(2-\left[1-\exp\left(-\frac{2U_b h/\nu_s}{3500}\right)\right]^4\right)\right)^{0.7}\frac{\frac{dU_i}{dx_k}\frac{dU_j}{dx_k}}{\sqrt{\frac{dU_p}{dx_q}\frac{dU_p}{dx_q}}}. \end{aligned} \tag{3.18}$$

The performance of the NLT_{ij} closure can be analysed in Figure 3.1 by comparing the predictions with DNS data case (19) in Table 3.1, and with the model of Resende et al. [70]. Figure 3.1a–c plots each normal component of NLT_{ij}, with the predictions as accurate as the previous model [70]. The new NLT_{xx} component is capable of predicting the maximum value and peak location of the destruction effect away from the wall along with the negative part near the wall, but requires a much simpler closure. The NLT_{yy} component is the leading order term in the C_{yy} component away from the wall, which is the dominant contributor to an effective polymeric viscosity. This strongly influences the turbulent dynamics according to Thais et al. [20] and Benzi et al. [104] with their DNS and toy model analysis respectively. This term is represented by the first term in Equation (3.17), along with NLT_{zz}. The NLT_{zz} component was shown by Pinho et al. [38] to have low impact in channel flows. This term only takes part in the trace of NLT_{ij}, which is dominated by the streamwise component where polymer stretching occurs. Benzi [104] characterises an ordering of each C_{ij} term such that $C_{xx} \sim 1/\Delta$, $C_{xy} \sim O(1)$, and $C_{yy} = C_{zz} \sim \Delta$ — where Δ is some small number. Given this, $NLT_{zz} = NLT_{yy}$ is an appropriate approximation. The shear component, NLT_{xy}, can be viewed in Figure 3.1e, where the predictions are similar compared with the previous model [70], but do not require additional L^2 variation via $L^{0.15}$.

Simulations are ran in series for each case in Table 3.1, with initial estimates of the model constants using model [70]. The model is calibrated for case 19 (DR=37%) and then examined for low (case 16, DR=18%) and high (case 20, DR=48%) DR at the same Re_{τ_0}(=395). More tests are performed to calibrate the model for the range of Re_{τ_0}.

Overall, all main features of NLT_{ij} are well captured such as the peak locations and magnitudes, but with a much simpler closure for the dominant contributor of polymer stretch, NLT_{xx}. Further, the NLT_{xy} and NLT_{yy} terms responsible for the polymer shear stress contribution in the momentum balance are featured, which were previously represented *ad hoc* with friction velocity dependence [16, 39] or misrepresented [40].

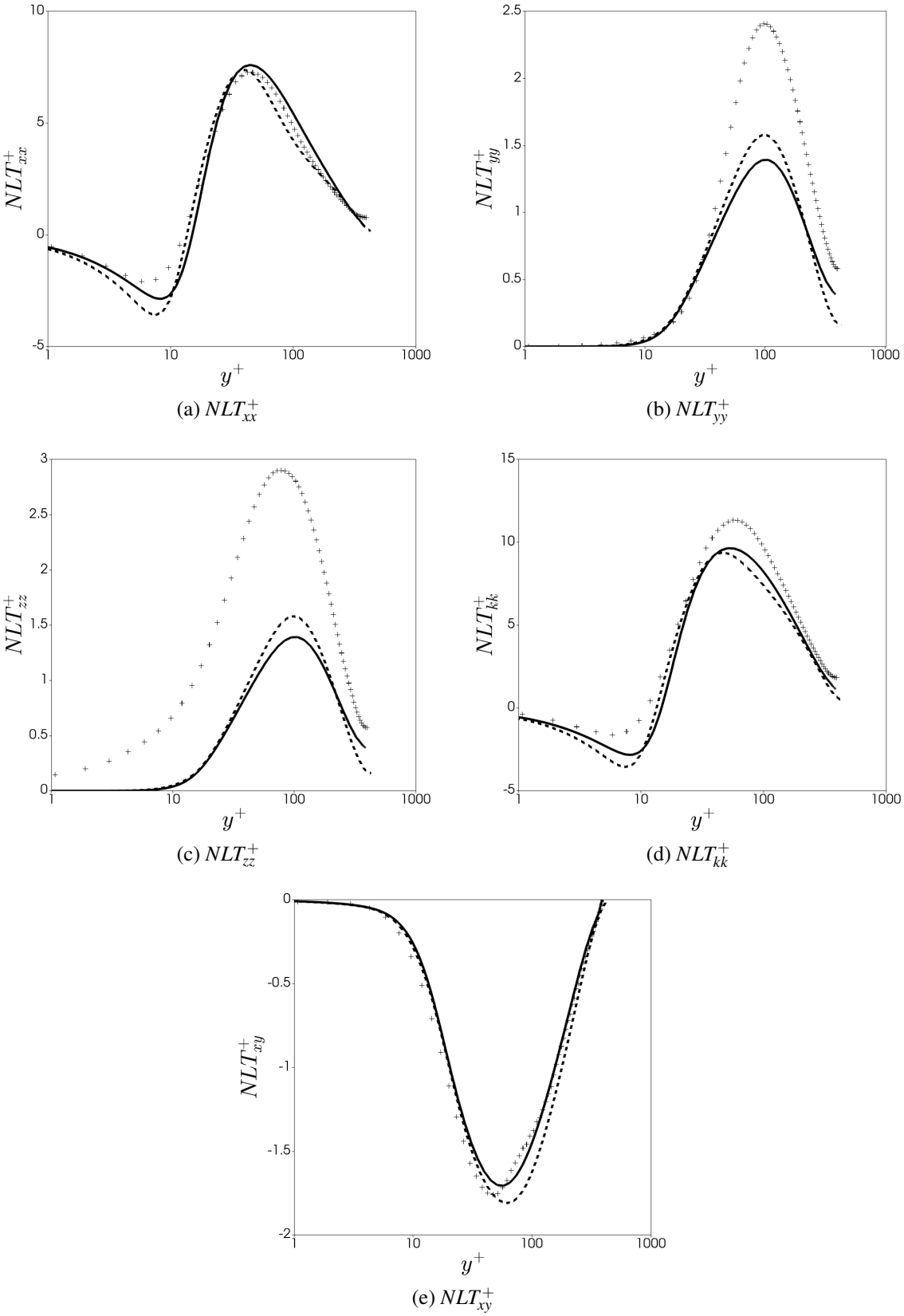

(a) NLT^+_{xx} (b) NLT^+_{yy}

(c) NLT^+_{zz} (d) NLT^+_{kk}

(e) NLT^+_{xy}

Figure 3.1: Comparison of the NLT_{ij} model between DNS data (+DR = 37%, case (19)) and predictions with the new model (continuous lines), and previous model [70] (dash lines).

3.3.2 Model for the Modified Damping Function, f_v

There have been many attempts to predict the eddy viscosity reduction as flow viscoelasticity increases for drag-reducing flows. In the case of low-Reynolds $k-\varepsilon$ models for FENE-P fluids, this was examined firstly by Pinho et al. [38] for the LDR regime; then later by Resende et al. [68] for the IDR regime. In both cases, there was a consistent reduction in the magnitude of k as DR increased, contrary to the DNS findings [61]. Similar attempts to model a modified damping function were made by Pinho [62], Cruz et al. [64] and Resende et al. [65] using the GNF model; along with Tsukahara and Kawaguchi [73] using the Giesekus model.

Recently, Resende et al. [70] proposed a modified damping function which was able to predict the correct behaviour of the eddy viscosity close to the wall, leading to the appropriate increase for the magnitude of k, and the shift away from the wall into the buffer layer as DR increased. This proposal was founded from the *a priori* DNS data analysis by Resende et al. [72], demonstrating the necessary increase to the production of k close to the wall. The model derived by Resende et al. [70] is based on the DNS analysis of Li et al. [61], with an approximation of the form $DR \sim C_{kk}/L$, giving rise to the correct damping of near-wall eddies as DR increases. In the $k-\varepsilon-v^2-f$ models proposed by Iaccarino et al. [39] and Masoudian et al. [16], the near-wall eddy viscosity damping effect is achieved by v^2, as $\nu_T = C_\mu v^2 k/\varepsilon$. However, the reduction in v^2 is not enough to increase k as given by the DNS data.

The approach by Resende et al. [70] works well in increasing k in the buffer layer, but fails to capture the viscoelastic effects away from the wall, due to the fact that $f_\mu^{\text{Previous}} \to 1$ as $y \to h$, which is contrary to the DNS data of Li et al. [15] and the analogous behaviour of v^2 away from the wall. Therefore an additional model is required to capture the effect of non-equilibrium away from the wall, similarly to the Newtonian model of Park et al. [105]. Benzi et al. [104] demonstrated that the overall effect of polymer stretching is to introduce an effective viscosity proportional to C_{yy}, which is dominated by the NLT_{yy} component (modelled here with the first term in Equation (3.17)). An additional term is multiplied to the eddy viscosity to account for the global reduction of eddy structures for increasing DR. This approach is similar to the model of Resende et al. [68] and the study using DNS data of Resende et al. [72] which multiplies the damping function by a factor of $1-g(\text{VE})$, where $g(\text{VE})$ is a function of the viscoelastic terms, VE.

The final model presented for the modified damping function, f_v, is

$$f_v = (1-A)\left[1-\exp\left(-\frac{y^*}{a_\mu\left(1+B/a_\mu\right)}\right)\right]^2, \tag{3.19}$$

$$A = C_A\left(f_N\frac{\lambda^2\tilde{L}^{3/2}}{f(C_{kk})^2}\frac{\varepsilon}{\nu_0}\right)^{0.3}, \tag{3.20}$$

$$B = C_B(C_{kk} - 3)^{1.25}/L, \tag{3.21}$$

with model constants $C_A = 0.071$ and $C_B = 0.44$. An additional contribution in the present model comes from an alternative representation of the dimensionless wall scaling $y^+ = y(u_\tau/\nu_0)$, where y is the wall distance dependence. The presence of the wall friction velocity poses a problem for flows with re-circulation or reattachment were the friction velocity becomes null at these points, causing floating point errors within computational solvers. Possibilities other than y^+ that solve this issue are $Re_y \equiv \sqrt{k}y/\nu_0$ or the turbulent Reynolds number, Re_t. Wallin and Johansson [106] formulated an alternative scaling, y^*, in terms of Re_y so that $y^* \approx y^+$ for $y^+ \leq 100$ in channel flows. The form proposed is

$$y^* = C_{y1}Re_y^{1/2} + C_{y2}Re_y^2, \tag{3.22}$$

where $C_{y1} = 2.4$ and $C_{y2} = 0.003$. The Re_y-term is motivated by the fact that the near-wall asymptotic behaviour for $Re_y^{1/2}$ is $\sim y^2$. The Re_y^2-term is artificially introduced to obtain a near linear relation in the buffer region.

The performance of the f_ν closure can be analysed in Figure 3.2 by comparing the predictions with DNS data cases (16, 19, 20) for LDR, IDR and HDR respectively in Table 3.1 and with the model of Resende et al. [70]. The predictions offer significant improvement away from the wall compared to the previous model. The effects can be viewed for the turbulent kinetic energy and the eddy viscosity in the results section, offering improved results for various levels of DR and Reynolds numbers. The f_ν closure more accurately represents the anisotropic effect akin to the $v^2 - f$ models of Masoudian et al. [16, 40], with the thickening of the buffer layer from the stretched polymers, along with a global reduction of the eddy viscosity with the new closure.

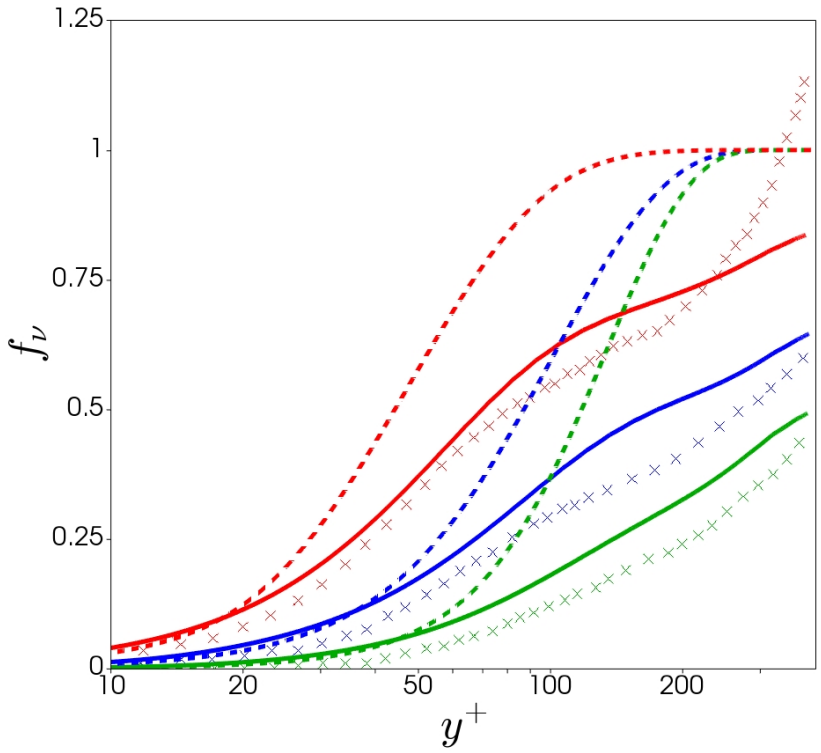

Figure 3.2: Comparison of the f_ν model between DNS data ($\times$ crosses) and predictions with the new model (continuous lines), and previous model (dash lines): each colour represents a different drag reduction regime: red (low drag reduction (LDR), case 16); blue (intermediate drag reduction (IDR), case 19); green (high drag reduction (HDR), case 20).

3.3.3 Development of Closures for ε^V and E^V

The viscoelastic stress work, ε^V, can be expressed as

$$\varepsilon^V = \frac{\nu_p}{\lambda}\left[\overline{C_{ij}f(C_{mm}+c'_{mm})\frac{\partial u'_i}{\partial x_j}} + \overline{c'_{ij}f(C_{mm}+c'_{mm})\frac{\partial u'_i}{\partial x_j}}\right]. \tag{3.23}$$

Pinho et al. [38] verified that in LDR, the triple correlations above can be decoupled into a double correlation and product of $f(C_{kk})$, which is $NLT_{kk}/2$. This was later confirmed for IDR and HDR by Resende et al. [68] and Masoudian et al. [16], respectively. Therefore the viscoelastic stress can be approximated by,

$$\varepsilon^V_{kk} = \varepsilon^V \approx \frac{\nu_p}{2\lambda} f(C_{mm}) NLT_{kk}. \tag{3.24}$$

This approximation is well founded and is applied in other models [16, 40, 70]. Masoudian et al. [16] confirmed the model capabilities within 5% accuracy for all DR regimes via an extensive pdf (probability density function) study.

Figure 3.3 shows the normal components of $\varepsilon^V_{ij} \approx \frac{\nu_p}{2\lambda} f(C_{mm}) NLT_{ij}$ for LDR and HDR.

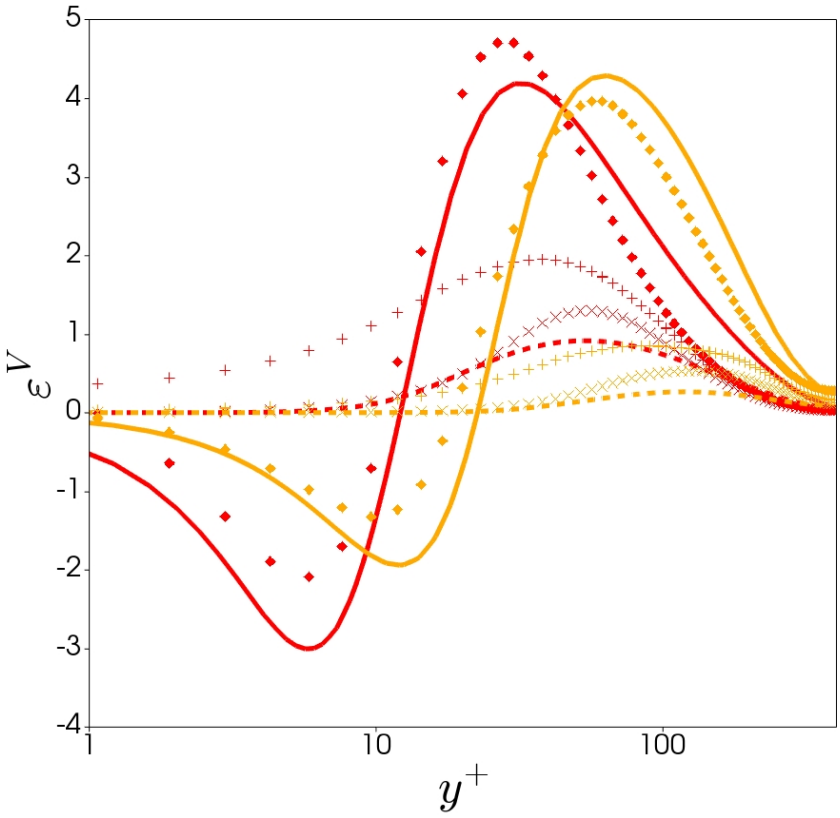

Figure 3.3: Comparison of the ε^V normal components between DNS data (xx : $\diamond$, yy : $\times$, zz : $+$) and model predictions (xx : solid line, yy and zz : dashed line): each colour represents a different drag reduction regime: red (LDR, case 16); orange (HDR), case 22).

The ε^V_{xx} component is the dominant contribution for the viscoelastic transport of k, demonstrating here the shift of the buffer layer as DR increases. The ε^V_{yy} and ε^V_{zz} are equated from the NLT_{ij} closure, which show a reasonable trend, although under-predicted.

The closure model derived for E^V assumes that it depends on the same quantities as the classical Newtonian destruction term of the transport equation of ε, but involving a viscoelastic quantity, typically with the viscoelastic stress work used by Resende et al. [68, 70] and Masoudian et al. [16, 40]. However, as ε^V contains a negative part close to the wall via the NLT_{kk} contribution, it is not feasible to include ε^V in a suitable model for E^V, based on the DNS analysis of ε being strictly decreasing near the wall for increasing DR.

The closure derived by Resende et al. [70] is complex with Wi_{τ_0} dependence to force the correct trend in ε. Here, a much simpler approach is obtained with dependence through k and some viscoelastic quantities which increases proportional with DR. The closure is given by

$$E^V \approx -C_{N4}\frac{\tilde{\varepsilon}^N}{k}\left[\nu_p\sqrt{C_\mu f_\mu}\tilde{L}^{3/4}\left(\frac{k}{\nu_0}\right)^2\right], \tag{3.25}$$

with model constant $C_{N4} = 0.083$. The effect of Equation (3.25) on ε predictions can be viewed in the results section for LDR and HDR.

Overall, it is clear that all the developed viscoelastic closures presented in this study perform well compared with DNS data. Most importantly, this was achieved without the use of friction velocity dependence and reduced complexity as presented in [70]. The simplicity of the governing closures allows easy implementation into 3D codes. The model is untested for the backwards facing step and DNS data for that system is not available. Examination of the model constants and applicability of the closures would need to follow.

3.4 Summary of the new $k-\varepsilon$ model

The governing equations with complete closure models that were developed in the previous sections are presented here.

Momentum equation:

$$\rho\frac{\mathrm{D}U_i}{\mathrm{D}t} = -\frac{\partial P}{\partial x_i} + \rho\frac{\partial}{\partial x_j}\left[(\nu_s+\nu_T)\frac{\partial U_i}{\partial x_j}\right] + \rho\frac{\partial}{\partial x_j}\left(\frac{\nu_p}{\lambda}\left[f(C_{mm})C_{ij}-\delta_{ij}\right]\right), \tag{3.26}$$

where the eddy viscosity is given by

$$\nu_T = C_\mu f_\nu \frac{k^2}{\varepsilon^N}, \tag{3.27}$$

with modified damping function

$$f_\nu = (1-A)\left[1-\exp\left(-\frac{y^*}{a_\mu\left(1+B/a_\mu\right)}\right)\right]^2, \tag{3.28}$$

$$A = C_A\left(f_N\frac{\lambda^2\tilde{L}^{3/2}}{f(C_{kk})^2}\frac{\varepsilon}{\nu_0}\right)^{0.3}, \tag{3.29}$$

$$B = C_B(C_{kk}-3)^{1.25}/L, \tag{3.30}$$

with constants $a_\mu = 26.5$, $C_A = 0.071$ and $C_B = 0.44$. y^* is given by Equation (3.22).

Conformation tensor equation:

$$\frac{\mathrm{D}C_{ij}}{\mathrm{D}t} - M_{ij} - NLT_{ij} = -\frac{1}{\lambda}[f(C_{kk})C_{ij}-\delta_{ij}], \tag{3.31}$$

with

$$NLT_{ij} \approx f_N C_{N1} \frac{\lambda \sqrt{\tilde{L}} \varepsilon^N}{\nu_0 f(C_{mm})} \delta_{ij} - f_N^{1/4} C_{N2} M_{ij} + C_{N3} \frac{k}{\nu_0} \sqrt{\frac{\tilde{L} M_{nn}}{\gamma}} \frac{\frac{\partial U_i}{\partial x_k} \frac{\partial U_j}{\partial x_k}}{\gamma^2}, \tag{3.32}$$

where $f_N = \nu_T / \nu_0$ is the local eddy viscosity, $\gamma = \sqrt{2 S_{ij} S_{ij}}$ is the shear rate invariant, $\tilde{L} = \sqrt{L^2/900}$ is the normalised maximum extension with the lowest DR, with model constants $C_{N1} = 0.11$, $C_{N2} = 0.3$ and $C_{N3} = 0.3$.

Transport equation of k:

$$\rho \frac{\mathrm{D}k}{\mathrm{D}t} = \rho \frac{\partial}{\partial x_i} \left[\left(\nu_s + \frac{f_t \nu_T}{\sigma_k} \right) \frac{\partial k}{\partial x_i} \right] + P_k - \rho(\tilde{\varepsilon}^N + D) - \frac{\nu_p}{\lambda} f(C_{mm}) \frac{NLT_{kk}}{2}, \tag{3.33}$$

where $P_k = -\rho \overline{u_i' u_j'} \frac{\partial U_i}{\partial x_j}$ is the rate of production of k.

Dissipation transport equation:

$$\begin{aligned} \rho \frac{\mathrm{D}\tilde{\varepsilon}^N}{\mathrm{D}t} =& \rho \frac{\partial}{\partial x_i} \left[\left(\nu_s + \frac{f_t \nu_T}{\sigma_\varepsilon} \right) \frac{\partial \tilde{\varepsilon}^N}{\partial x_i} \right] - f_2 C_{\varepsilon_2} \rho \frac{(\tilde{\varepsilon}^N)^2}{k} + \rho E \\ &+ \left(C_{\varepsilon_1} P_k - C_{N4} \nu_p \sqrt{C_\mu f_\mu} \tilde{L}^{3/4} \left(\frac{k}{\nu_0} \right)^2 \right) \frac{\tilde{\varepsilon}^N}{k}, \end{aligned} \tag{3.34}$$

with model constant $C_{N4} = 0.083$.

The remaining constants are from the Newtonian model and are $C_{\varepsilon_1} = 1.45$, $C_{\varepsilon_2} = 1.90$, $C_\mu = 0.09$, $\sigma_k = 1.1$ and $\sigma_\varepsilon = 1.3$.

3.5 Numerical Procedure

The numerical procedure is more extensively explained in chapter 2. Here a summary is given for the context of this chapter.

A fully-developed channel flow using half of the channel height, h, is applied given the symmetry of the governing geometry. We assigned 100 cells in the transverse (wall) direction with approximately 10 cells located inside the viscous sublayer. This is to provide mesh independent results, with errors within 0.5% for the mean velocity and the friction factor compared with a very fine mesh, similarly with [40]. The initial state of the simulation is the Newtonian solution until a steady-state solution was reached for each run case, except for HDR where a similar IDR developed case is applied to reduce computational time. Relaxation factors for the additional conformation tensor field are set to 0.2, along with residual control set to 10^{-5}. To improve numerical stability, an artificial diffusion term is added to the RACE of the form, $\kappa \partial_k^2 C_{ij}$, where κ denotes a constant, isotropic, artificial numerical diffusivity. In earlier studies [36], the dimensionless artificial numerical diffusivity is taken to be $\kappa / h u_\tau \sim O(10^{-2})$. Here, $\kappa / h u_\tau \sim O(10^{-3})$ and

has negligible effect on mean values. A pressure gradient is forced in the streamwise direction to be unity, with periodic boundary conditions for all other flow fields, mimicking the DNS procedure of Li et al. [15]. No-slip boundary conditions were imposed on the solid wall for the velocity field U, along with k and $\tilde{\varepsilon}$ set to zero (or very small, $\sim 10^{-15}$). A Dirichlet boundary condition for C_{ij} is reported in Equation (2.17).

3.6 Results and Discussion

Following the numerical procedure proposed in the previous section, the model performance is assessed against a range of different flow and rheological parameters presented in the DNS data within Table 3.1.

3.6.1 Analysis of Conformation Tensor

Figure 3.4 compares the individual components of the conformation tensor with the present model against the model of Resende et al. [70] and selected DNS data covering L^2, Wi_{τ_0} and Re_{τ_0} variations (cases 16, 19, 20 and 26 in Table 3.1). As can be viewed in Figure 3.4a, the C_{xx} predictions are consistent with the DNS data. The new closure for NLT_{xx} (see term III in Equation (3.17)) is responsible for the improved predictions and can capture the Re_{τ_0}, L^2 and Wi_{τ_0} variations with much greater simplicity, especially for increased Reynolds number ($Re_{\tau_0} = 590$) compared with the model of Resende et al. [70].

Figure 3.4b plots the C_{yy} component, showing good agreement with the DNS data and improving upon the most recent model, especially away from the wall. The important feature is the location of the value at the centre-line and the peak location which both show good improvement, especially for higher Reynolds numbers ($Re_{\tau_0} = 590$). The improvements are a result of the new E^V closure (see Equation (3.25)) which directly impacts ε^N in the NLT_{yy} closure (see term I in Equation (3.17)). Figure 3.4c plots the C_{zz} component and shows an under-prediction due to the isotropic assumption used in the model of NLT_{ij}, however, its impact is not significant.

The model predictions of the C_{yy} term are important in capturing the features of the C_{xy} component. As can be observed in Figure 3.4d, the model is able to capture the near-wall region, which, according to the findings of Li et al. [15], is the region of high chain dumbbell extension (limited to $y^+ < 50$) where the effect of C_{xy} acts towards the polymer shear stress.

It is evident that the overall predictions of the individual conformation tensor components are improved compared to the model of Resende et al. [70]. This is a result of the new NLT_{ij} and E^V closures developed in the present work, which allows more scope of predictability and increased numerical stability with simpler closures.

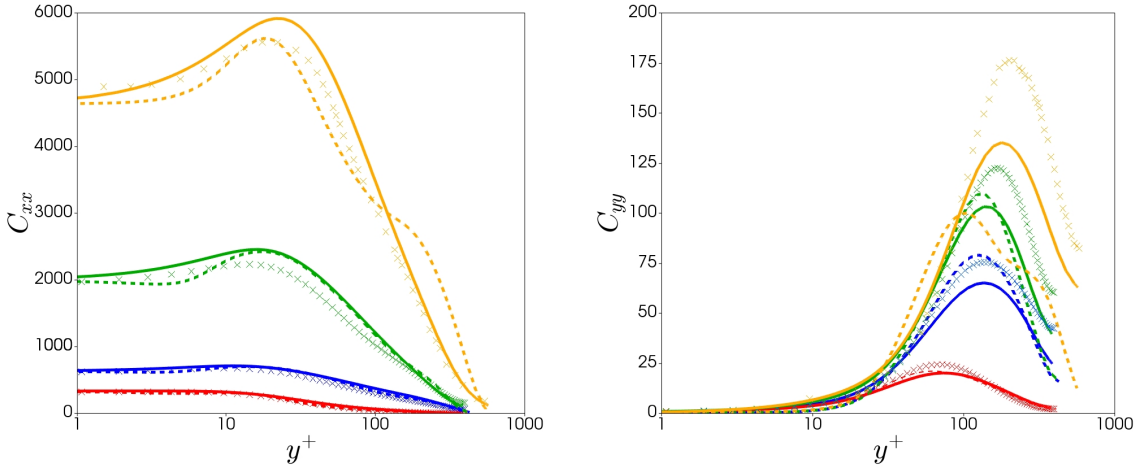

(a) C_{xx} (b) C_{yy}

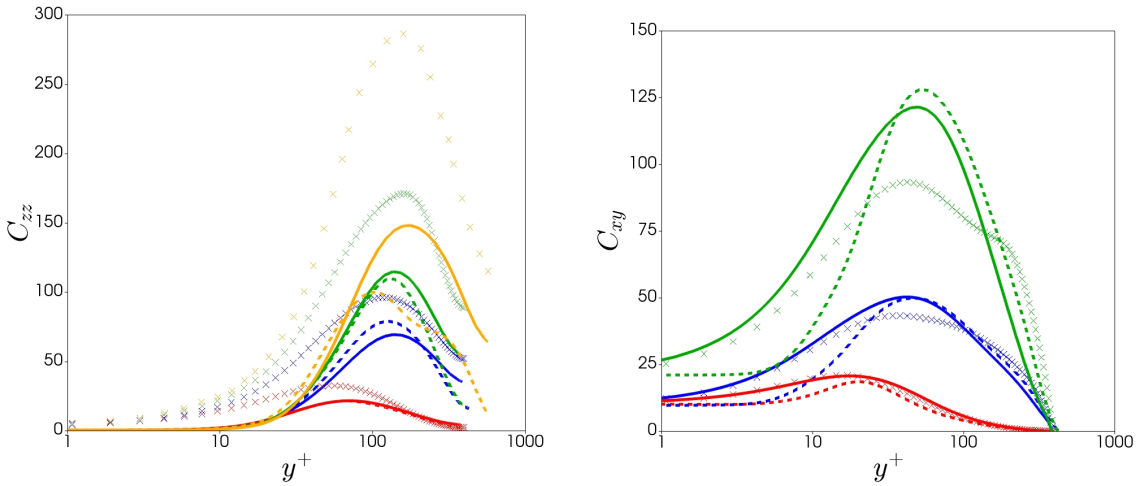

(c) C_{zz} (d) C_{xy}

Figure 3.4: Comparison of the conformation tensor between DNS data ($\times$ crosses) and predictions with the new model (continuous lines), and previous model (dash lines). Each colour represents a different drag reduction regime: red (LDR, case 16); blue (IDR, case 19); green (HDR, case 20) and orange (very HDR, case 26. DNS data not available for C_{xy}).

3.6.2 Analysis of k, ε and ν_T

The predicted k profiles are shown in Figure 3.5a for cases 16 and 19 in Table 3.1, and Figure 3.5b for low and high Reynolds number cases (7 and 27). There is reasonable improvement of the profile away from the wall as a result of the new f_v closure for increasing drag reduction and for various Reynolds numbers.

In Figure 3.6, the prediction of the dissipation rate are compared with the DNS data of both LDR (case 16) and very HDR (case 22), along with predictions for the $v^2 - f$ model of Masoudian et al. [16]. The predictions for LDR are captured well with the DNS for both near and far from the wall. For HDR, there is a significant improvement near the wall compared with the $v^2 - f$ model. This is a result of the E^V closure formulated

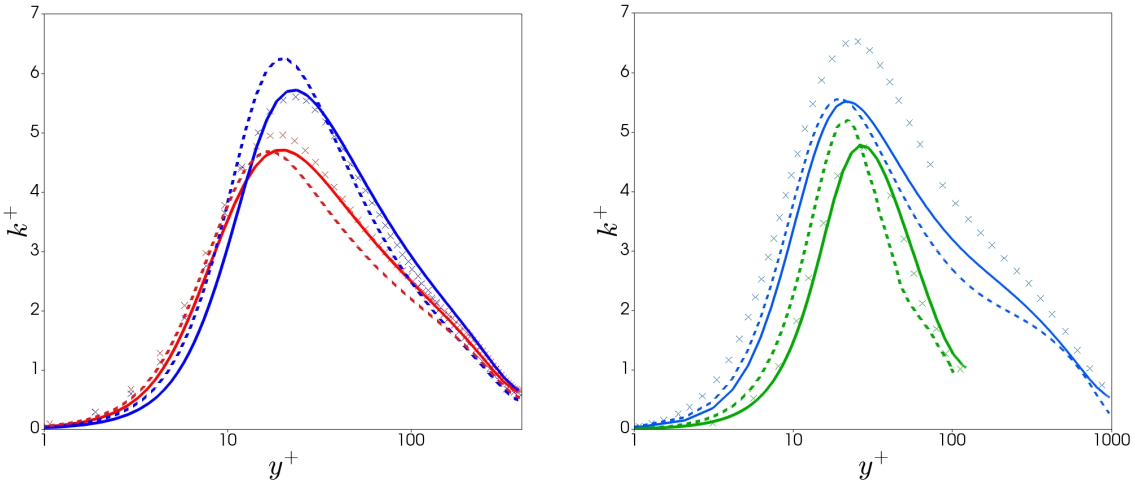

(a) $Re_{\tau_0} = 395$ (b) $Re_{\tau_0} = 125, 1000$

Figure 3.5: Comparison of turbulent kinetic energy between DNS data ($\times$ crosses) and predictions with the new model (continuous lines), and previous model (dash lines): (**a**) $Re_{\tau_0} = 395$—red (LDR case 16)—and blue (IDR case 19); (**b**) $Re_{\tau_0} = 125$—green (HDR, case 7) and $Re_{\tau_0} = 1000$—blue (IDR, case 27).

(see Equation (3.25)) which decreases ε as flow viscoelasticity increases. The model of Resende et al. [70] shows similar results to the current model and is not plotted so that the figure is clearer. However, the complexity of the present E^V closure model is reduced substantially and removes all friction velocity dependence, but can still predict all the main flow features with good performance.

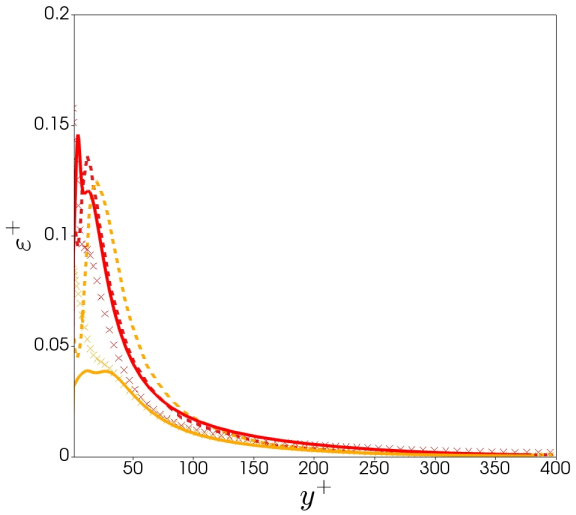

Figure 3.6: Comparison of the rate of Newtonian dissipation of k between DNS data ($\times$ crosses) and predictions with the new model (continuous lines), and $v^2 - f$ model of Masoudian et al. [16] (dash lines). Each colour represents a different drag reduction regime: red (LDR case 16); orange (HDR case 22).

The local eddy viscosity is plotted in Figure 3.7a for all ranges of DR. The combined performance of f_v, k and ε gives rise to the predictions shown. We observe a reduction in the eddy structures within the buffer-layer and log-layer for increasing DR, as the DNS suggests. The damping function predicts well this behavior with the near-wall polymer extension via C_{kk} and the global reduction via $(1-A)$.

3.6.3 Analysis of Stresses and Velocity Profiles

The overall stress balance (Reynolds stress, solvent stress and polymer stress) is plotted in Figure 3.8 for LDR, IDR and HDR. The Theory line is the sum of the stress components and is defined by $1 - \frac{y^+}{Re_{\tau_0}}$. Each component is predicted well, with some over-prediction of the polymer stress term for HDR.

Figure 3.7b shows the mean streamwise velocity profiles for all ranges of DR at $Re_{\tau_0} = 395$. All of the profiles reduce to the linear distribution $u^+ = y^+$ in the viscous sub-layer. Further from the wall, the velocity profiles are well-captured for all ranges of DR.

The model can also predict well a range of Reynolds numbers with varying rheological parameters as can be viewed in Figure 3.9a. This is extended in Figure 3.9b for high Reynolds numbers, where there is a significant improvement compared with the model of Resende et al. [70]. This is a result of the new closure model for NLT_{xx} which scales well with Reynolds number and with reduced complexity.

The advantage of the current model is the ability to capture all velocity profiles well within the model limits, with more simplicity with regards to model closures and without friction velocity dependence.

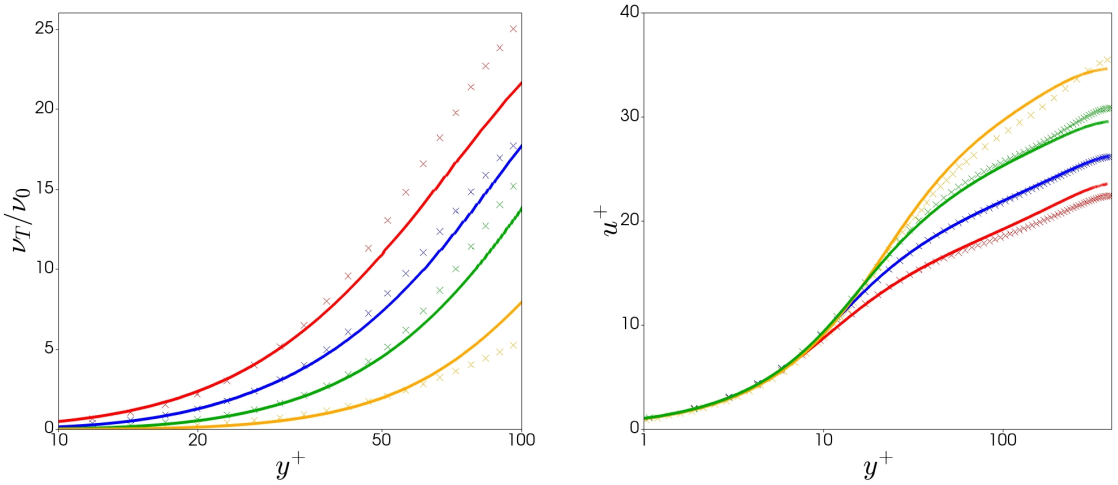

(a) (b)

Figure 3.7: Comparison of the (**a**) local eddy viscosity and (**b**) mean streamwise velocity profile, between DNS data ($\times$ crosses) and model predictions (continuous lines). Each colour represents a different drag reduction regime: red (LDR case 16); blue (IDR case 19); green (HDR case 20); orange (very HDR case 22).

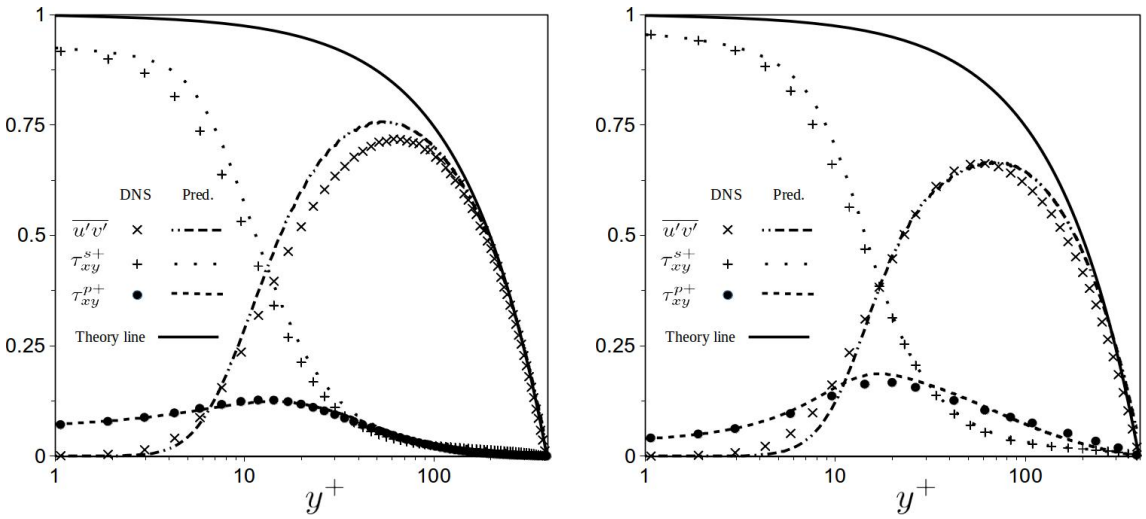

(a) LDR

(b) IDR

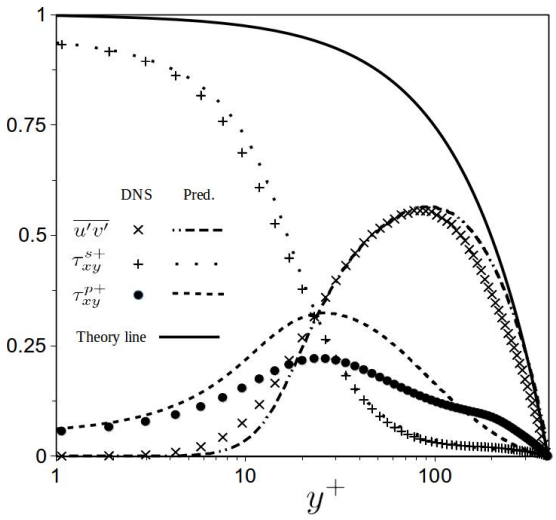

(c) HDR

Figure 3.8: Comparison of the stresses at (a) LDR, (b) IDR and (c) HDR, between DNS data (symbols) and model predictions (lines).

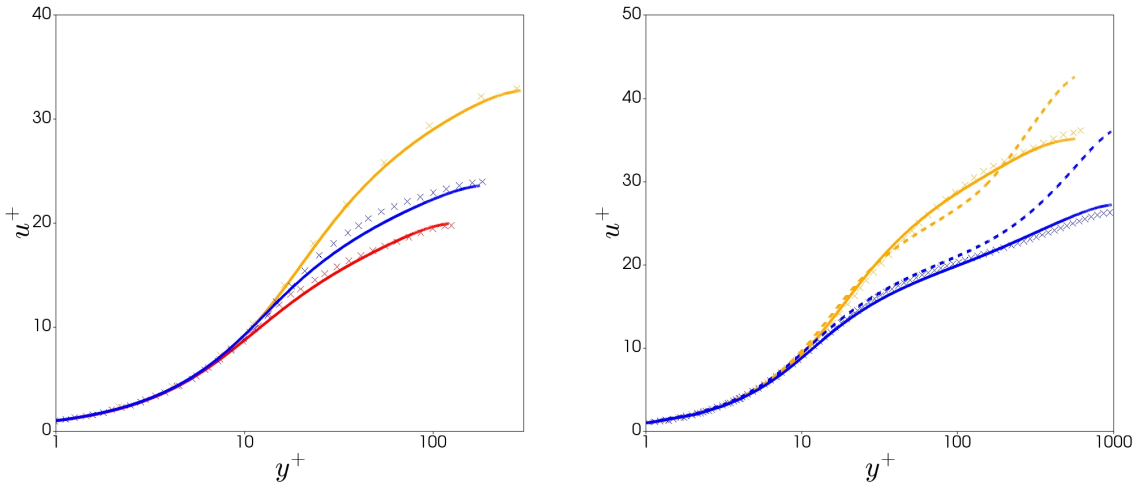

(a) $Re_{\tau_0} = 125, 180, 300$ (b) $Re_{\tau_0} = 590, 1000$

Figure 3.9: Comparison of the velocity profiles between DNS data ($\times$ crosses), current model predictions (continuous lines) and previous model predictions [70] (dashed lines). Each colour represents a different drag reduction regime: (**a**) red (LDR case 1); blue (IDR case 10); orange (very HDR case 15). (**b**) blue (IDR case 27); orange (very HDR case 26).

3.7 Conclusions

A viscoelastic turbulence model in fully-developed drag-reducing channel flow is improved, with turbulent eddies modelled under a $k-\varepsilon$ representation, along with polymeric solutions described by the finitely extensible nonlinear elastic-Peterlin (FENE-P) constitutive model. A new finite volume C++ computational solver was developed in the OpenFOAM software by modifying the $k-\varepsilon$ sub-class files and introducing the FENE-P viscoelastic quantities such as: the polymer stress to the momentum equation; conformation tensor transport equation; and modified damping function to include elastic effects. The model performance is evaluated against a variety of rheological parameters within the DNS data literature, including: friction Reynolds number $Re_{\tau_0} =$ 125, 180, 300, 395, 590, 1000; Weissenberg number $Wi_{\tau_0} = 25$, 36, 50, 100, 116, 200; and maximum molecular extensibility of the dumbbell chain $L^2 = 900$, 1800, 3600, 10000, 14400. The DNS data case (19) in Table 3.1 ($Re_{\tau_0} = 395$, DR = 37%) is used for the calibration of the closures developed for the turbulent cross-correlations identified in Section 3.3. The model is capable of predicting all flow features for low and high Reynolds numbers at all regimes of DR and improves significantly on the model of Resende et al. [70], with its ability to capture higher Reynolds numbers with simpler closures.

The main feature is the formulation of the NLT_{ij} term which accounts for the interactions between the fluctuating components of the conformation tensor and the velocity gradient tensor. The advantage of the closure is the reduction in the complexity and use of damping functions in the dominant contribution, NLT_{xx}, modelled here to increase with turbulent kinetic energy as the flow viscoelasticity increases, demonstrating significant improvement with a range of rheological parameters and flow conditions.

Further improvements are developed for the viscoelastic contribution to the dissipation equation, E^V. This is modelled here with dependence on k and viscoelastic quantities, showing the ability to predict ε for low and high drag reduction.

An improved modified damping function, f_v, is also presented, which is able to predict the global reduction of the eddy viscosity and shift away from the wall for increasing viscoelasticity, whilst also improving the profiles of turbulent kinetic energy.

Overall, predictions compare very well with a wide range of DNS data and significantly improves on capturing all flow features with simplicity and performance compared with the most recent $k-\varepsilon$ model developed by Resende et al. [70]. The simplicity of the present model allows easy implementation into 3D codes and increases numerical stability. All friction velocity dependence is removed in the present model which is the first of its kind for damping function $k-\varepsilon$ models. Future work to extend to this study includes the development of an improved $k-\omega$ model based on the present model [41]. This would require the same concept of the modified damping function developed in this paper to be applied, with capabilities to predict flow behaviour in industrially represented geometries such as pipes and constrictions.

Chapter 4

An improved $k-\omega$ turbulence model for FENE-P fluids with β variation

4.1 Introduction

In the present chapter, a $k-\omega$ model is developed based on the recent $k-\varepsilon$ model of McDermott et al. [99] (Chapter 3) and Resende et al. [70]. The model here introduces β variation, along with a new formulation of the damping function from the Newtonian model [107]. The model vastly improves on the previous $k-\omega$ model of Resende et al. [41, 70]. The shortcomings in the model complexity of the NLT_{ij} term and other viscoelastic turbulent closures are addressed by applying a more physically based approach, and removing all additional damping functions and friction velocity dependence. A similar closure for the modified damping function as seen in Chapter 3 is also proposed, capable of predicting the decrease of the eddy viscosity for all ranges of DR. The advantage of the current model is the ability to predict DR behaviour for a large range of flow and rheological parameters, with model simplicity and without the need for friction velocity dependence.

The chapter is organised as follows: Section 4.2 introduces the instantaneous and time-averaged governing equations and identifies some of viscoelastic terms that will require modelling; Section 4.3 introduces the closures to the Newtonian turbulence model and changes to the damping function, along with presenting the other viscoelastic terms that need closures; Section 4.4 explains in detail the development of the viscoelastic turbulent closures based on comparisons with DNS data of fully developed channel flow present within the literature; Section 4.5 summarises the model; Section 4.6 presents the results of the flow fields in fully developed channel flow, covering all ranges of DR and flow conditions; and finally in Section 4.7, the main conclusions are presented. The work presented in this chapter has been published in [108].

4.2 Governing Equations

The incompressible RANS equations for a FENE-P fluid were formulated in section 1, and are here summarised for the context of this chapter.

The Reynolds-averaged continuity and momentum equations are respectively:

$$\frac{\partial U_j}{\partial x_j} = 0, \tag{4.1}$$

$$\rho\frac{\partial U_i}{\partial t} + \rho U_j\frac{\partial U_i}{\partial x_j} = -\frac{\partial P}{\partial x_i} + \frac{\partial}{\partial x_j}\left(\mu_s S_{ij} - \rho\overline{u_i'u_j'} + \overline{\tau}_{ij,\mathrm{p}}\right), \tag{4.2}$$

where

$$\overline{\tau}_{ij,\mathrm{p}} = \frac{\mu_p}{\lambda}\left[f(C_{kk})C_{ij} - f(L)\delta_{ij}\right]. \tag{4.3}$$

and Reynolds averaged conformation evolution (RACE):

$$\frac{DC_{ij}}{Dt} - M_{ij} - NLT_{ij} = \frac{\overline{\tau}_{ij,\mathrm{p}}}{\mu_p}, \tag{4.4}$$

$$M_{ij} = C_{jk}\frac{\partial U_i}{\partial x_k} + C_{ik}\frac{\partial U_j}{\partial x_k}, \tag{4.5}$$

$$NLT_{ij} = \overline{c'_{jk}\frac{\partial u'_i}{\partial x_k}} + \overline{c'_{ik}\frac{\partial u'_j}{\partial x_k}}. \tag{4.6}$$

4.3 Turbulence Model

The Reynolds stress tensor is computed by adopting the Boussinesq turbulent stress strain relationship,

$$-\rho\overline{u_i u_j} = 2\rho\nu_T S_{ij} - \frac{2}{3}\rho k\delta_{ij}, \tag{4.7}$$

where k is the turbulent kinetic energy, S_{ij} is the mean rate of strain tensor and ν_T is the eddy viscosity. ν_T is modelled by the typical isotropic $k-\omega$ turbulence model, which includes a damping function f_μ to account for near-wall effects,

$$\nu_T = f_\mu\frac{k}{\omega}, \tag{4.8}$$

where ω is the specific rate of dissipation of k. The $k-\omega$ Newtonian transport equations are represented by the Bredberg model [107] which is presented further but with an alternative representation of f_μ. In their work, the damping function was derived from semi-empirical data and the final form is given as,

$$f_\mu^{\text{Bredberg}} = 0.09 + \left(0.91 + \frac{1}{R_t^3}\right)\left[1 - \exp\left\{-\left(\frac{R_t}{25}\right)^{2.75}\right\}\right], \tag{4.9}$$

with $R_t = k/(\nu_s\omega^N)$. The alternative formulation is based on the Newtonian model of Nagano et al. [100] [101] which employs a Van-Driest type damping function of the form,

$$f_\mu^{\text{Nagano}} = \left[1 - \exp\left(-\frac{y^+}{26.5}\right)\right]^2, \tag{4.10}$$

where $y^+ = u_{\tau_0}y/\nu_0$ is the dimensionless wall scaling, u_{τ_0} is the friction velocity, y is the distance to the nearest wall, and ν_0 is the sum of solvent and polymer viscosity coefficients ($\nu_0 = \nu_s + \nu_p$).

An adjustment is made to our model to remove the friction velocity dependence by using an alternative representation of y^+, with the near-wall scaling, y^*, motivated by

Wallin et al. [106] such that,

$$y^* = C_{y1} Re_y^{1/2} + C_{y2} Re_y^2, \tag{4.11}$$

where $Re_y \equiv \sqrt{k}y/\nu_0$, with $C_{y1} = 2.2$ and $C_{y2} = 0.003$. The model constants are slightly adjusted from [106] as they apply a damping function of power 1. The final form of our Newtonian damping function model is given by,

$$f_\mu = \left[1 - \exp\left(-\frac{y^*}{a_\mu}\right)\right]^2, \tag{4.12}$$

with $a_\mu = 26.5$ and y^* given as Equation (4.11). The damping function requires further modelling to include viscoelastic effects of the drag reducing flow, to be discussed later in this chapter.

The governing transport equation for the turbulent kinetic energy for turbulent FENE-P fluids was initially developed by [41], and is given by,

$$\begin{aligned}\rho\frac{\partial k}{\partial t} + \rho U_i \frac{\partial k}{\partial x_i} = &\frac{\partial}{\partial x_i}\left[\left(\mu_s + \frac{\rho\nu_T}{\sigma_k}\right)\frac{\partial k}{\partial x_i}\right] + P_k - \rho C_\mu \omega k \\ &+ Q^V - \rho\varepsilon^V,\end{aligned} \tag{4.13}$$

where $P_k = -\rho\overline{u_i' u_j'}\frac{\partial U_i}{\partial x_j}$ is the rate of production of k, and $\sigma_k = 1.0$. The last two terms on the right side of Equation (4.13) are:

$$Q^V = \frac{\partial \overline{\tau_{ij,p}' u_i'}}{\partial x_j} \quad \text{and} \quad \varepsilon^V = \frac{1}{\rho}\overline{\tau_{ij,p}' \frac{\partial u_i'}{\partial x_j}}, \tag{4.14}$$

which are the viscoelastic turbulent transport and the viscoelastic stress work, respectively. They represent the fluctuating viscoelastic turbulent part of the k transport equation. As presented in section 3.2.3, Q^V is neglected and ε^V requires a suitable closure.

The corresponding transport equation for the specific rate of dissipation, ω, in turbulent channel flow for FENE-P fluids is defined by,

$$\begin{aligned}\rho\frac{\partial \omega}{\partial t} + \rho U_i \frac{\partial \omega}{\partial x_i} = &\frac{\partial}{\partial x_i}\left[\left(\mu_s + \frac{\rho\nu_T}{\sigma_\omega}\right)\frac{\partial \omega}{\partial x_i}\right] + C_{\omega_1}\frac{\omega}{k}P_k - C_{\omega_2}\rho\omega^2 \\ &+ \frac{C_\omega}{k}(\nu_s + \nu_T)\frac{\partial k}{\partial x_i}\frac{\partial \omega}{\partial x_i} + E^V,\end{aligned} \tag{4.15}$$

where $C_\omega = 0.9$, $C_{\omega 1} = 0.49$, $C_{\omega 2} = 0.072$ and $\sigma_\omega = 1.8$. The last term of Equation (4.15) is the viscoelastic contribution to the ω transport and is given by,

$$E^V = 2\nu_s \overline{\frac{\partial u_i'}{\partial x_k} \frac{\partial}{\partial x_k} \left(\frac{\partial \tau_{ij,p}'}{\partial x_j} \right)}, \tag{4.16}$$

It has non-negligible effects on flow predictions for all DR regimes and thus requires a suitable closure model. The full details of these equations can be found in Pinho et al. [38] and Resende et al. [41].

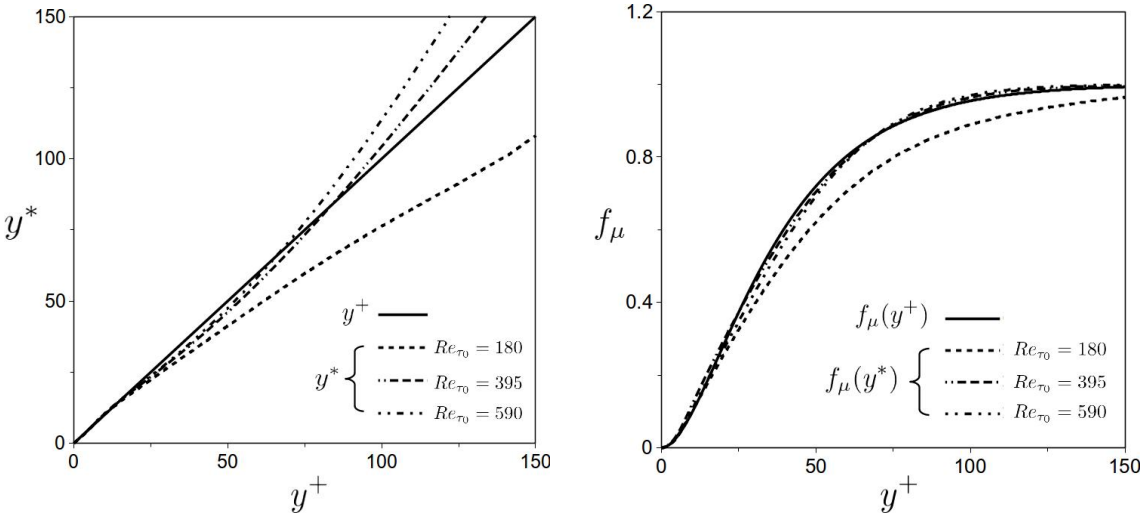

Figure 4.1: (a) Near-wall scaling comparison between y^+ (solid line) and y^* (Equation 4.11) (dashed lines). (b) The damping function (Equation 4.10) compared with Equation 4.12 in Newtonian turbulent channel flow at $Re_{\tau_0} = 180, 395$ and 590.

The performance of the Newtonian model and the effect of the damping function (Equation (4.12)) with y^* (Equation (4.11)) is analysed in Figure 4.1 for fully developed turbulent channel flow at different friction Reynolds number regimes, $Re_{\tau_0} = 180, 395$ and 590. The correspondence between y^* and y^+ is good for $y^+ < 100$, with deviations at the lower Reynolds numbers (Figure 4.1a). The damping function can be viewed in Figure 4.1b where the deviations at $Re_{\tau_0} = 180$ are not sufficient to have a significant impact on model predictions, with higher Reynolds numbers showing excellent agreement. The mean streamwise velocity profile can be viewed in Figure 4.2, predicting low, intermediate and high Reynolds number behaviour very well.

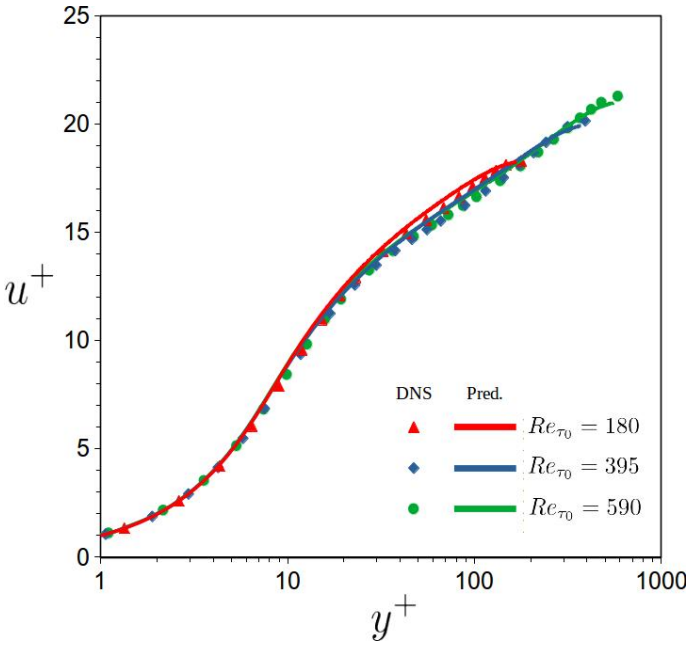

Figure 4.2: Comparison of the velocity profiles for Newtonian turbulent channel flow at $Re_{\tau_0} = 180, 395$ and 590 with DNS data [14] (symbols) and model predictions (solid lines).

4.4 Development of viscoelastic closures

In this section, closure models are developed for the turbulent viscoelastic cross-correlations, namely: NLT_{ij} (Equation (4.6)); ε^V (Equation (4.14)); E^V (Equation (4.16)) and a modified damping function, f_μ (Equation (4.12)). The closure model predictions are validated against DNS data of fully developed channel flow at an intermediate friction Reynolds number of $Re_{\tau_0} = 395$ with a range rheological parameters, then subsequently compared to other DNS data sets for accurate turbulence modelling. The DNS data pertains to a large collection of studies (Table 4.1) in fully developed channel flow performed by Li et al. [61], Thais et al. [102], Masoudian et al. [16, 40, 103], Iaccarino et al. [39] and Ptasinski et al. [57].

Case	Reference	Rheological parameters				Drag reduction (%)		
		$Re_{\tau_0} = \frac{hu_\tau}{\nu_0}$	$\beta = \frac{\nu_s}{\nu_0}$	$Wi_{\tau_0} = \frac{\lambda u_\tau^2}{\nu_0}$	L^2	DNS	Model	Chapter 3
(1)	Li et al. [61]	125	0.9	25	900	19	19	20
(2)	Li et al. [61]	125	0.9	25	3600	22	23	23
(3)	Li et al. [61]	125	0.9	25	14400	24	28	25
(4)	Li et al. [61]	125	0.9	50	900	31	27	30
(5)	Li et al. [61]	125	0.9	50	1800	35	33	32
(6)	Li et al. [61]	125	0.9	100	900	37	34	36
(7)	Li et al. [61]	125	0.9	100	1800	45	38	43
(8)	Li et al. [61]	125	0.9	100	3600	56	49	51
(9)	Masoudian et al. [16]	180	0.9	25	900	19	20	19
(10)	Li et al. [61]	180	0.9	50	900	31	28	30
(11)	Masoudian et al. [16]	180	0.9	100	900	38	34	38
(12)	Masoudian et al. [16]	180	0.9	100	3600	54	47	53
(13)	Thais et al. [102]	180	0.9	116	10000	64	58	60
(14)	Iaccarino et al. [39]	300	0.9	36	3600	33	33	32
(15)	Iaccarino et al. [39]	300	0.9	120	10,000	59	59	59
(16)	Masoudian et al. [40]	395	0.9	25	900	19	23	22
(17)	Masoudian et al. [40]	395	0.9	50	900	30	30	30
(18)	Masoudian et al. [40]	395	0.9	50	3600	38	39	38
(19)	Masoudian et al. [40]	395	0.9	100	900	37	35	37
(20)	Masoudian et al. [40]	395	0.9	100	3600	48	48	47
(21)	Masoudian et al. [103]	395	0.9	100	10000	55	58	55
(22)	Masoudian et al. [40]	395	0.9	100	14,400	61	63	60
(23)	Thais et al. [102]	395	0.9	116	10,000	62	60	60
(24)	Li et al. [61]	395	0.9	200	14,400	75	70	69
(25)	Masoudian et al. [40]	590	0.9	50	3600	39	39	40
(26)	Thais et al. [102]	590	0.9	116	10,000	61	61	59
(27)	Thais et al. [102]	1000	0.9	50	900	30	35	33
(A)	Ptasinski et al. [57]	180	0.8	54	1000	40	40	-
(B)	Ptasinski et al. [57]	180	0.6	54	1000	61	63	-
(C)	Ptasinski et al. [57]	180	0.6	72	1000	66	65	-

Table 4.1: Independent DNS data of fully-developed turbulent channel flow for FENE-P fluids with DR model predictions.

4.4.1 Closures for the conformation tensor

To compute the polymer stress, we need to calculate the components of the conformation tensor, C_{ij}, which are computed with the RACE (Equation (4.4)). The set of analytical equations for fully developed channel flow can be viewed in Appendix 1 of [38]. The polymer shear stress component can be written as

$$\overline{\tau}_{xy,\mathrm{p}} = \frac{\nu_p}{\lambda} f(C_{kk}) C_{xy} = \nu_p \underbrace{\left(\frac{\lambda NLT_{yy} + 1}{f(C_{mm})} \right)}_{C_{yy}} \frac{\mathrm{d}U}{\mathrm{d}y} + \nu_p NLT_{xy}. \tag{4.17}$$

In order to obtain predictions for the polymer shear stress in fully developed channel flow, one requires a closure model for C_{xy} and C_{kk}. The NLT_{yy} and NLT_{xy} terms act towards an effective polymer viscosity [39, 104]. The stretching of the polymer chains is accounted for by NLT_{kk}, and predominantly occur in the direction of mean flow or direction of the largest normal Reynolds stress, xx.

Here, a closure is developed for all relevant components based on the $k-\varepsilon$ model of Resende et al. [70]. The NLT_{ij} closure is presented below in three key parts, with a detailed explanation of each term:

$$\begin{aligned} NLT_{ij} \approx & \underbrace{f_N C_{N1} C_\mu \frac{\lambda \sqrt{L} k \omega}{\nu_0 f(C_{mm})} \delta_{ij}}_{I} - \underbrace{f_N^{1/4} C_{N2} M_{ij}}_{II} \\ & + \underbrace{C_{N3} \frac{k}{\nu_0} \sqrt{\frac{L(1-\beta) M_{nn}}{\gamma} \frac{\frac{\partial U_i}{\partial x_k} \frac{\partial U_j}{\partial x_k}}{\gamma^2}}}_{III}, \end{aligned} \tag{4.18}$$

where $f_N = \nu_T / \nu_0$ is the local eddy viscosity, $\gamma = \sqrt{2 S_{ij} S_{ij}}$ is the shear rate invariant, with model constants $C_{N1} = 0.02$, $C_{N2} = 0.3$ and $C_{N3} = 0.18$.

- Term I captures the NLT_{yy} component and is similar to the model found in Resende et al. [70]. The adjustments were made in the context of the $k-\omega$ model, with minor corrections to the parameter values.

- Term II is primarily responsible for capturing the shear component, NLT_{xy}, which is a key component in predicting C_{xy}. The correlation here is with the exact term, M_{ij} (see Equation (4.5)), and by the local eddy viscosity, $f_N^{1/4}$. The $L^{0.15}$ variation is removed from the model developed by Resende et al. [70]. The negative part of the NLT_{xx} component is also captured here via the M_{xx} term, with this component acting as a destruction term near walls.

- Term III is developed to predict the NLT_{xx} component which is the dominant term in the trace of NLT_{ij}, responsible for the stretch of the polymer chains due to turbulent fluctuations. Following the same assumption as Masoudian et al. [69], one can see that $NLT_{xx} \sim \overline{u_x' u_x'} \sim k$. In physical terms, the turbulent stretching terms represent the ability

of the turbulent fluctuations to act on the polymer chains. This stretching is effective if the polymer shear, maximum extensibility and/or beta variation is large enough. So $\sqrt{L(1-\beta)M_{kk}/\gamma}$ is included here with k. Note that for fully developed channel flow, this term reduces to $\sqrt{L(1-\beta)C_{xy}}$ which increases proportional to drag reduction. The β variation is added from chapter 3, with further adjustments made to f_μ further in the thesis. This new term includes the same physical assumption as Masoudian et al [16, 40], and is simplified from the *ad hoc* approach of Resende et al. [70] which contained bulk parameters.

The performance of the individual components of NLT_{ij} can be analysed in Figure 4.3 by comparing current model predictions against DNS data for low, intermediate and high DR in fully-developed turbulent channel flow at $Re_{\tau_0} = 395$. The previous $k-\omega$ model closure of NLT_{ij} from Resende et al. [41] can also be viewed comparatively here. Figure 4.3a shows NLT_{xx}, the dominant polymer stretching term. It is clear that the model predictions match well with DNS data and improve significantly on the previous $k-\omega$ model of Resende et al. [41], requiring a much simpler closure without additional damping functions. Figure 4.3b & 4.3d show the NLT_{yy} and NLT_{xy} terms respectively, needed for the polymer shear stress. The flow features are well captured such as the peak location and shift away from the wall for increasing viscoelasticity. Figure 4.3c shows the NLT_{zz} component and generally under-predicts. Pinho et al. [38] showed that NLT_{zz} has low impact on flow features and thus the current model predictions are adequate for the purposes of this study. All flow features are well captured such as the magnitude and peak locations, improving significantly on the previous model. The effect of the NLT_{ij} closures on the mean conformation tensor are analysed in the results section.

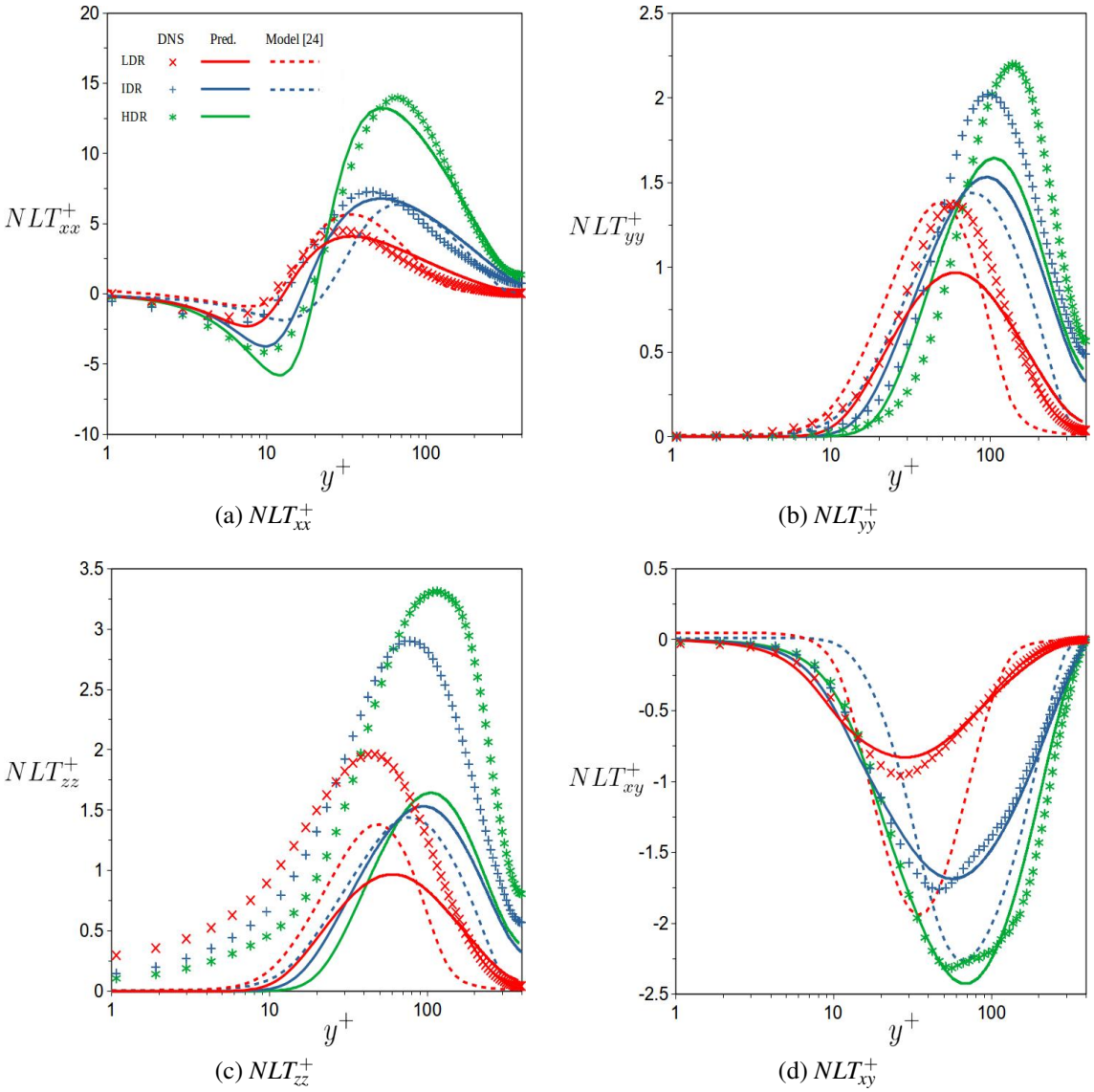

(a) NLT^+_{xx} (b) NLT^+_{yy}

(c) NLT^+_{zz} (d) NLT^+_{xy}

Figure 4.3: Comparison of the NLT_{ij} components between DNS data (symbols) and model predictions (lines) for channel flow at $Re_{\tau_0} = 395$: (a) NLT_{xx} (legend used for all figures); (b) NLT_{yy}; (c) NLT_{zz}; (d) NLT_{xy}. Each colour represents a different drag reduction regime: case 16 (LDR); case 19 (IDR); case 20 (HDR).

4.4.2 Model for the modified damping function, f_μ

In viscoelastic turbulent flow, there is a reduction in the Reynolds shear stress and shift away from the wall of the peak as observed in the DNS [61]. There is a thickening of the buffer layer causing a turbulent kinetic energy redistribution, increasing in magnitude with viscoelasticity. The cause of this is in part due to a reduction in the pressure-velocity correlation found in the full Reynolds Stress Model [60]. In the context of RANS modelling, Iaccarino [39] attempted to model this effect implicitly by proposing an effective rate of production within the f equation of the $v^2 - f$ model, where f represents the turbulent redistribution process. Direct modelling of this term is complex and can lead to numerical stiffness and complete relaminarisation in previous models [39, 67]. An alternative is to model this effect implicitly with a modified damping function, which can capture the dynamics of the eddy viscosity in viscoelastic flows. Here the constant a_μ in Equation (4.12) is enhanced to incorporate an effective thickening of the buffer layer, as similarly presented in [70]. This term is made proportional to the polymer stretching term, C_{kk}/L, which is shown to be proportional to DR in the DNS studies [61]. The term $(1-A)$ ensures smooth variations in the buffer and logarithmic layer, causing a global reduction in the eddy viscosity as shown in the DNS studies [61].

The complete modified damping function is presented as,

$$f_\mu = (1-A)\left[1-\exp\left(-\frac{y^*}{a_\mu\left(1+B/a_\mu\right)}\right)\right]^2, \tag{4.19}$$

$$A = C_A\left(f_N\frac{\lambda^2}{f(C_{kk})^2}\left(\frac{L}{30}\right)^{3/2}\frac{\varepsilon}{\nu_0}\right)^{0.3}, \tag{4.20}$$

$$B = C_B(1-\beta)^{0.2}\frac{(C_{kk}-3)^{1.25}}{L}, \tag{4.21}$$

with y^* given by Equation (4.11) and model constants $C_A = 0.071$ and $C_B = 0.69$.

Model constants vary from Chapter 3 (Equation 3.19) along with β variation within B. The performance of f_μ is tested against DNS data (case (16), IDR) in fully developed channel flow by analysing the effects on the local eddy viscosity (Figure 4.4a). As viscoelasticity is increased, the decrease of the eddy viscosity is captured well. The thickening of the buffer layer is a result of the high near-wall polymer extension, along with an overall global reduction in the eddy viscosity compared with the Newtonian case, both of which are accurately predicted within the closure model. The effect on the mean production is also shown in Figure 4.4b, capturing the peak location and magnitude well. A sensitivity study was performed by varying the f_μ parameters C_A and C_B by $\pm 10\%$ and $\pm 20\%$ (Table 4.2) with drag reduction as the output. The effect on the mean velocity can be viewed in Figure 4.5. The overall change in drag reduction predictions with varying parameters does not substantially change the results, thus confirming the robustness of the

closure presented.

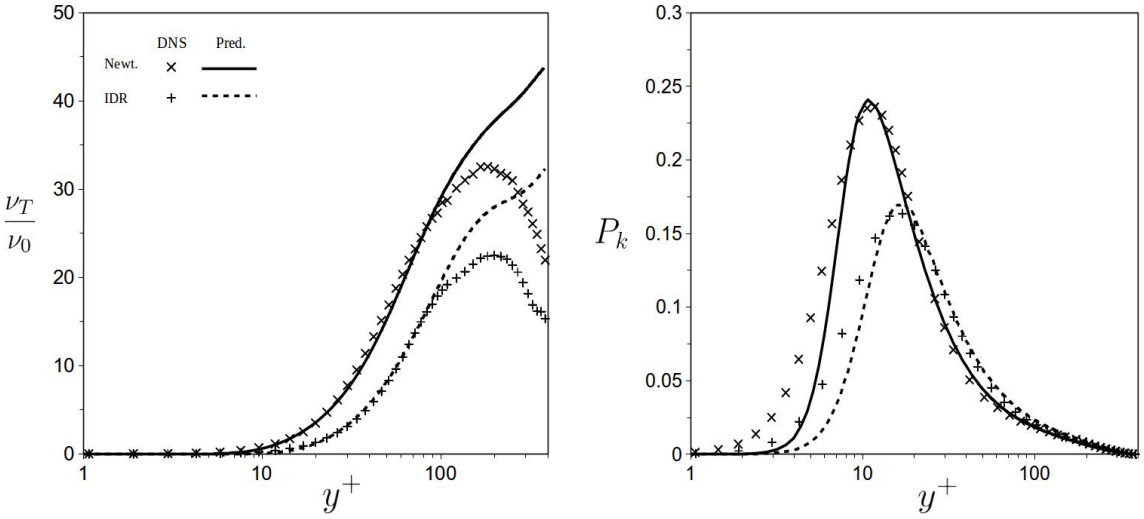

(a) (b)

Figure 4.4: Comparison of the (a) local eddy viscosity and (b) mean production of turbulent kinetic energy between DNS data (symbols) and model predictions (lines) for channel flow at $Re_{\tau_0} = 395$. Newtonian [14] and case 19 (IDR).

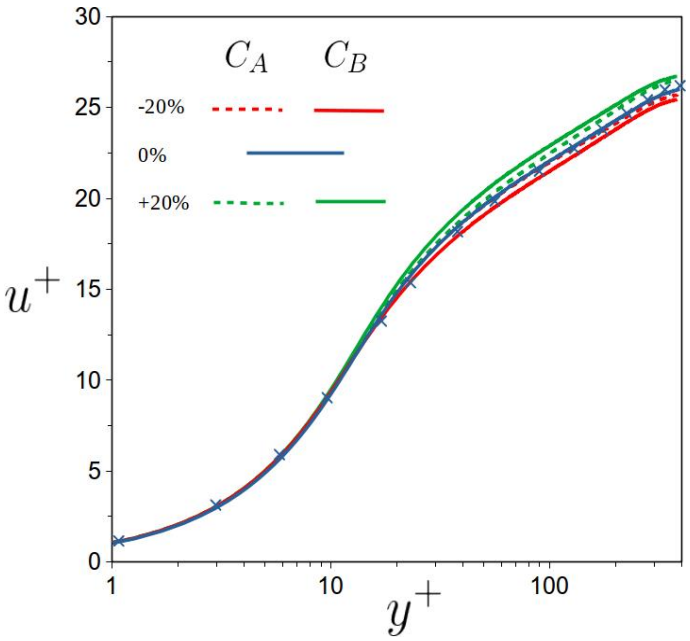

Figure 4.5: Effect of varying parameters C_A and C_B on the mean velocity profile for IDR (case 19). DNS given by blue cross ($\times$).

C_A	$\mathbf{DR}_A$ **(%)**	C_B	$\mathbf{DR}_B$ **(%)**
$0.057(-20\%)$	$33.55(-4.8\%)$	$0.62(-20\%)$	$32.31(-8.3\%)$
$0.064(-10\%)$	$34.31(-2.7\%)$	$0.62(-10\%)$	$33.82(-4.1\%)$
$0.071(0\%)$	$35.26(0\%)$	$0.69(0\%)$	$35.26(0\%)$
$0.078(10\%)$	$36.06(2.2\%)$	$0.76(10\%)$	$36.55(3.6\%)$
$0.085(20\%)$	$36.99(4.9\%)$	$0.83(20\%)$	$37.82(7.2\%)$

Table 4.2: Sensitivity study of drag reduction value with variations in f_μ parameters C_A and C_B by $\pm 10\%$ and $\pm 20\%$.

4.4.3 Development of closures within the k and ε transport equations

The viscoelastic closure models required in the k and ε transport equations are ε^V and E^V, respectively. From section 3.3.3, the viscoelastic stress work, ε^V, is expressed as

$$\varepsilon^V \approx \frac{\nu_p}{2\lambda} f(C_{mm}) NLT_{kk}. \tag{4.22}$$

The closure model derived for E^V assumes that it depends on the same quantities as the classical Newtonian destruction term of the transport equation of ω, but involving a viscoelastic quantity, typically with the viscoelastic stress work used by Resende et al. [41, 68, 70] and Masoudian et al. [16, 40]. However, the models of Masoudian et al. [16, 40] show an opposite trend in ε for increasing DR, which could be explained by the negative contribution of ε^V in the buffer layer.

The closure derived by Resende et al. [41] in the previous $k-\omega$ is very complex with Wi_{τ_0} dependence to force the correct trend in ε. Here, a much simpler approach is obtained with dependence through k which increases with DR, along with the polymer length and concentration via L and $1-\beta = \nu_p/\nu_0$ respectively. The closure is given by

$$E^V \approx -C_{N4}\frac{\omega}{k}\left[\nu_p\sqrt{C_\mu f_\mu}\left(\frac{L}{30}\right)^{0.65}\left(\frac{k}{\nu_0}\right)^2\right], \tag{4.23}$$

with model constant $C_{N4} = 0.026$. The effect of Equation (4.23) on ε predictions can be viewed in the results section for LDR and HDR.

Overall, it is clear that all the developed viscoelastic closures presented in this study perform well compared with DNS data. Most importantly, this was achieved without the need for extra damping functions or the use of friction velocity dependence. The simplicity of the governing closures allows easy implementation into 3D codes and can be extended to flows with reattachment when DNS data becomes available.

4.5 Summary of the new $k-\omega$ model

The governing and transport equations are given below, using the closures developed in the previous section.

Momentum equation:

$$\rho\frac{\mathrm{D}U_i}{\mathrm{D}t} = -\frac{\partial P}{\partial x_i} + \rho\frac{\partial}{\partial x_j}\left[(\nu_s+\nu_T)\frac{\partial U_i}{\partial x_j}\right] + \rho\frac{\partial}{\partial x_j}\left(\frac{\nu_p}{\lambda}\left[f(C_{mm})C_{ij}-\delta_{ij}\right]\right), \tag{4.24}$$

where the eddy viscosity is given by

$$\nu_T = f_\mu\frac{k}{\omega}, \tag{4.25}$$

with modified damping function

$$f_\mu = (1-A)\left[1-\exp\left(-\frac{y^*}{a_\mu\left(1+B/a_\mu\right)}\right)\right]^2, \tag{4.26}$$

$$A = C_A\left(f_N\frac{\lambda^2}{f(C_{kk})^2}\left(\frac{L}{30}\right)^{3/2}\frac{\varepsilon}{\nu_0}\right)^{0.3}, \tag{4.27}$$

$$B = C_B(1-\beta)^{0.2}\frac{(C_{kk}-3)^{1.25}}{L}, \tag{4.28}$$

with constants $a_\mu = 26.5$, $C_A = 0.071$ and $C_B = 0.69$. y^* given by Equation (4.11).

Conformation tensor equation:

$$\frac{DC_{ij}}{Dt} - M_{ij} - NLT_{ij} = -\frac{1}{\lambda}[f(C_{kk})C_{ij}-\delta_{ij}], \tag{4.29}$$

with M_{ij} given by Equation (4.5) and

$$\begin{aligned} NLT_{ij} =& f_N C_{N1} C_\mu \frac{\lambda\sqrt{L}k\omega}{\nu_0 f(C_{mm})}\delta_{ij} - f_N^{1/4} C_{N2} M_{ij} \\ &+ C_{N3}\frac{k}{\nu_0}\sqrt{\frac{L(1-\beta)M_{nn}}{\gamma}}\frac{\frac{\partial U_i}{\partial x_k}\frac{\partial U_j}{\partial x_k}}{\gamma^2}, \end{aligned} \tag{4.30}$$

where $f_N = \nu_T/\nu_0$ is the local eddy viscosity, $\gamma = \sqrt{2S_{ij}S_{ij}}$ is the shear rate invariant, with model constants $C_{N1} = 0.02$, $C_{N2} = 0.3$ and $C_{N3} = 0.18$.

Transport equation of k:

$$\rho\frac{Dk}{Dt} = \rho\frac{\partial}{\partial x_i}\left[\left(\nu_s + \frac{\nu_T}{\sigma_k}\right)\frac{\partial k}{\partial x_i}\right] + P_k - C_\mu\rho\omega k - \frac{\nu_p}{\lambda}f(C_{mm})\frac{NLT_{mm}}{2}. \tag{4.31}$$

Specific rate of dissipation transport equation:

$$\rho\frac{D\omega}{Dt} = \rho\frac{\partial}{\partial x_i}\left[\left(\nu_s + \frac{\nu_T}{\sigma_\omega}\right)\frac{\partial \omega}{\partial x_i}\right] + \frac{C_\omega}{k}(\nu_s+\nu_T)\frac{\partial k}{\partial x_i}\frac{\partial \omega}{\partial x_i} + \frac{\omega}{k}\left(C_{\omega_1}P_k - C_{N4}\nu_p\sqrt{C_\mu f_\mu}\left(\frac{L}{30}\right)^{0.65}\left(\frac{k}{\nu_0}\right)^2\right) - C_{\omega_2}\rho\omega^2 \tag{4.32}$$

and model constant $C_{N4} = 0.026$.

The remaining constant are of the Newtonian model and are $C_\omega = 0.9$, $C_{\omega_1} = 0.49$, $C_{\omega_2} = 0.072$, $C_\mu = 0.09$, $\sigma_k = 1.0$ and $\sigma_\omega = 1.8$.

4.6 Results and discussion

The numerical implementation of the model follows the same fully developed channel flow set-up as described in section 3.5. No-slip boundary conditions are imposed on the solid wall for the velocity field U, along with $k = 0$. The specific rate of dissipation, ω, follows the asymptotic formed by Wilcox [109] such that, $\omega \to \frac{2\nu_s}{C_\mu y^2}$ as $y \to 0$. A Dirichlet boundary condition for C_{ij} is applied as reported in Chapter 3.

The model performance is assessed against a range of different flow and rheological parameters presented in the DNS data within Table 1.

Figure 4.6 plots the components of the conformation tensor (C_{zz} excluded) and shows good agreement with the DNS data for LDR and HDR. The C_{xx} component is dominated by NLT_{xx}, the new term modelled. The peak location near the wall and decay towards the centre is well captured (Figure 4.6a). The shear component C_{xy} (Figure 4.6c) has most effect on the flow in a region $y^+ < 50$ according to the findings of Li et al. [61], which is captured here for LDR and HDR. Finally the C_{yy} component is shown in Figure 4.6b, which is important for an effective polymer viscosity, shown here to capture the shift away from the wall for increasing DR.

Figure 4.7 shows the turbulent kinetic energy profiles for Newtonian and IDR. The increase of k and peak location is captured well, improving greatly upon previous model predictions. Figure 4.8 demonstrates the model capabilities of predicting low and high DR.

The Newtonian dissipation of k is plotted in Figure 4.9 and shows good agreement

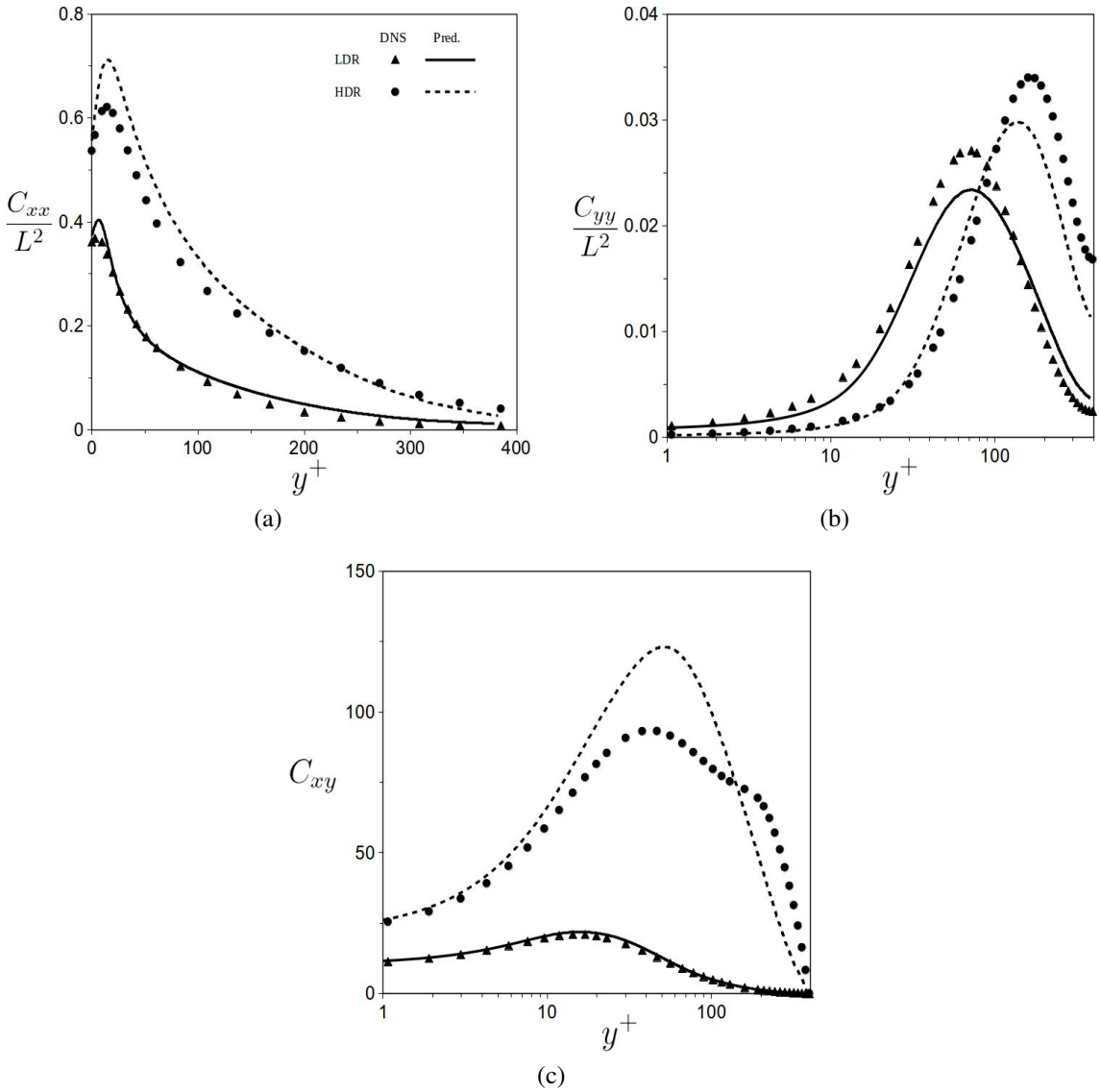

Figure 4.6: Comparison of the conformation tensor components between DNS data (symbols) and model predictions (lines) for channel flow at $Re_{\tau_0} = 395$: (a) C_{xx}/L^2 (legend used for all figures); (b) C_{yy}/L^2; (c) C_{xy}. case 16 (LDR) and case 20 (HDR).

with DNS for LDR and HDR. The near-wall values lose accuracy which is a known defect in isotropic $k-\omega$ models. The closure for E^V predicts well the decrease in ε as viscoelasticity increases.

The local eddy viscosity is plotted in Figure 4.10 for all ranges of DR at $Re_{\tau_0} = 395$. The prefix of L, I, H, VH and M before DR in the plots mean low, intermediate, high, very high and maximum, respectively. The decrease of ν_T with increasing viscoelasticity is predicted well, capturing the thickening of the buffer layer and reduction in the log-layer ascertained by the modified damping function.

The overall stress balance (Reynolds stress, solvent stress and polymer stress) is plotted in Figure 4.11a for IDR, and LDR and HDR in Figure 4.12. The Theory line is the sum of the stress components and is defined by $1 - \frac{y^+}{Re_{\tau_0}}$. Good predictions of the stress balance determines the velocity profile accuracy. The mean streamwise velocity profiles

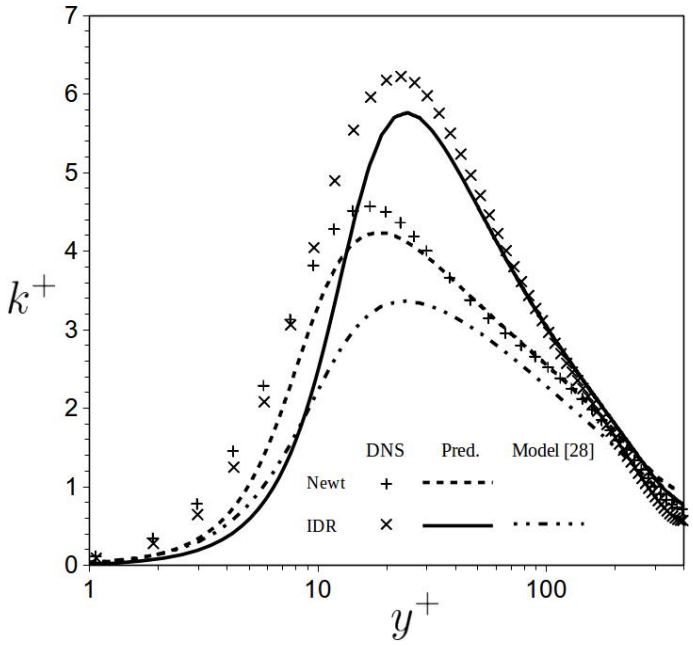

Figure 4.7: Comparison of the turbulent kinetic energy, k, between DNS data (symbols) and model predictions (lines) for channel flow at $Re_{\tau_0} = 395$. Newtonian [14], case 19 (IDR).

for all ranges of DR at $Re_{\tau_0} = 395$ are plotted in Figure 4.11b. The maximum drag reduction asymptote of Virk [110] is also plotted here, along with the viscous sub-layer and log law equations. The model can predict well the increase in the log law for increasing DR. At LDR the model over-predicts, but has an improved performance at different Reynolds numbers. For MDR there is an under-prediction due to the limitations of the isotropic assumptions, where the near-wall eddies become excessively dampened, but still captures fairly well the overall increase of the log law profile. Figure 4.13 shows the model capability in predicting a range of Reynolds numbers and flow parameters. This is extended with small β variation as shown in Figure 4.14 which shows good agreement with the DNS data.

Overall it is evident that the model can predict drag reducing features well for a range of flow and rheological parameters, where the main advantage is through model simplicity and without friction velocity dependence compared to the previous isotopic models [41, 68, 70].

Table 4.1 shows the DR for the $k-\varepsilon$ model (Chapter 3) and current $k-\omega$ model. Both models give similar performance when predicting the range of rheological parameters within the mean DNS data. The main advantage of the $k-\omega$ model is the extension to β variation, which is included through the f_μ and NLT_{kk} model.

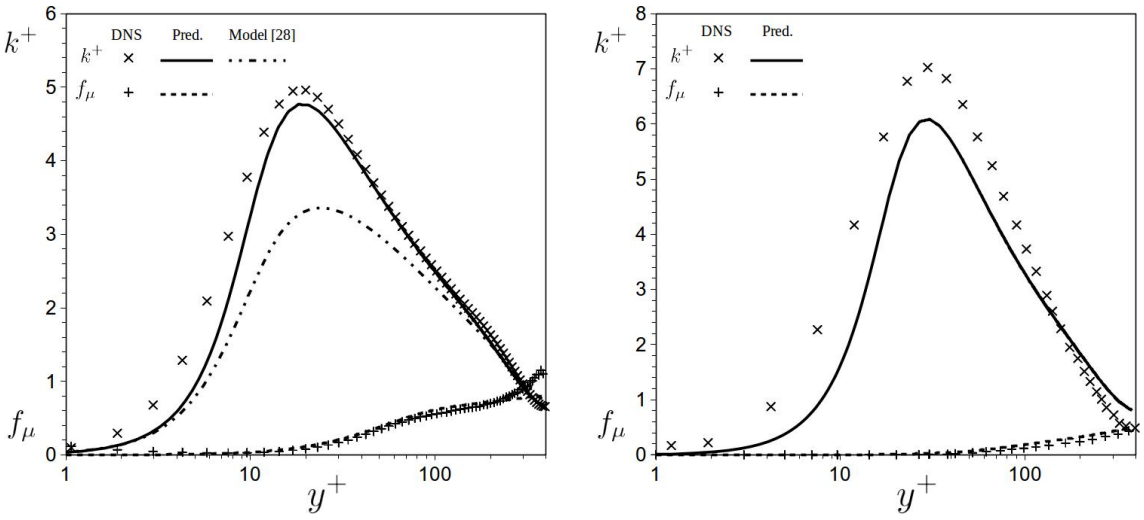

(a) LDR (b) HDR

Figure 4.8: Comparison of the turbulent kinetic energy, k, and damping function, f_μ, between DNS data (symbols) and model predictions (lines) for channel flow at $Re_{\tau_0} = 395$: (a) case 16 (LDR); (b) case 20 (HDR).

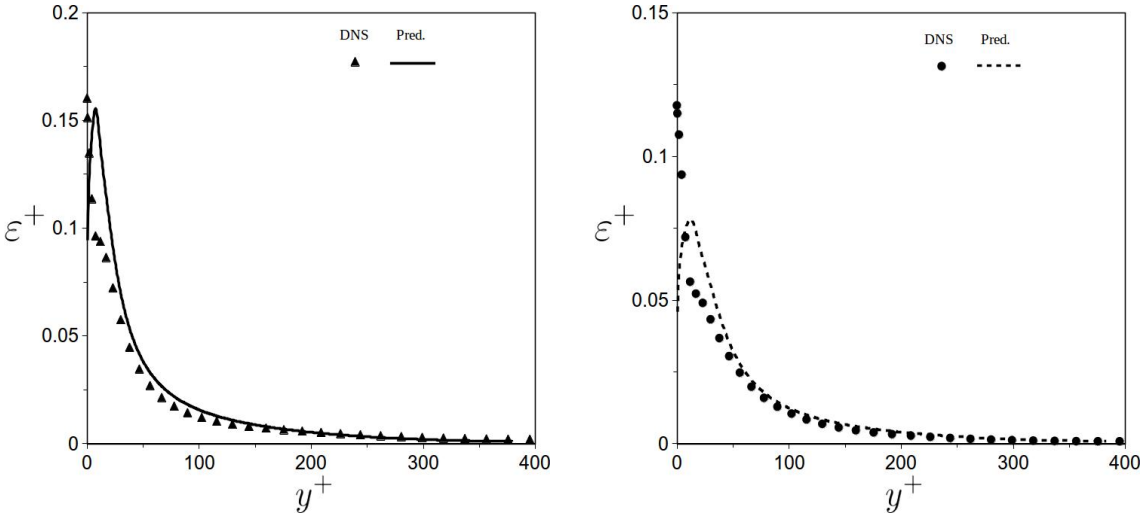

(a) LDR (b) HDR

Figure 4.9: Comparison of the true Newtonian dissipation rate of k between DNS data (symbols) and model predictions (lines) for channel flow at $Re_{\tau_0} = 395$: (a) case 16 (LDR); (b) case 20 (HDR).

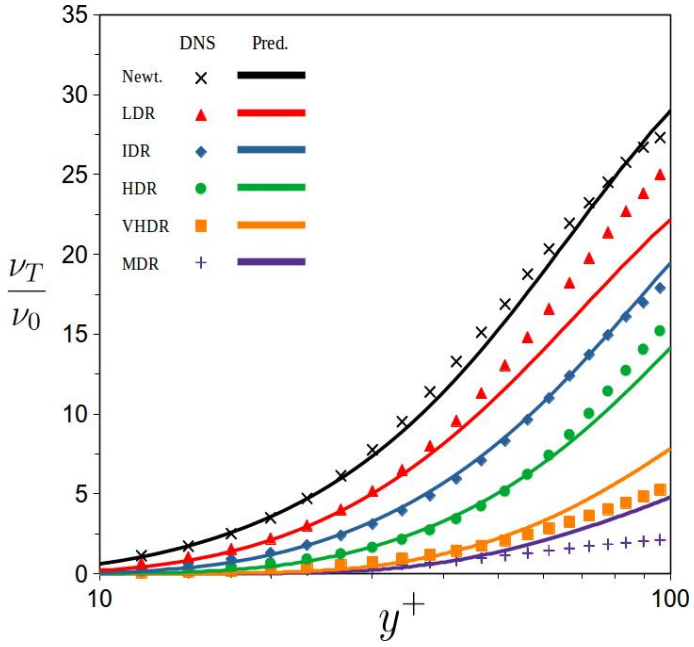

Figure 4.10: Comparison of the local eddy viscosity between DNS data (symbols) and model predictions (lines) for channel flow at $Re_{\tau_0} = 395$. Each colour represents a different drag reduction regime: Newtonian [14]; case 16 (LDR); case 19 (IDR); case 20 (HDR); case 22 (Very HDR); case 24 (MDR).

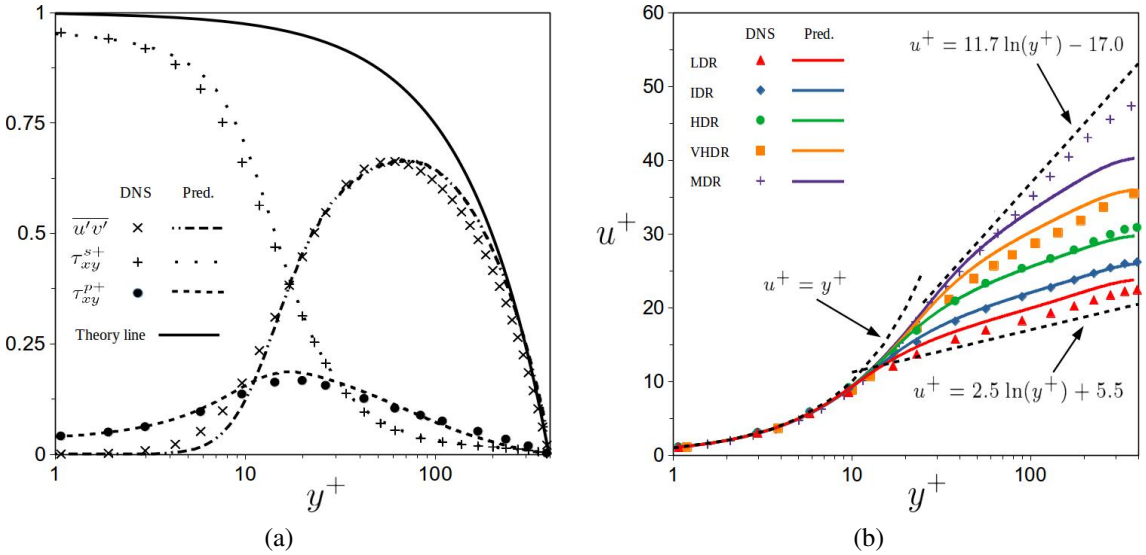

Figure 4.11: Comparison of (a) normalised shear stresses (case 19 (IDR)) and (b) mean streamwise velocity profiles between DNS data (symbols) and model predictions (lines) for channel flow at $Re_{\tau_0} = 395$. Each colour represents a different drag reduction regime: case 13 (LDR); case 19 (IDR); case 20 (HDR); case 22 (Very HDR); case 24 (MDR). The viscous sub-layer equation, log layer equation, and Virk's asymptote [110] are also shown (dotted lines) in (b).

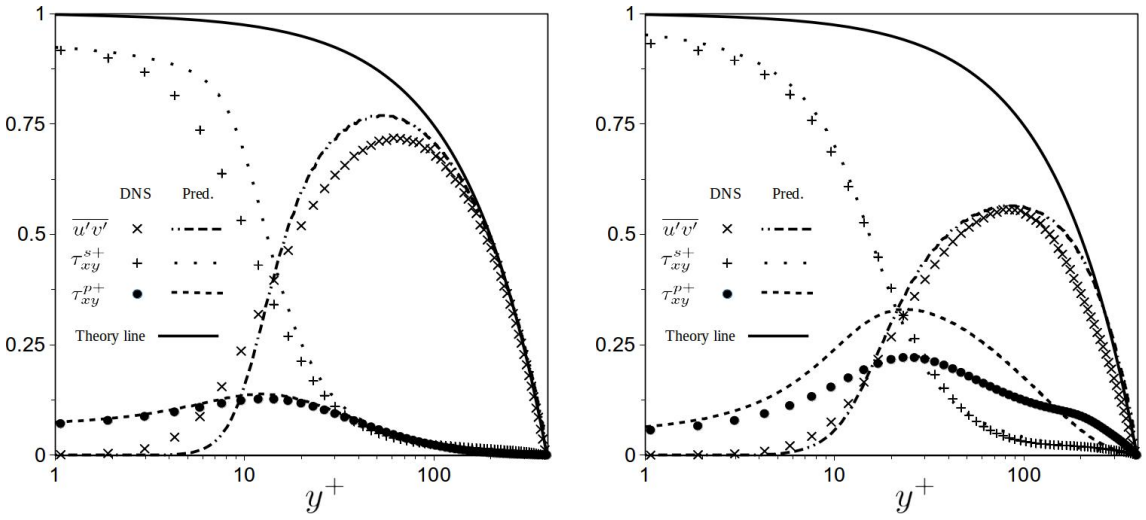

Figure 4.12: Comparison of normalised shear stresses at (a) LDR (case 16) and (b) HDR (case 20), between DNS data (symbols) and model predictions (lines) for channel flow at $Re_{\tau_0} = 395$.

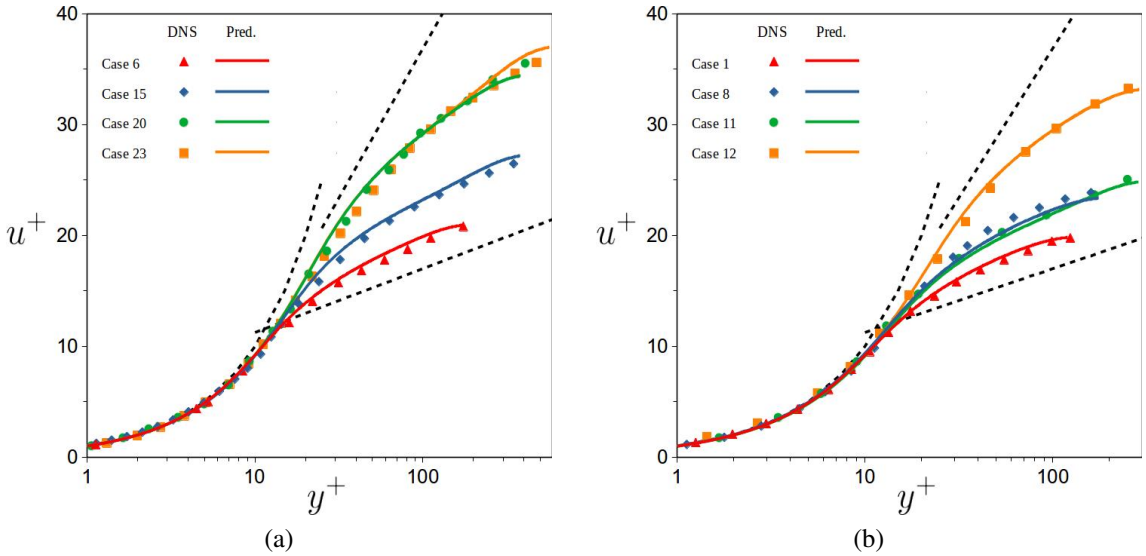

Figure 4.13: Comparison of the mean streamwise velocity profiles between DNS data (symbols) and model predictions (lines) for channel flow at various Reynolds numbers. Each colour represents a different case. See Figure 4.11b for dotted lines.

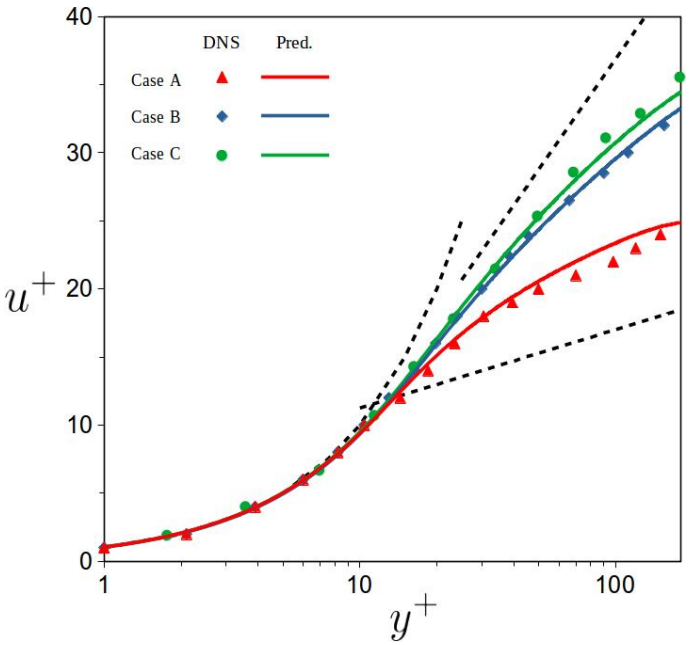

Figure 4.14: Comparison of the mean streamwise velocity profiles between DNS data (symbols) and model predictions (lines) for channel flow at varying β at $Re_{\tau_0} = 180$. Each colour represents a different case. See Figure 4.11b for dotted lines.

4.7 Conclusions

A viscoelastic turbulence model in fully-developed drag reducing channel flow is improved, with turbulent eddies modelled under a $k-\omega$ representation, along with polymeric solutions described by the finitely extensible nonlinear elastic-Peterlin (FENE-P) constitutive model. The Newtonian model of Bredberg [107] is modified to include a new Van-Driest type damping function but including a near-wall scaling, y^*, such that $y^+ \sim y^*$ for $y^+ < 100$. The model performance is evaluated against a variety of rheological parameters within the DNS data literature including: friction Reynolds number $Re_{\tau_0} = 125, 180, 300, 395, 590$; Weissenberg number $Wi_{\tau_0} = 25, 36, 50, 54, 72, 100, 116, 200$; viscosity ratio $\beta = 0.9, 0.8, 0.6$; and maximum molecular extensibility of the dumbbell chain $L^2 = 900, 1000,\ 1800, 3600, 10000, 14400$. The DNS data for $Re_{\tau_0} = 395$ in Table 4.1 is used for the calibration of the closures developed for the turbulent cross correlations identified in section 4.4. The model is capable of predicting a large range of flow features for low and high Reynolds number at all regimes of DR and improves significantly on the model of Resende et al. [41], with its ability to capture higher Reynolds numbers with simpler closures.

The main feature is the modified damping function, f_μ, which is capable of predicting the reduction in the eddy viscosity and effective thickening of the buffer layer as viscoelasticity increases. The correct increase in the turbulent kinetic energy, k, is also shown and improves greatly on the previous model [41]. The model can also capture small β variation in accordance with the FENE-P limits, highlighted with the dependence on $1-\beta$, which is proportional to the polymer concentration. Further improvements are developed within the closures of the NLT_{ij} and E^V terms present within the governing equations after the Reynolds averaging process. The NLT_{ij} model presents a better performance for all regimes of DR when compared with the previous $k-\omega$ model [41]. The main advantage of the closure is the reduction in the complexity and damping functions in the dominant contribution, NLT_{xx}, modelled here to increase with turbulent kinetic energy as the flow viscoelasticity increases. In terms of the viscoelastic contribution to the dissipation equation, E^V, previous isotropic models developed by Resende et al. [41, 68, 70] required friction velocity dependence which is here removed and greatly simplifies the model, keeping the same prediction accuracy of ε.

Overall, the model predicts well across a wide range of DNS data and significantly improves on capturing all flow features with simplicity and performance compared with the most recent $k-\omega$ model developed by Resende et al. [41], which was limited to a few DNS data cases. The current model extends on chapter 3, but here including β variation up-to the FENE-P limits, and with a Newtonian model based on $k-\omega$ that is naturally more numerically stable. The simplicity of the present model allows easy implementation into 3D codes and increases numerical stability. All friction velocity dependence is removed in the present model which is the first of its kind for isotropic

models with damping functions.

Chapter 5

An anisotropic $k-\varepsilon-v^2-f$ model to predict turbulent polymer flow features in fully developed channel and square duct flows

5.1 Introduction

In the present chapter, an anisotropic $k-\varepsilon-v^2-f$ model for Newtonian fluids [91] is adapted to predict polymer flow features in fully developed turbulent viscoelastic channel and square duct flows. A model for NLT_{ij} is formulated based on the redistribution of the stretching term, NLT_{kk}, in a similar fashion to the normal Reynolds stress model in the Newtonian closure. Simple *ad hoc* models are included for the spanwise Reynolds stress component, $\overline{w'^2}$, and the energy redistribution term, f, to include the near-wall reduction from viscoelastic effects, leading to predictions for the secondary flow features. The model is assessed and validated against DNS data for LDR in fully developed channel flow [16], then qualitatively analysed in square duct flow [75] (see Appendix for data used for comparisons).

The chapter is organised as follows: Section 5.2 introduces the Reynolds-averaged governing equations appropriate for wall-bounded turbulent polymer flow, and identifies the viscoelastic terms requiring suitable closure models; Section 5.3 explains in detail the development of viscoelastic turbulent closures, which are validated against DNS data of fully developed channel flow present within the literature; Section 5.4 summarises the present model; Section 5.5 presents the numerical procedure for fully developed channel and square ducts; Section 5.6 presents the results for Newtonian and viscoelastic flow in both channel and square ducts at LDR; and finally in Section 5.7, the main conclusions are presented.

5.2 Governing Equations

The incompressible RANS equations for a FENE-P fluid were formulated in section 1, and are here summarised for the context of this chapter.

The Reynolds-averaged continuity and momentum equations are respectively:

$$\frac{\partial U_j}{\partial x_j} = 0, \tag{5.1}$$

$$\rho\frac{\partial U_i}{\partial t} + \rho U_j\frac{\partial U_i}{\partial x_j} = -\frac{\partial P}{\partial x_i} + \frac{\partial}{\partial x_j}\left(\mu_s S_{ij} - \rho\overline{u_i'u_j'} + \overline{\tau}_{ij,\mathrm{p}}\right), \tag{5.2}$$

where

$$\overline{\tau}_{ij,\mathrm{p}} = \frac{\mu_p}{\lambda}\left[f(C_{kk})C_{ij} - f(L)\delta_{ij}\right]. \tag{5.3}$$

and Reynolds averaged conformation evolution (RACE):

$$\frac{DC_{ij}}{Dt} - M_{ij} - NLT_{ij} = \frac{\overline{\tau}_{ij,\mathrm{p}}}{\mu_p}, \tag{5.4}$$

$$M_{ij} = C_{jk}\frac{\partial U_i}{\partial x_k} + C_{ik}\frac{\partial U_j}{\partial x_k}, \tag{5.5}$$

$$NLT_{ij} = \overline{c'_{jk}\frac{\partial u'_i}{\partial x_k}} + \overline{c'_{ik}\frac{\partial u'_j}{\partial x_k}}. \tag{5.6}$$

5.2.1 Reynolds stresses

The Reynolds stress tensor is computed with the model of Pecnik and Iaccarino [91], which adopts a 'linear'[1] Boussinesq turbulent stress strain relationship,

$$-\overline{u'_i u'_j} \approx 2\nu_T S_{ij} - kN_{ij}, \tag{5.7}$$

where k is the turbulent kinetic energy and ν_T is the eddy viscosity. N_{ij} is formulated to redistribute k in the normal components such that

$$N_{ij} = \frac{2}{3}\delta_{ij} + \left(1 - \frac{3}{2}\frac{v^2}{k}\right)\left(\frac{\delta_{ij}}{3} - n_i n_j\right) + \left(\frac{2 - f_d}{2 + f_d} - \frac{1}{2}\frac{v^2}{k}\right)(2t_i t_j + n_i n_j - \delta_{ij}), \tag{5.8}$$

where the first term is the isotropic component, with the second term ensuring $\overline{v'^2} = v^2$, and the third term redistributing the streamwise and spanwise Reynolds stress components with the function

$$f_d = \min\left[\max\left(\left(\frac{3}{2}\frac{v^2}{k}\right)^{1/2}, 0.3\right), 1.0\right]. \tag{5.9}$$

The direction of anisotropy is obtained by means of a normalised gradient of ϕ,

$$n_i = \frac{\partial \phi}{\partial x_i}/|\nabla \phi|, \tag{5.10}$$

such that ϕ solves an elliptic relaxation equation given as

$$\nabla^2 \phi = -1, \tag{5.11}$$

typically used to obtain smooth variations of the wall distance in complex geometries [111]. At solid walls, $\phi = 0$, and $\partial\phi/\partial x_i = 0$ at open boundaries. The normalised direction of the largest normal Reynolds stress component, t_i, is assumed to coincide with the normalised velocity gradient [91]. This is a reasonable assumption for our studies in pressure driven wall bounded flows. More generally, t_i can coincide with the mean direction of vorticity such that,

$$t_i \sim \frac{\omega_i}{|\omega_i|} = \varepsilon_{ijk}\frac{\partial U_j}{\partial x_k}/\gamma \tag{5.12}$$

[1] The linearity holds because $\overline{u'_m u'_m} = 2k$, however non-isotropic.

where ε_{ijk} is the Levi-Civita symbol, ω_i is the vorticity vector[1] and $\gamma = \sqrt{S_{ij}S_{ij}}$ is the shear rate magnitude.

In this work, the eddy viscosity is modelled by the $k-\varepsilon-v^2-f$ formulation of Lien et al. [92]. This is chosen because of the capabilities of the turbulence model in calculating wall Reynolds stress statistics without damping functions for low Reynolds number models [70, 99]. The eddy viscosity is given as

$$\nu_T = C_\mu \overline{v^2} T_t, \tag{5.13}$$

where C_μ is a constant coefficient, $\overline{v^2}$ is the transverse (wall normal) Reynolds stress scalar, and T_t is the turbulent time scale defined as:

$$T_t = \max\left\{\frac{k}{\varepsilon}, C_T\sqrt{\frac{\nu}{\varepsilon}}\right\}, \tag{5.14}$$

where C_T is a constant coefficient.

The governing transport equation for the turbulent kinetic energy, k, with FENE-P fluids is given by [16],

$$U_j\frac{\partial k}{\partial x_j} = \frac{\partial}{\partial x_j}\left[\left(\nu_s + \frac{\nu_T}{\sigma_k}\right)\frac{\partial k}{\partial x_j}\right] + P_k - \varepsilon + Q^V - \rho\varepsilon^V, \tag{5.15}$$

where $P_k = \overline{u_i'u_j'}S_{ij}$ is the mean rate of production of k.

The last two terms on the right side of the Equation (5.15) are:

$$Q^V = \frac{\partial\overline{\tau_{ij,p}'u_i'}}{\partial x_j} \quad \text{and} \quad \varepsilon^V = \frac{1}{\rho}\overline{\tau_{ij,p}'\frac{\partial u_i'}{\partial x_j}}, \tag{5.16}$$

which are the viscoelastic turbulent transport and the viscoelastic stress work, respectively. They represent the fluctuating viscoelastic turbulent part of the k transport equation and require suitable closure models.

The corresponding governing transport equation for ε, the modified Newtonian rate of dissipation of k, is given by,

$$U_j\frac{\partial \varepsilon}{\partial x_j} = \frac{\partial}{\partial x_j}\left[\left(\nu_s + \frac{\nu_T}{\sigma_\varepsilon}\right)\frac{\partial \varepsilon}{\partial x_j}\right] + \frac{C_{\varepsilon1}P_k - C_{\varepsilon2}\varepsilon}{T_t} - E^V. \tag{5.17}$$

The last term in Equation (5.17) is the viscoelastic contribution to the overall ε balance, given by

$$E^V = 2\nu_s\overline{\frac{\partial u_i'}{\partial x_k}\frac{\partial}{\partial x_k}\left(\frac{\partial \tau_{ij,p}'}{\partial x_j}\right)} \tag{5.18}$$

[1]Not the same as the scalar quantity, ω, in Chapter 4.

It has non-negligible effects on flow predictions for all DR regimes and thus requires a suitable closure model.

The transport equation for the scalar wall Reynolds stress, $\overline{v^2}$, is given by

$$U_j \frac{\partial \overline{v^2}}{\partial x_j} = \frac{\partial}{\partial x_j}\left[\left(\nu_s + \frac{\nu_T}{\sigma_k}\right)\frac{\partial \overline{v^2}}{\partial x_j}\right] + kf - 6\frac{\varepsilon}{k}\overline{v^2} + Q^V_{v^2} - \varepsilon^V_{v^2}. \tag{5.19}$$

The last two terms are the transverse components of Equation (5.16) and require closures.

The turbulence energy redistribution, f, is derived from the pressure-strain correlation term [112, 113] in the full Reynolds stress transport, namely

$$\Pi_{ij} = -\frac{1}{\rho}\left(\overline{u'_i \frac{\partial p'}{\partial x_j}} + \overline{u'_j \frac{\partial p'}{\partial x_i}}\right). \tag{5.20}$$

In the context of Newtonian turbulence $v^2 - f$ models, Equation (5.20) is posed as an integral solution of the Poisson equation of the fluctuating pressure,

$$\nabla^2 p = -2\rho \frac{\partial U_i}{\partial x_j} + \rho(\overline{u'_i u'_j} - u'_i u'_j), \tag{5.21}$$

with a simple isotropic exponential correlation function, $g(x_i, \tilde{x}_i) = \exp(-||x_i - \tilde{x}_i||/L_t)$, where L_t is the correlation length scale. The term, $g(x_i, \tilde{x}_i)$, is the free-space Greens function associated with the operator $-\nabla^2 + 1/L_t^2$, which leads to the *elliptic relaxation equation*

$$\Pi_{ij} - L_t^2 \nabla^2 \Pi_{ij} = \Pi^h_{ij}, \tag{5.22}$$

where Π^h_{ij} is any quasi-homogeneous model. The nomenclature follows that $f = \Pi_{ij}/k$, with

$$f^h = \frac{1}{T_t}\left(\frac{2}{3}(C_1 - 1) - (C_1 - 6)\frac{\overline{v^2}}{k}\right) + C_2 \frac{P_k}{k}, \tag{5.23}$$

where C_1 a constant coefficient.

For turbulent viscoelastic flows, the polymers modify the fluctuating pressure and hence the pressure–strain correlations. The pressure–strain redistribution of turbulent kinetic energy among Reynolds stress components is the source of wall-normal velocity fluctuations, which in turn inhibit the production of turbulent shear stress [67]. The viscoelastic contribution to the pressure-strain is given by $\Pi^V_{v^2} = f^V k$. This leads to the governing equation for f in turbulent viscoelastic flows represented as

$$f - L_t^2 \frac{\partial^2 f}{\partial x_j \partial x_j} = f^h + f^V, \tag{5.24}$$

with the length scale defined as,

$$L_t^2 = C_L^2 \max\left\{\frac{k^3}{\varepsilon^2}, C_\eta^2\sqrt{\frac{\nu_s^3}{\varepsilon}}\right\}, \tag{5.25}$$

where C_L and C_η are constant coefficients. Note that f^V requires a suitable closure model.

5.2.2 Streamwise vorticity equation

The origins of mean secondary flow in fully developed turbulent polymer duct flow are found within the mean streamwise vorticity, ω_x, transport equation (see Appendix of [75]),

$$\frac{\partial\overline{\omega}_x}{\partial t} = \underbrace{\overline{v}\frac{\partial\overline{\omega}_x}{\partial y} + \overline{w}\frac{\partial\overline{\omega}_x}{\partial z}}_{C} + \underbrace{\frac{\partial^2}{\partial y\partial z}(\overline{w'w'} - \overline{v'v'})}_{A} \tag{5.26}$$

$$+ \underbrace{\left(\frac{\partial^2}{\partial y^2} - \frac{\partial^2}{\partial z^2}\right)\overline{v'w'}}_{D} \underbrace{- \frac{\beta}{Re}\left(\frac{\partial^2}{\partial y^2} + \frac{\partial^2}{\partial z^2}\right)\overline{\omega}_x}_{V} \tag{5.27}$$

$$\underbrace{- \frac{1-\beta}{Re}\left(\frac{\partial^2\overline{\tau}_{23}^p}{\partial y^2} + \frac{\partial^2\overline{\tau}_{33}^p}{\partial y\partial z} - \frac{\partial^2\overline{\tau}_{22}^p}{\partial y\partial z} - \frac{\partial^2\overline{\tau}_{23}^p}{\partial z^2}\right)}_{P}, \tag{5.28}$$

where C is the convection of the mean vorticity by the secondary motion; A is the production term associated with the anisotropy of the in-plane normal stresses; D is the production/dissipation term due to the cross-stream Reynolds stress component, $\overline{v'w'}$; V is the viscous dissipation and P is the polymeric contribution.

The budget analysis of Equation (5.26) in polymeric square duct flow can be viewed in Figure 13 of [75]. It is found that the dominant contributions in both Newtonian and polymeric flows are from the production of in-plane anisotropy, A, and viscous dissipation, V. The production of cross-stream Reynolds stress, D, although not negligible, is over 10 times smaller in magnitude than A. Thus it will be neglected in this study. The convection term, C, along with P are negligible. It is interesting to note that although the polymeric stress contribution to $\overline{\omega_x}$ is small in amplitude, its presence produces macroscopic changes to the flow, by reducing the anisotropy of the in-plane velocity fluctuations.

Figure 5.1 shows DNS data [14, 40, 56] of the in-plane anisotropy in channel flow for increasing DR. There is a steady decrease and shift away from the wall as DR increases. As long as the viscoelastic closures are robust for capturing $\overline{w'w'}$ and $\overline{v'v'}$, then the shift of the secondary flow towards the centre of the square duct for increasing DR will feature.

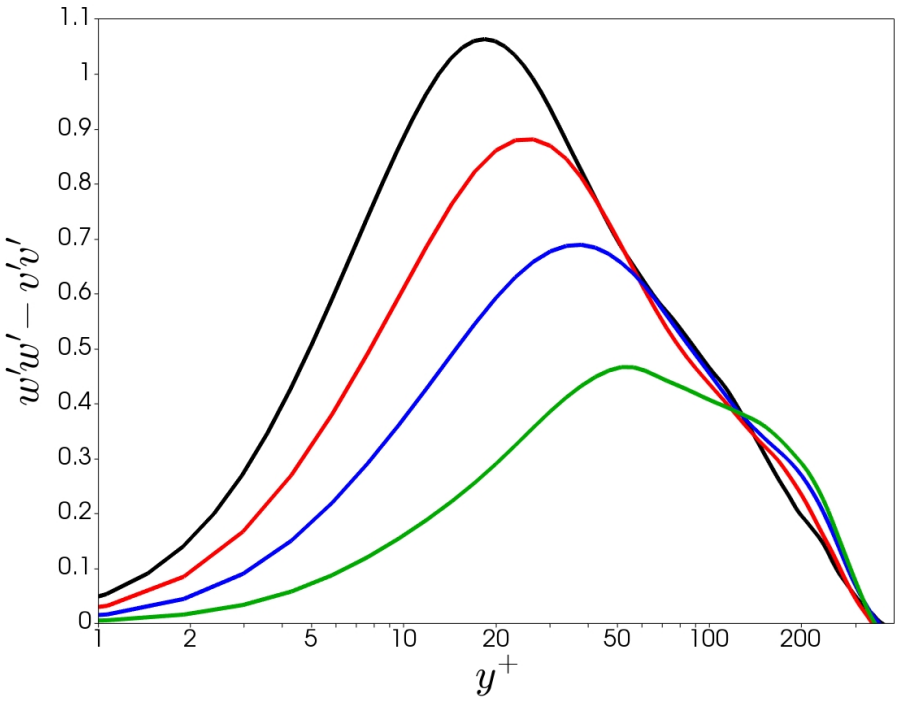

Figure 5.1: DNS data [14, 40, 56] of the in-plane anisotropy, $\overline{w'w'} - \overline{v'v'}$, in fully developed channel flow at $Re_{\tau_0} = 395$ with lines: Newtonian (black); 18% DR (red); 37% DR (blue) and 48% (green).

5.3 Development of viscoelastic closures

In this section, the viscoelastic closures identified in the previous section are developed to predict turbulent polymer flows in channel and square ducts. The turbulent viscoelastic model in channel flow is assessed against DNS data case 'A' [40], DR=18% ($Re_{\tau_0} = 395$, $Wi_{\tau_0} = 25$, $L^2 = 900$, $\beta = 0.9$), and then subsequently qualitatively assessed against square duct flow DNS data [75] with the same rheological parameters.

5.3.1 Closures for the conformation tensor

To compute the polymer stress, we need to calculate the components of the conformation tensor, C_{ij}, which are computed with the Reynolds Averaged Conformation Evolution (RACE), Equation (5.4). The set of analytical equations for fully developed channel flow can be viewed in Appendix 1 of [38]. In square ducts, there are walls in the y and z directions — such that the polymer shear stress can be written as,

$$\overline{\tau}_{xy,\mathrm{p}} + \overline{\tau}_{xz,\mathrm{p}} = \frac{\nu_p}{\lambda} f(C_{kk})(C_{xy} + C_{xz}) = \nu_p (NLT_{xy} + NLT_{xz}) + \frac{\nu_p}{f(C_{mm})} \left((\lambda NLT_{yy} + 1) \frac{\mathrm{d}U}{\mathrm{d}y} + (\lambda NLT_{zz} + 1) \frac{\mathrm{d}U}{\mathrm{d}z} \right). \tag{5.29}$$

For fully developed channel flow, the xz and zz terms are zero. As a result of the square duct symmetry along $y = z$, the terms in $\overline{\tau}_{xy,\mathrm{p}}$ and $\overline{\tau}_{xz,\mathrm{p}}$ are identical. Going forward, only $\overline{\tau}_{xy,\mathrm{p}}$ is referred to WLOG.

In order to obtain predictions for the polymer shear stress in channel and duct flow, one requires a closure model for C_{xy} and C_{kk}. An expression for C_{xy} can be derived from Eq (5.29) viz,

$$C_{xy} = \underbrace{\frac{\lambda}{f(C_{kk})}\left(\frac{\lambda NLT_{yy}+1}{f(C_{mm})}\right)\frac{\mathrm{d}U}{\mathrm{d}y}}_{I} + \underbrace{\frac{\lambda}{f(C_{kk})}NLT_{xy}}_{II}. \tag{5.30}$$

The $NLT_{\overline{v^2}}$ and $NLT_{x\overline{v}}$ terms both require adequate closure for accurate predictions of $C_{x\overline{v}}$. The stretching of the polymer chains is accounted for by NLT_{kk}, which is dominated by the xx component, as the chains tend to align with the mean streamwise vortices or enstrophy [59]. Figure 5.2 plots *a priori* DNS data of the C_{xy} term and its parts, I and II, in fully developed channel flow at $Re_{\tau_0} = 395$ with IDR. There is a discrepancy between the near wall values and the expected value, which can be accounted for by the increased numerical diffusion found in the early DNS studies [56, 61]. Term I of Eq (5.30) is dependent on the transverse NLT_{yy} component, with term II proportional to counter shear component, NLT_{xy}

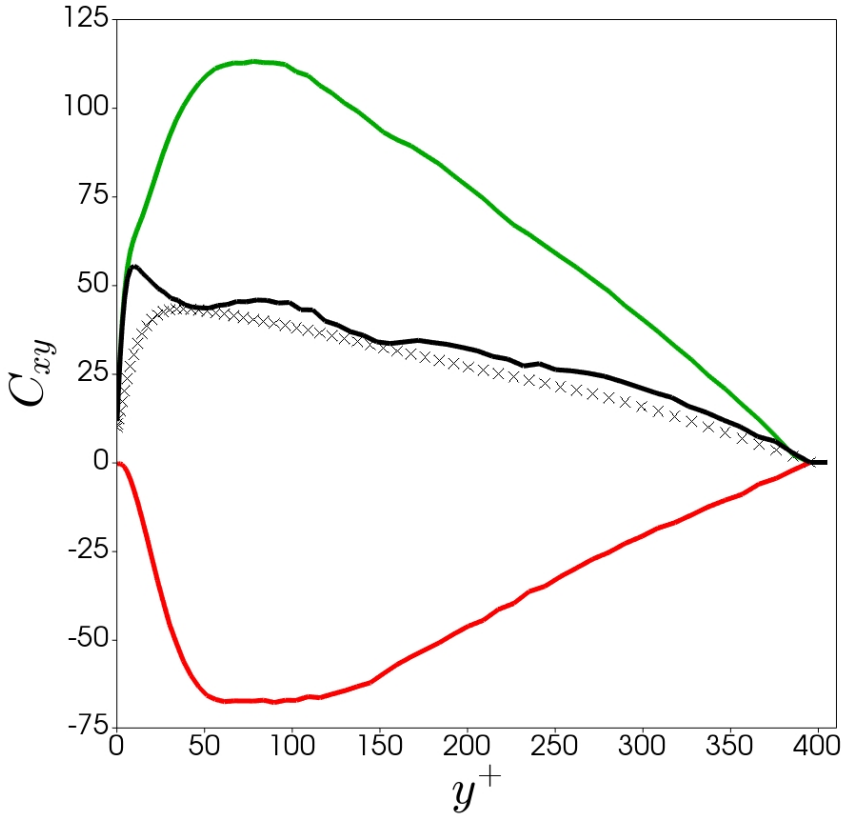

Figure 5.2: Comparison of the C_{xy} component with DNS data [61] at DR=37% ($Re_{\tau_0} = 395$, $Wi_{\tau_0} = 100$, $L^2 = 900$): ($\times$) DNS data, green line is term I in Equation (5.29), red line is term II in Equation (5.29), black line is the sum of term I and term II in Equation (5.29).

NLT_{ij}

Previous closure models derived for the NLT_{ij} term in the literature are here discussed, and guide us to the model applied in this work.

Masoudian et al. [40] proposes a Boussinesq-like stress strain relationship with the local eddy viscosity, $f_N = \nu_T/\nu_0$, and mean flow distortion term, M_{ij}, such that

$$NLT_{ij}^{\text{Mas}} = f_N M_{ij}. \tag{5.31}$$

In fully-developed channel flow, the non-zero components of M_{ij} are xx and xy. In the formulation by Masoudian et al. [40], $NLT_{yy} = 0$, and thus $C_{yy} = 0$ in the bulk of the flow. This requires NLT_{xy} to have the opposite sign to account for the calculation of C_{xy}.

In chapter 3 and 4, the NLT_{ij} closure was developed to capture all the individual components. The more general formulation is here presented,

$$NLT^{\text{Chapter 3,4}} = -\underbrace{C_{N1} f_N^{1/4} M_{ij}}_{shear} + \underbrace{A t_i t_j}_{streamwise} + \underbrace{B n_i n_j}_{transverse} + \underbrace{g(B)(\delta_{ij} - t_i t_j - n_i n_j)}_{spanwise}, \tag{5.32}$$

with

$$A = C_{N2}\frac{k}{\nu_0}\sqrt{\frac{LM_{nn}}{\gamma}} \quad \text{and} \quad B = C_{N3} f_N \frac{\lambda\sqrt{L}\varepsilon^N}{\nu_0 f(C_{mm})}. \tag{5.33}$$

The first term in Equation (5.32) is responsible for the shear component and near-wall negative streamwise component, which according to Dubief et al. [60], is the region where polymers inject energy into turbulence. The closure has the same principles as Masoudian et al. [16, 40], but here with the appropriate sign. The second term calculates the dominant streamwise polymer stretch contribution, modelled with A. The third term represents the transverse component, responsible for NLT_{v^2} in the polymer stress tensor (Equation (5.29)). In the original models [99, 108], this term was set to $B\delta_{ij}$ with $g(B) = B$, so that $NLT_{yy} = NLT_{zz}$. Given the similarity of the NLT_{zz} component with NLT_{yy} for varying DR regimes (Figure 5.3), the function $g(B)$ can be applied. The spanwise component has small impact on model predictions [38], and can be neglected.

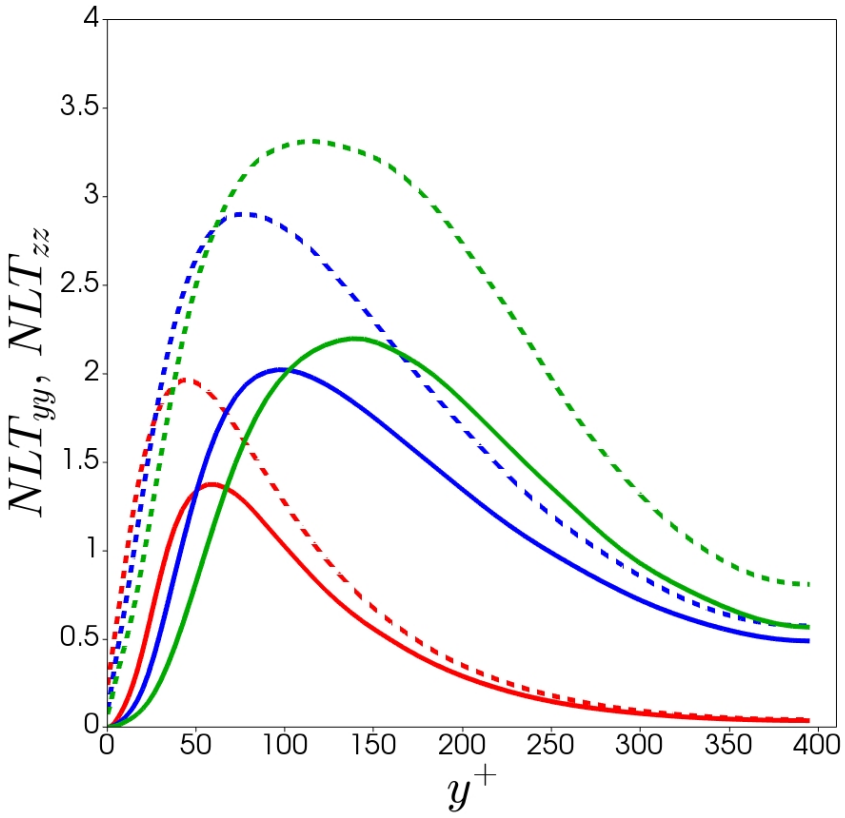

Figure 5.3: Comparison of the NLT_{yy} (solid line) and NLT_{zz} (dashed line) component with DNS data [61] in fully developed channel flow at $Re_{\tau_0} = 395$ with DR= 18% (red), 37% (blue), 51% (green).

It was demonstrated by Masoudian et al. [69] that NLT_{ij} and $\overline{u_i' u_j'}$ have similarity of events, based on their iso-surface projections. This can be approximated with the following assumption for the NLT_{ij} normal components as,

$$NLT_{ij} \sim \frac{u_i u_j}{2k} NLT_{kk}. \tag{5.34}$$

A priori DNS test of Equation (5.34) at 18% DR can be viewed in Figure 5.4. The model shows good correlation with the DNS, capturing peak locations and trends well with the anisotropy of the Reynolds stress tensor distributing NLT_{kk}. In duct flows, the NLT_{zz} component has negligible impact on overall flow predictions [114], thus a full scale model may not be appropriate. Here, an alternative is formed based on the natural wall scaling, $\overline{v^2}/k$. One can apply this principle to NLT_{kk} and NLT_{v^2}. The scaling can be argued with v^2/k such that,

$$NLT_{v^2} \sim \frac{v^2}{k} NLT_{kk}. \tag{5.35}$$

Figure 5.5 shows *a priori* DNS analysis of Equation (5.35) for 18% (LDR), 37% (IDR) and 51% (HDR). The approximation is strong for LDR, with some over dampening at HDR.

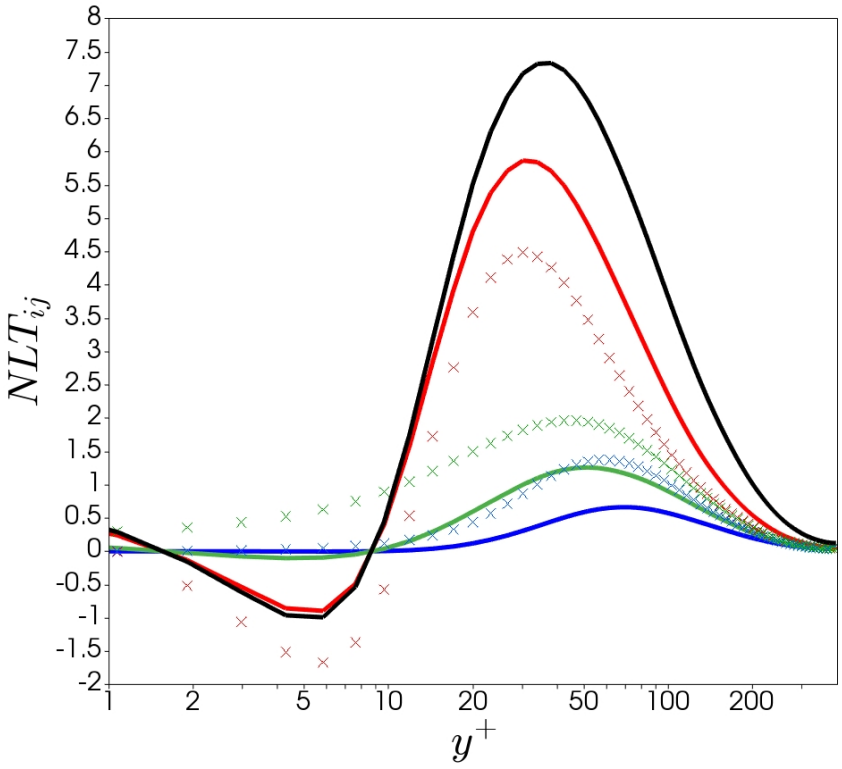

Figure 5.4: *A priori* DNS data of NLT_{ij} (Equation (5.34)) at 18% DR in fully developed channel flow. Symbols ($\times$) and solid lines are the LHS and RHS of Equation (5.34), respectively. Each normal component is represented by colours: *kk* (black), *xx* (red), *yy* (blue), *zz* (green).

The second approximation equates the component of dominant stretch, NLT_{xx}, with the total stretch such that,

$$NLT_{kk} \approx NLT_{ij} t_i t_j, \tag{5.36}$$

where t_i is given by Equation (5.12). This is inspired by the fact that polymers tend to align and stretch with the direction of mean flow or streamwise enstrophy, $t_i t_j \sim \omega_i^2$ [59]. The closure model for the trace of NLT_{ij} is given by that of Masoudian et al. [16] such that $NLT_{kk} = f_N M_{kk}$.

The final term requiring consideration for NLT_{ij} is the shear component, NLT_{xy}. This term appears in the polymer shear stress (Equation (5.29)) and is strictly negative. There is no clear explanation in the literature for the mechanistic role of this term, although it has some energy transfer from the polymer to the turbulence [67]. In [70, 99, 108], this term is modelled with dependence on the local eddy viscosity, ν_T/ν_0 and mean flow distortion term, M_{ij} (see first term in Equation (5.32)), and is neglected in the $v^2 - f$ models [16, 39, 40]. After robust testing in square duct flow, it is found that the NLT_{xy} term can lead to numerical instability and spurious results in polymer shear stress calculations, caused by term II becoming greater than term I in Equation (5.29) within regions of the domain. A new closure here is considered. Based on Figure 5.2, the transverse component, NLT_{v^2}, modelled by Equation (5.35), can be cast with a reduced pseudo constant which accounts

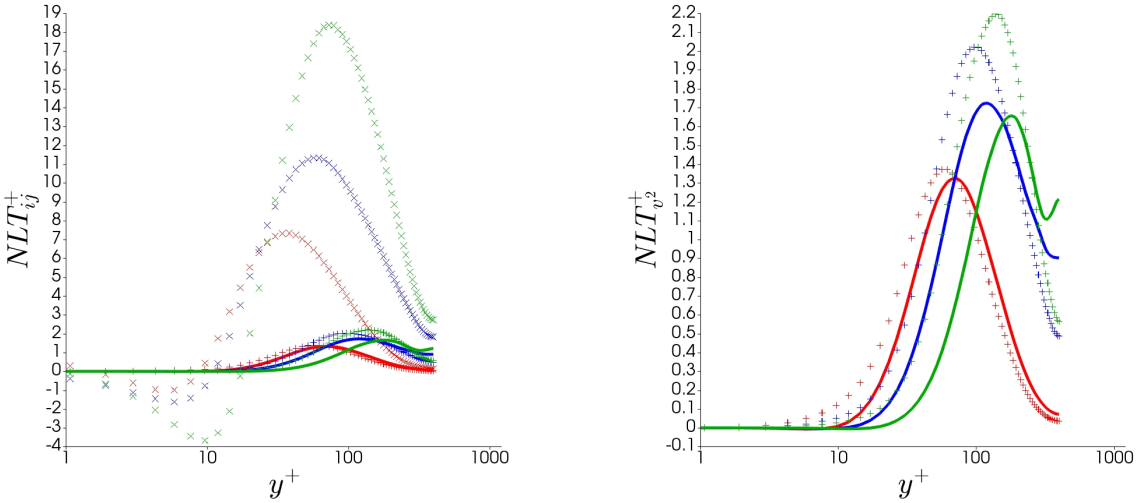

Figure 5.5: Comparison of the DNS data for NLT_{v^2} and the model of Equation (5.35) in fully developed channel flow with LDR (red), IDR (blue) and HDR (green): NLT_{kk} ($\times$), NLT_{v^2} (+), Equation (5.35).

for the countering effects of NLT_{xy} on the polymer stress (see red line in Figure 5.2).

The final form of NLT_{ij} is given by,

$$NLT_{ij} = C_{N1} f_N M_{kk} \left(t_i t_j + C_{N2} \frac{v^2}{k} n_i n_j \right), \tag{5.37}$$

where $C_{N1} = 0.6$ and $C_{N2} = 0.45$.

The performance of the NLT_{ij} model can be analysed in Figure 5.6 by comparing current model predictions against DNS data at DR=18% in fully developed channel flow, then subsequently assessed in square duct flow for the equivalent case. Figure 5.6a & 5.6c plot the polymer stretching term in channel flow and square ducts, respectively. The magnitude and peak locations are well captured compared to the DNS data. In square duct flow, the symmetry along $y = z$, and the reduction in magnitude towards the duct corner ($y = z$) is exhibited. Figure 5.6b & 5.6d plot the transverse component in channel flow and square ducts, respectively. The reduced magnitude accounts for the countering, $NLT_{x\bar{v}}$ term, with general features captured well with the DNS, and extended features in square ducts. The closure has great simplicity and with strong robustness compared to previous models [99, 108]. The effect of NLT_{ij} on the mean conformation tensor, C_{ij}, are analysed in the results section against DNS data for both channel flow and square duct flow.

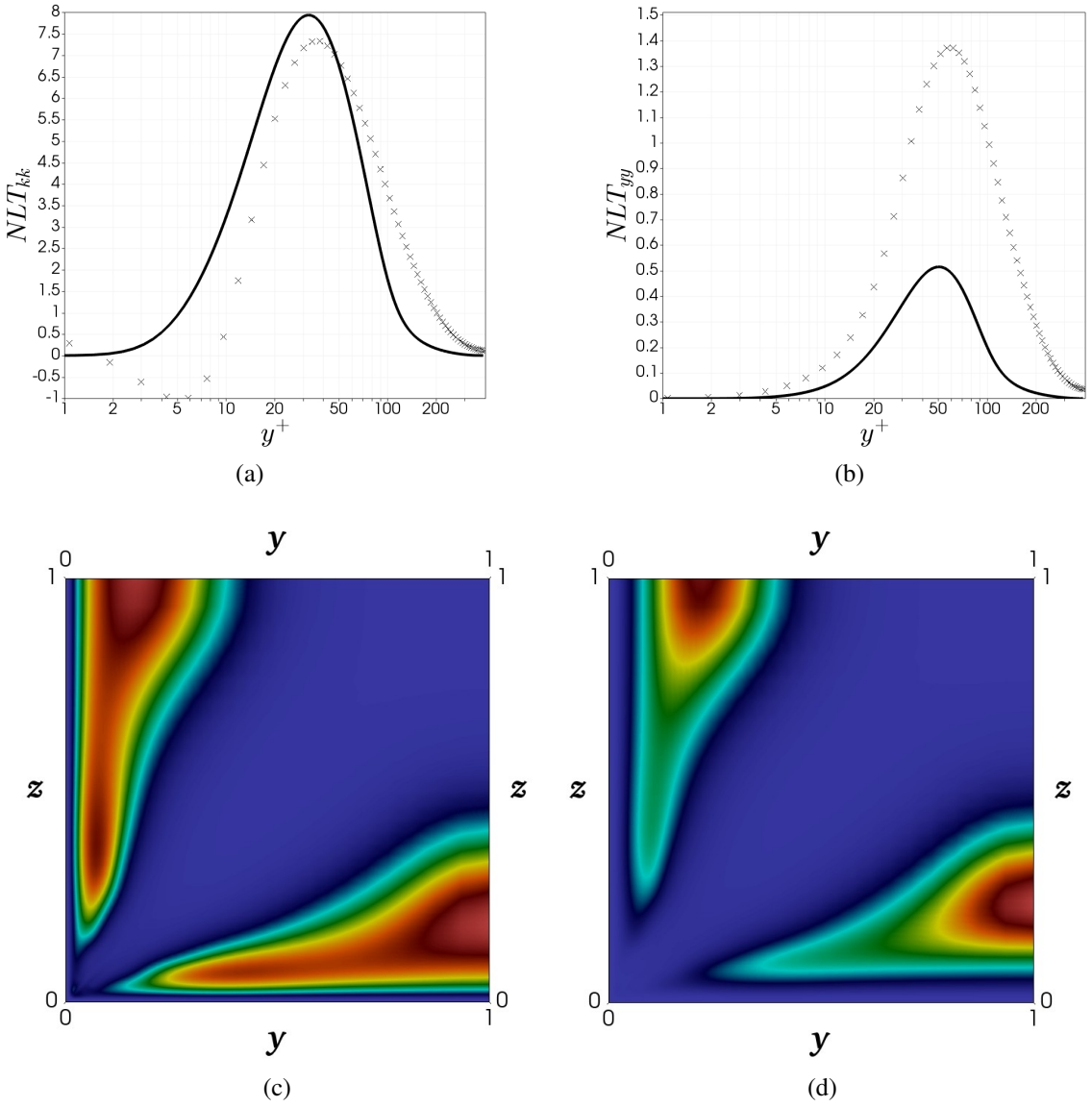

Figure 5.6: Comparison of the NLT_{ij} model predictions (solid lines) with DNS data case DR=18% ($Re_{\tau_0} = 395$, $Wi_{\tau_0} = 25$, $L^2 = 900$, $\beta = 0.9$) (crosses) in fully developed channel flow (a, b), and square duct model predictions (c, d): (a) NLT_{kk}, (b) NLT_{yy}, (c) NLT_{kk}, (d) $NLT_{yy} + NLT_{zz}$. The colour scale ranges from 0 (blue) to 10.4 (red) for (c), and 0 (blue) to 1.2 (red) for (d).

5.3.2 Closure for Reynolds Stresses

The redistribution of the turbulent kinetic energy is achieved by the N_{ij} term (Equation (5.8)). The model depends on the knowledge of k and v^2 which are separately addressed for viscoelastic flow. The $\overline{w'^2}$ term requires a viscoelastic model, as predictions are important in the production of streamwise vorticity. The functional form of the Newtonian model [91] is given by,

$$\overline{w'^2} = \frac{f_d}{2}\left(\overline{u'^2} + \overline{v'^2}\right). \tag{5.38}$$

The damping function, f_d (Equation (5.9)), was introduced to ensure the correct asymptotic behaviour of the components parallel to the wall, so that $\overline{u'^2} \propto y^2$ and $\overline{w'^2} \propto y^2$. This was achieved by setting the damping function to a constant value of $f_{d0} = 0.3$ until $y^+ \approx 10$ given the DNS data [14]. Above this y^+ value, the damping function is modelled as a function of v^2/k. For turbulent viscoelastic flow, $\overline{w'^2}$ reduces in the near wall for increasing DR, in a similar fashion to $\overline{v'^2}$. This is approximated *ad hoc* with the term $f_{d0} = 0.3/(1+(L/30)^2)$, given that the maximum chain extensibility, L^2, has some proportionality to *DR*. Figure 5.7 shows *a priori* DNS analysis of $\overline{w'^2}$ for case E, with good correlation and simplicity of the modelled term. The adjusted model is presented as,

$$f_d^V = \min\left[\max\left(\left(\frac{3}{2}\frac{v^2}{k}\right)^{1/2}, \frac{0.3}{1+(L/30)^2}\right), 1.0\right]. \tag{5.39}$$

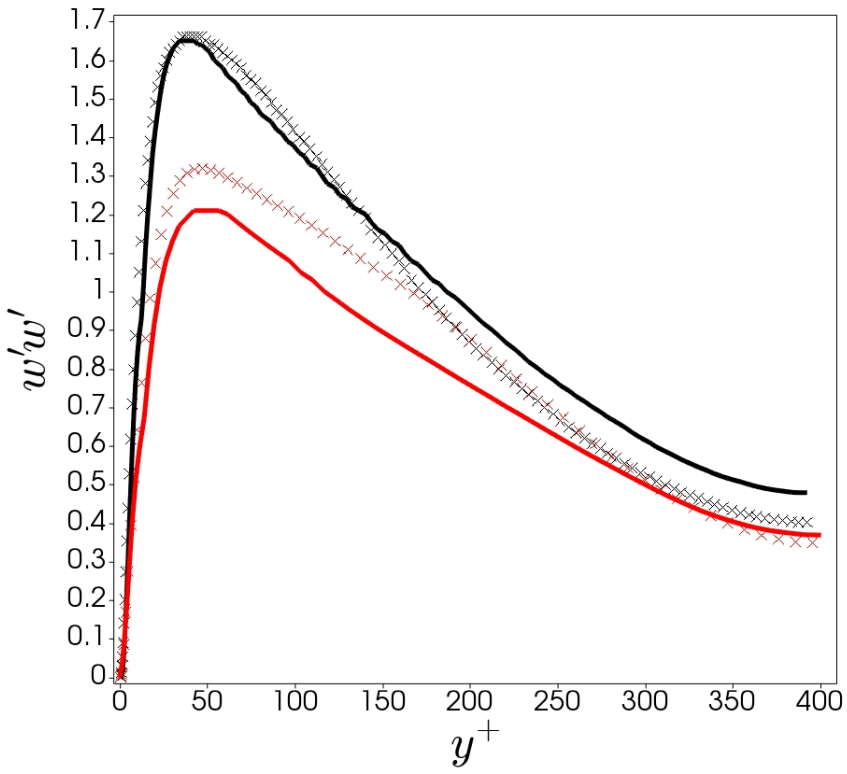

Figure 5.7: Comparison of the spanwise Reynolds stress component, w'^2, in fully developed channel flow with DNS data [14, 56] (crosses) and *a priori* model (solid lines) given by Equation (5.39). Newtonian in black (DR=0%, $Re_{\tau_0} = 395$), and LDR in red (DR=18%, $Re_{\tau_0} = 395$, $Wi_{\tau_0} = 25$, $L^2 = 900$, $\beta = 0.9$).

5.3.3 Closures for the transport of k, ε, v^2 and f

A budget analysis for each term in the k transport equation was performed by Pinho et al. [38] for different regimes of DR. They demonstrated that the magnitude of Q^V has more impact on the overall budget in the IDR, and also developed a closure. In the HDR, the amplitude of Q^V is the same as ε^V but has a different location in the buffer layer, in which the effects of Q^V are overcome by turbulent diffusion, revealing negligible effects to overall flow predictions. Previous models [16, 40, 70, 99, 108] chose to neglect the Q^V contributions, and it is also not included here as well.

The closure model for the viscoelastic stress work is well founded [38, 69, 99], and is presented as,

$$\varepsilon^V_{ij} = \frac{\nu_p}{2\lambda} f(C_{mm}) NLT_{ij}, \tag{5.40}$$

so that the viscoelastic closure in the k transport is,

$$\varepsilon^V_{kk} \equiv \varepsilon^V = \frac{\nu_p}{2\lambda} f(C_{mm}) NLT_{kk}. \tag{5.41}$$

The viscoelastic contribution to the dissipation equation, E^V, is modelled in the same

fashion as previous models [16, 40, 68],

$$E^V = \frac{C_{\varepsilon 1}\varepsilon^V}{T_t}. \tag{5.42}$$

The transverse viscoelastic stress work, $\varepsilon^V_{v^2}$, in the transport of v^2 can be simply represented by importing the NLT_{v^2} component into Equation (5.41), or more simply as

$$\varepsilon^V_{v^2} = C'_{N2}\frac{v^2}{k}\varepsilon^V. \tag{5.43}$$

The constant coefficient, C'_{N2}, is such that $C'_{N2} > C_{N2}$, which gives a more realistic representation of the NLT_{v^2} magnitude (see Figure 5.6b). This is in contrast to the *ad hoc* developments of previous models [16, 40, 108],

$$\left(\varepsilon^V_{v^2}\right)^{\text{Chapter 4}} = 0.001(1-\beta)\sqrt{L}f_N\varepsilon \quad \text{and} \quad \left(\varepsilon^V_{v^2}\right)^{\text{Mas}} = 0.002L[f(C_{mm})]^2 kf. \tag{5.44}$$

Given Equation (5.43), the transport equation of $\overline{v^2}$ can be recast as:

$$U_j\frac{\partial\overline{v^2}}{\partial x_j} = \frac{\partial}{\partial x_j}\left[\left(\nu_s + \frac{\nu_T}{\sigma_k}\right)\frac{\partial\overline{v^2}}{\partial x_j}\right] + kf - \left(6\varepsilon + C'_{N2}\varepsilon^V\right)\frac{\overline{v^2}}{k}. \tag{5.45}$$

The reduction of v^2 in the near wall region as DR increases is the primary source for reduced Reynolds shear stresses. The effect of $\varepsilon^V_{v^2}$ on the transport of $\overline{v^2}$ is away from the wall, meaning that its impact is less significant to the near wall phenomena. With only a closure model for $\varepsilon^V_{v^2}$, the turbulent kinetic energy reduces as DR increases, which is counter to the DNS findings. The reason is that the near wall viscoelastic effects in Equation (5.45) are accounted for by a reduced production term, kf. Given that k increases with DR, there must be a substantial reduction in the redistribution term, f. For the rest of this study, C'_{N2} is set to 0, but the theory is described here for complete context.

In this thesis, the viscoelastic effects for v^2 are captured via implicit changes in f. The modification of the fluctuating pressure field represents implicit polymer effects which limit pressure–strain redistribution and hence the production of turbulent shear stress. Limited closure models are available for the pressure-strain term in turbulent viscoelastic flows (denoted f^V in Equation (5.24)). Leighton et al. [67] first produced a closure for f^V proportional to the first term in f^h (Equation (5.23)), with some viscoelastic quantities. In their RSM, the closure required an additional damping function, and was later found to completely relaminarise the flow at HDR [39]. Iaccarino et al. [39] proposed a modification to the production term to account for the implicit effects of the polymer chains, with an effective rate of production, $P_k - \varepsilon^V$, where ε^V represents the energy transfer related to the polymer stretching. The closures developed in the model were shown to perform poorly, with excessive damping in the log-layer [16]. Masoudian et al. [16, 40] mod-

elled v^2 *ad hoc* by recasting the production term, kf, to include viscoelastic effects via $kf(1-g)$, where g are some viscoelastic quantities. The difficulty with this closure is for when $g > 1$ in any part of the flow domain, the pressure term becomes negative and will cause complete flow relaminarisation or code instability, as pointed out by [40, 95]. Later, slight improvements are made to the closure parameters [40], although the same functional form is maintained.

Here a simple *ad hoc* closure is proposed which recasts the production term constant to, $C_2/(1+(L/30)^2)$, where L^2 has some proportionality to DR. Thus the transport of f is given as

$$f - L_t^2 \frac{\partial^2 f}{\partial x_j \partial x_j} = \frac{1}{T_t}\left(\frac{2}{3}(C_1 - 1) - (C_1 - 6)\frac{\overline{v^2}}{k}\right) + \frac{C_2}{1+(L/30)^2}\frac{P_k}{k}. \tag{5.46}$$

This simple closure is more robust than previous models which is necessary in square duct flows. The effects can be viewed in the results section on the mean flow field.

Coefficient	Value
Newtonian:	
C_μ	0.22
σ_k	1.0
σ_ε	1.3
$C_{\varepsilon 1}$	$1.4\left[1+0.045\sqrt{k/\overline{v^2}}\right]$
$C_{\varepsilon 2}$	1.92
C_1	1.4
C_2	0.3
C_L	0.23
C_η	70.0
Viscoelastic:	
C_{N1}	0.6
C_{N2}	0.45

Table 5.1: List of model Newtonian and viscoelastic coefficients.

5.4 Summary of the present model

The governing equations with complete closure models that were developed in the previous sections are presented here. The model coefficients are summarised in Table 5.1.

Momentum equation:

$$U_j\frac{\partial U_i}{\partial x_j} = -\frac{\partial P}{\partial x_i} + \frac{\partial}{\partial x_j}\left((\beta\nu_0+\nu_T)\frac{\partial U_i}{\partial x_j} - kN_{ij}\right) + \frac{(1-\beta)\nu_0}{\lambda}\frac{\partial}{\partial x_j}\left(f(C_{mm})C_{ij}-\delta_{ij}\right), \tag{5.47}$$

where the eddy viscosity is

$$\nu_T = C_\mu \overline{v^2} T_t, \tag{5.48}$$

the normal Reynolds stress distribution term is

$$N_{ij} = \frac{2}{3}\delta_{ij} + \left(1 - \frac{3}{2}\frac{\overline{v^2}}{k}\right)\left(\frac{\delta_{ij}}{3} - n_i n_j\right) + \left(\frac{2 - f_d}{2 + f_d} - \frac{1}{2}\frac{\overline{v^2}}{k}\right)(2t_i t_j + n_i n_j - \delta_{ij}), \tag{5.49}$$

with

$$f_d = \min\left[\max\left(\left(\frac{3}{2}\frac{v^2}{k}\right)^{1/2}, \frac{0.3}{1 + (L/30)^2}\right), 1.0\right]. \tag{5.50}$$

The wall normal vector, n_i, and the normalised direction of mean vorticity, t_i, are given by Eqs. (5.10) and (5.12), respectively.

Conformation tensor transport equation:

$$\frac{DC_{ij}}{Dt} - M_{ij} - NLT_{ij} = -\frac{1}{\lambda}[f(C_{kk})C_{ij} - \delta_{ij}], \tag{5.51}$$

with

$$NLT_{ij} = C_{N1} f_N M_{kk}\left(t_i t_j + C_{N2}\frac{v^2}{k} n_i n_j\right), \tag{5.52}$$

where $f_N = \nu_T/\nu_0$ is the local eddy viscosity with constant coefficients $C_{N1} = 0.6$ and $C_{N2} = 0.45$.

Turbulent kinetic energy transport equation:

$$U_j\frac{\partial k}{\partial x_j} = \frac{\partial}{\partial x_j}\left[\left(\beta\nu_0 + \frac{\nu_T}{\sigma_k}\right)\frac{\partial k}{\partial x_j}\right] + \left(P_k - \varepsilon^V\right) - \varepsilon, \tag{5.53}$$

where $P_k = \overline{u_i' u_j'} S_{ij}$ and

$$\varepsilon^V \equiv \varepsilon^V_{kk} = \frac{\nu_p}{2\lambda} f(C_{mm}) NLT_{kk}. \tag{5.54}$$

Dissipation transport equation:

$$U_j\frac{\partial \varepsilon}{\partial x_j} = \frac{\partial}{\partial x_j}\left[\left(\beta\nu_0 + \frac{\nu_T}{\sigma_\varepsilon}\right)\frac{\partial \varepsilon}{\partial x_j}\right] + \frac{C_{\varepsilon 1}(P_k - \varepsilon^V) - C_{\varepsilon 2}\varepsilon}{T_t} \tag{5.55}$$

Wall normal Reynolds stress transport equation:

$$U_j\frac{\partial \overline{v^2}}{\partial x_j} = \frac{\partial}{\partial x_j}\left[\left(\beta\nu_0 + \frac{\nu_T}{\sigma_k}\right)\frac{\partial \overline{v^2}}{\partial x_j}\right] + kf - 6\frac{\varepsilon}{k}\overline{v^2} \tag{5.56}$$

Elliptic relaxation, f, transport equation

$$f - L_t^2 \frac{\partial^2 f}{\partial x_j \partial x_j} = \frac{1}{T_t}\left(\frac{2}{3}(C_1 - 1) - (C_1 - 6)\frac{\overline{v^2}}{k}\right) + \frac{C_2}{1 + (L/30)^2}\frac{P_k}{k}. \tag{5.57}$$

5.5 Numerical procedure

The numerical procedure is more extensively explained in chapter 2. Here a summary is given for the context of this chapter.

In order to examine the viscoelastic turbulence model against the available DNS data identified within the literature, a finite volume C++ code was developed within the OpenFOAM software (See Chapter 2). For both Newtonian and polymeric flows, a fixed pressure gradient (ex post facto [9]) is applied in the streamwise (x) direction, such that

$$\frac{\partial P}{\partial x} \equiv \frac{\Delta P}{\Delta x} = \frac{\langle \tau_w \rangle}{R_h}, \tag{5.58}$$

where $R_h = A_h/P_h$ is the hydraulic radius, A_h is the cross-sectional area of the geometry, P_h is the 'wetted' perimeter, and $\langle \tau_w \rangle$ is the average wall shear stress. For channel flow, $R_h = 4h^2/4h = h$, where h is the channel half-height. For square duct flow, $R_h = 4h^2/8h = h/2$. Here h is set to 1 for simplicity. The mesh generated for the channel has a symmetry plane at the centre-line (middle) $y = h = 1$, and at both $y = h = 1$ and $z = h = 1$ for the square duct (see Figure 2.1). A total of 50 cells are assigned in the wall normal directions with approximately 10 cells located inside the viscous sub-layer ($y^+ \sim 10$). This ensures mesh independence as shown in [16].

The Poisson equation (Equation 5.11) which describes the normal directions is given by,

$$\nabla^2 \phi = -1 \quad \text{with} \quad \phi_{\mathrm{w}} = 0 \quad \text{and} \quad \frac{\partial \phi}{\partial x_i}|_{\partial\Omega} = 0, \tag{5.59}$$

where 'w' and '$\partial\Omega$' denote the wall and middle, respectively. The solutions to Equation (5.59) in channel flow and square ducts are $\phi(y) = \frac{1}{2}y(2h - y)$ and $\phi(y,z) = \frac{1}{2}(h^2 - y^2 - z^2)$, respectively. The wallDist functionality within OpenFOAM is utilised for defining the normalised wall tensor, $n_i n_j$, viz:

```
1 volScalarField y = wallDist(mesh_).y();
2 volVectorField ni = fvc::grad(y);
3 normal_ = symm(ni * ni);
```

This removes the need to solve ϕ as a pre-simulation process as required in [91].

A summary of the boundary conditions applied within OpenFOAM can be viewed in Table 2.2. The conformation tensor boundary condition is a Dirichlet condition which can be viewed in Chapter 2.

5.6 Results and discussion

Following the numerical procedure proposed in the previous section, the model performance is assessed against DNS data case 'A' [40], DR=18% ($Re_{\tau_0} = 395$, $Wi_{\tau_0} = 25$, $L^2 = 900$, $\beta = 0.9$), and then subsequently qualitatively assessed against square duct flow DNS data [75] with the same rheological parameters.

5.6.1 Analysis of C_{ij}

Figure 5.8 shows the model predictions of the conformation tensor trace (a, c) and shear component (b, d) in fully developed channel flow and square duct flow, respectively. The polymer extension, C_{kk} is well captured in the near wall region and buffer layer, where effects on the flow are dominant, which is a consequence of the NLT_{kk} closure formulated from Equation (5.37). These effects are translated to square duct flow, in which the symmetry holds along $y = z$, and the field diminishing towards the square duct corner ($y = z = 0$). Qualitative analysis of the DNS data (see Figure 8a in [75]) shows that the model predicts these key features. The polymer shear term, C_{xy}, matches well with DNS data for fully developed channel flow. The predictions are dominated by the NLT_{yy} model which is presented with a reduced pseudo constant (see Equation (5.37)). In square duct flow, the key features match well (see Figure 8c in [75]), such as the diminishing magnitude towards the square duct corner, and the negative peak below the $y = z$ line. It is important to note that the C_{xz} component (not shown here) demonstrates the same features as C_{xy} in square duct flow, with symmetry in $y = z$, as expected. The conformation tensor predictions are a consequence of the robustness of the NLT_{ij} closure model, depending on the distribution of the polymer stretch, NLT_{kk}, to the streamwise and transverse components, with two simple constant coefficients of O(1).

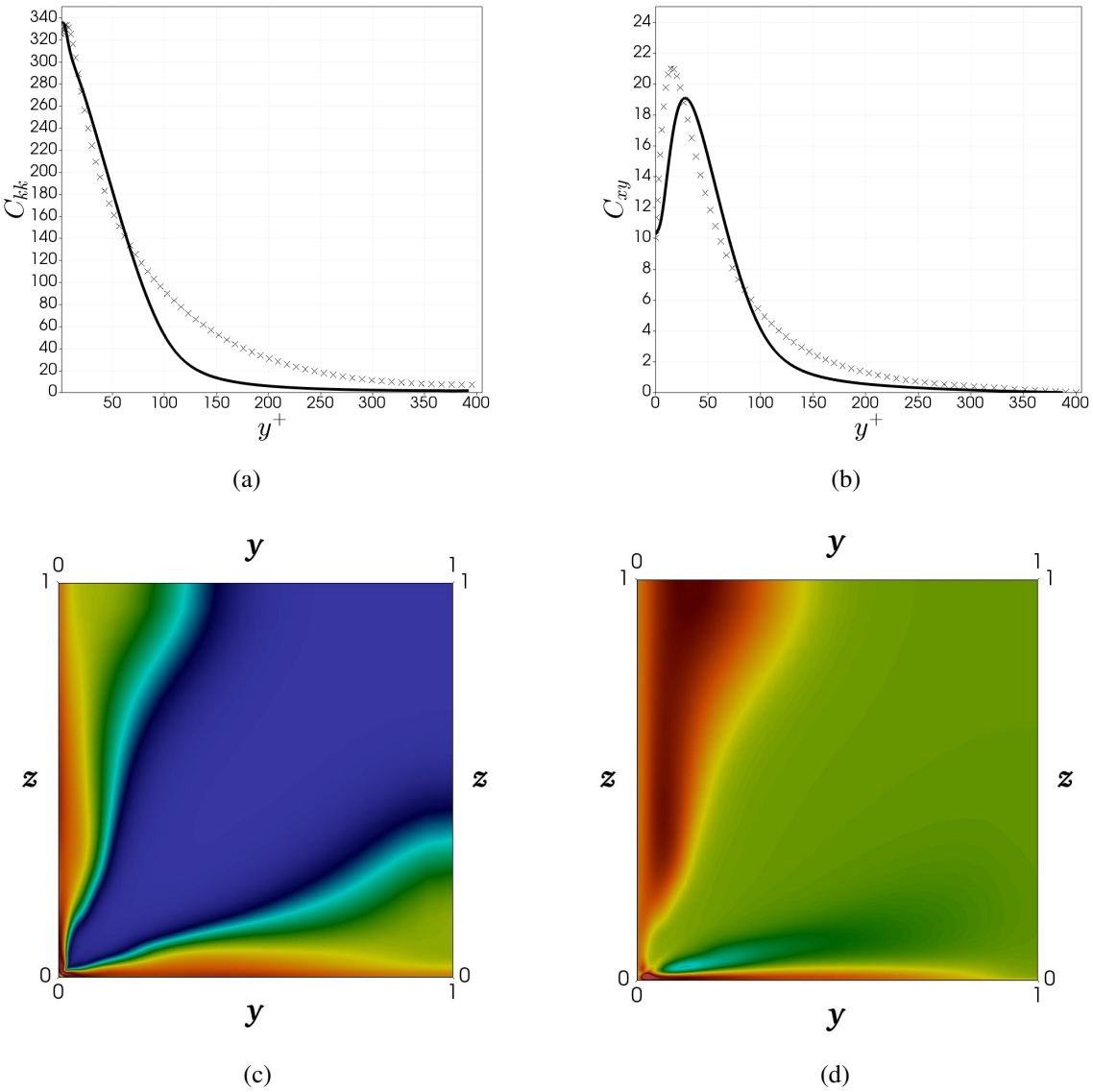

Figure 5.8: Comparison of the C_{ij} model predictions (solid lines) with DNS data case 'A' (crosses) in fully developed channel flow (a, b), and square duct model predictions (c, d): (a, c) C_{kk} and (b, d) C_{xy}. The colour scale ranges from 0 (blue) to 450 (red) for (c), and -30 (blue) to 30 (red) for (d).

5.6.2 Analysis of Reynolds stresses and dissipation rate

Figure 5.9 shows model predictions of the Reynolds Stress (a) normal components, (b) and shear component, in fully developed channel flow. The reduction in the $\overline{v'}^2$, $\overline{w'}^2$, and $\overline{u'v'}$ components are well captured, with the shift away from the wall into the buffer layer. The *ad hoc* closure model for f suppresses the production term based on implicit polymer effects, demonstrated here with a reduction in $\overline{v'}^2$. The effect of this is translated to the Reynolds shear stress via the eddy viscosity model, $\nu_T = C_\mu \overline{v'}^2 T_t$. The streamwise component, $\overline{u'}^2$, shows a slight decrease compared with the Newtonian case, although is of similar magnitude. The viscoelastic closure for f increases $\overline{u'}^2$ compared to if just a

Newtonian closure was used. Masoudian et al. [16] argues that the small increase of $\overline{u'}^2$ for polymer flows in some DNS data could be fictitious, given that the experimental findings [57] show similar magnitudes for both Newtonian and polymeric flows. This could be a consequence of the limitations of the FENE-P model [40, 57]. Figure 5.10 shows model predictions of (a, b) $\overline{v'}^2$, and (c, d) the Reynolds shear stress magnitude, in square duct flow for Newtonian and LDR. In both cases, the shift away from the wall and reduced magnitude are highlighted. These features translate well for both channel and square duct flow, which is a consequence of the simple and robust viscoelastic closures developed for $\overline{v'}^2$, $\overline{w'}^2$, and f.

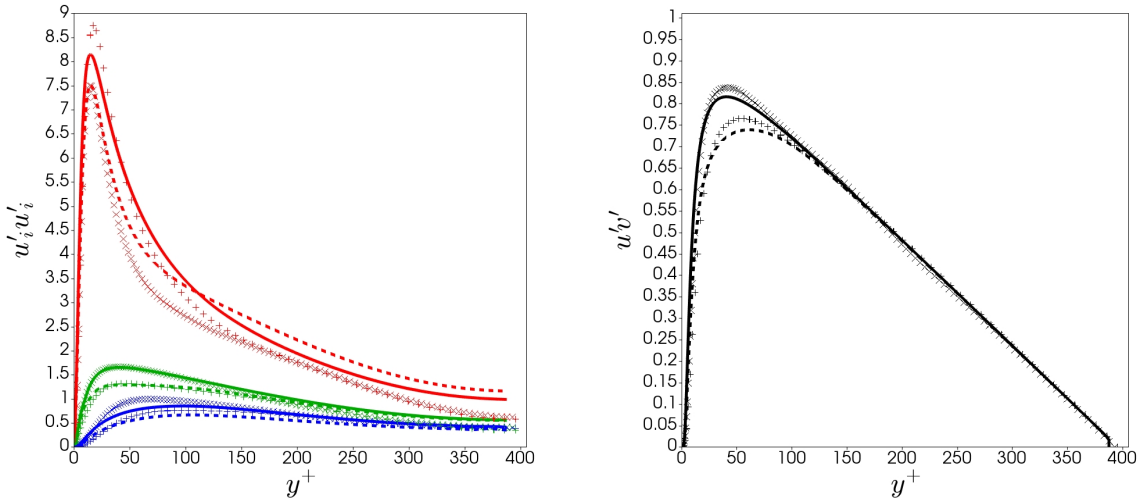

(a) (b)

Figure 5.9: Comparison of the $\overline{u_i'u_j'}$ model predictions (lines) with DNS data from Newtonian [14] (crosses) and case 'A' (plus) in fully developed channel flow. Each colour represents a different Reynolds stress component: (a) $\overline{u'u'}$ (red), $\overline{v'v'}$ (blue), $\overline{w'w'}$ (green); (b) $\overline{u'v'}$ (black). Solid lines are Newtonian [14]), and dashed lines are case 'A'.

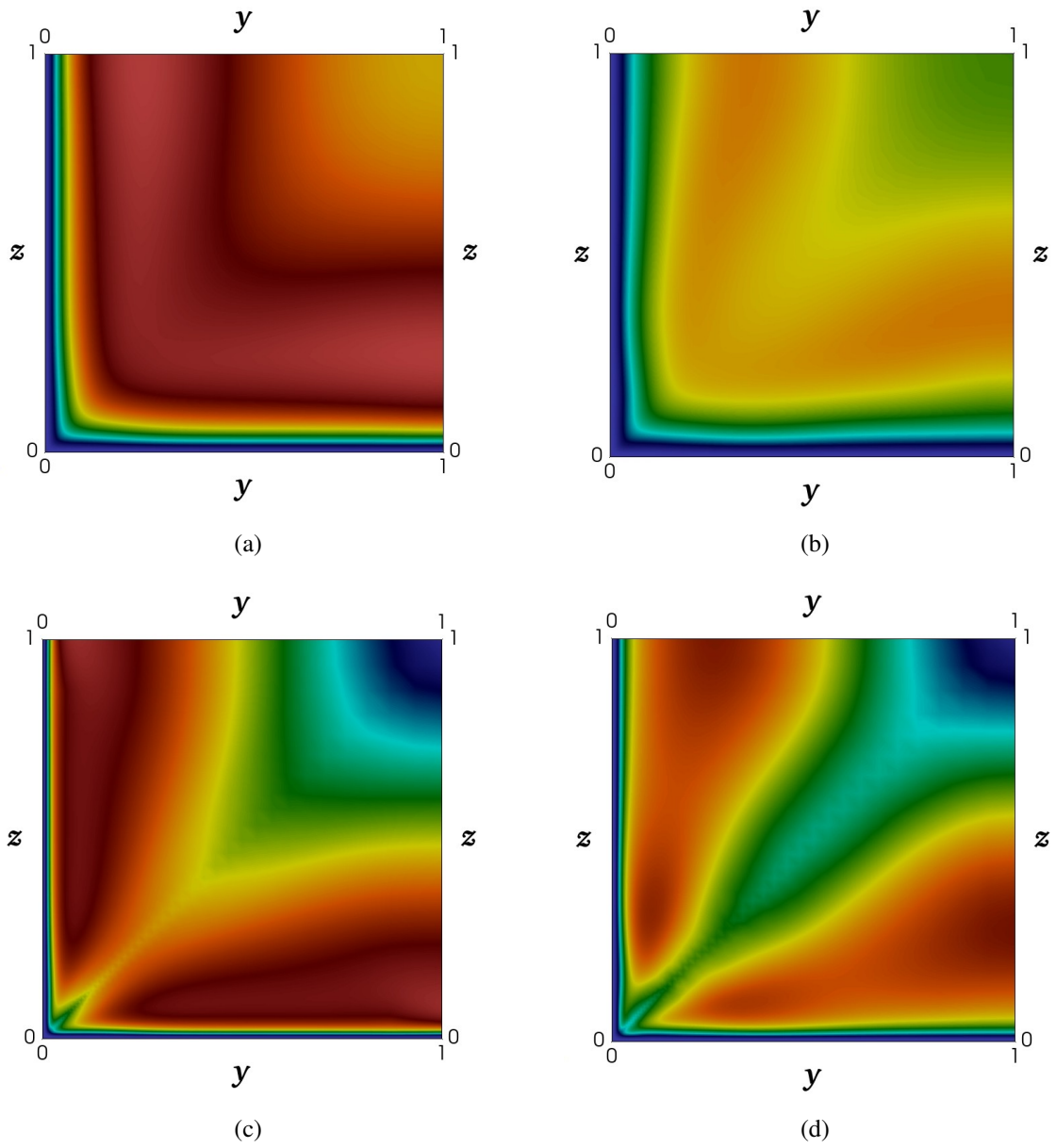

Figure 5.10: Model predictions of (a, b) wall Reynolds stress, $\overline{v^2}$, and (c, d) Reynolds shear stress magnitude, $\nu_T \sqrt{S_{pq} S_{pq}}$, in square duct flow with the same comparative flow conditions as DNS data case 'A': (a, c) Newtonian [14], and (b, d) LDR. The colour scale ranges from 0 (blue) to 1 (red) in all figures.

Figure 5.11 shows model predictions of the dissipation rate, ε^+, in (a) channel flow, and (b, c) square duct flow. The reduction in LDR is featured for both cases, which is captured with the well founded viscoelastic closure in E^V.

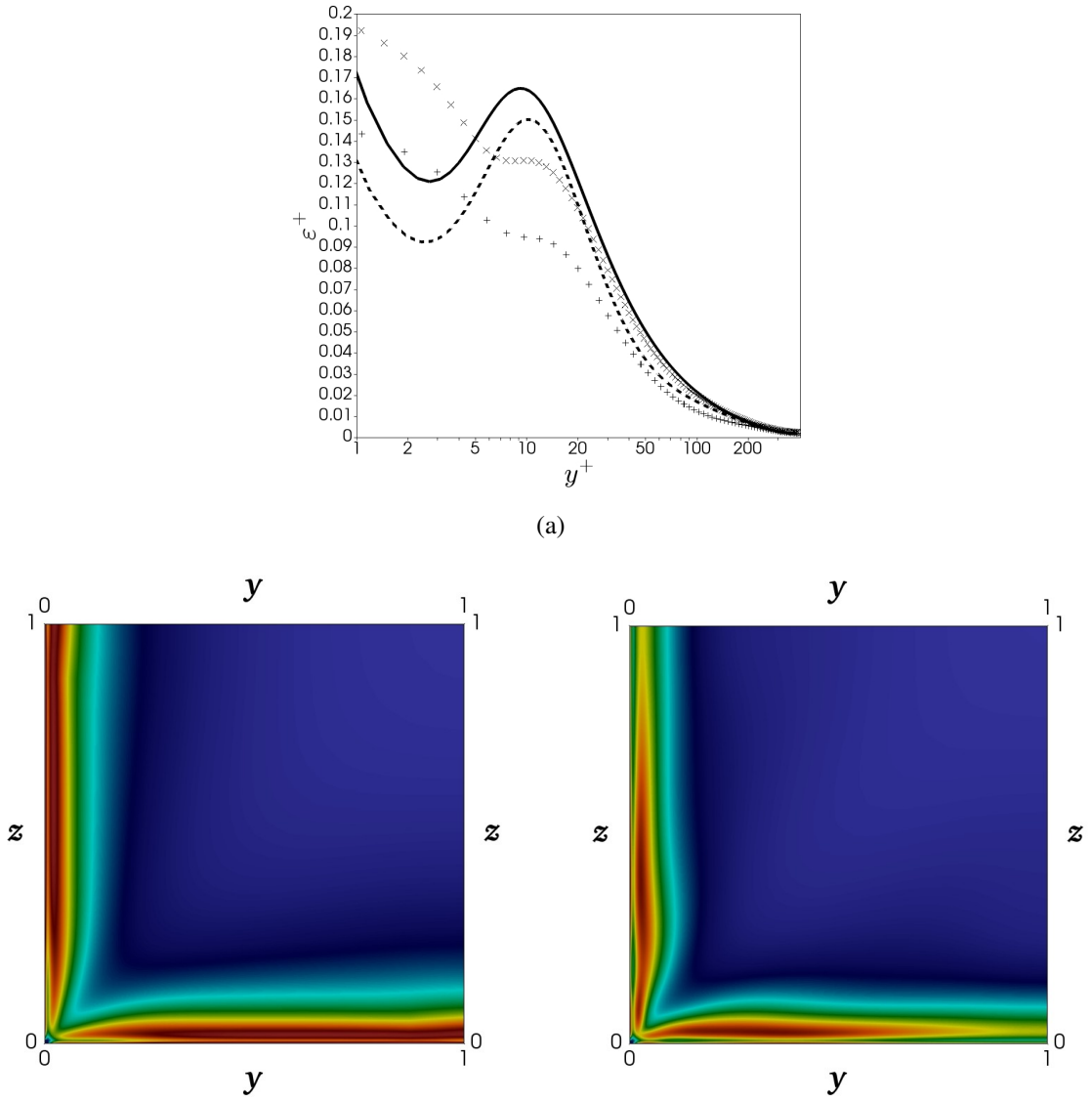

(a)

(b)

(c)

Figure 5.11: Comparison of the ε^+ predictions (solid lines) with DNS data from Newtonian [14] (crosses) and case 'A' (plus) in fully developed channel flow (a), and square duct model predictions (b, c): (b) Newtonian, and (c) LDR. The colour scale ranges from 0 (blue) to 0.2 (red).

5.6.3 Analysis of mean velocity and secondary flow

Figure 5.12 shows model predictions of the mean velocity, U^+, in (a) channel flow, and (b, c) square duct flow. The increase and thickening of the buffer layer is featured for channel flow. This is also translated in square duct flow, with the bending of the isolines towards the square duct corner compared to Newtonian flow. This can be qualitatively assessed in Figure 4a of [75]. Figure 5.13 shows the model predictions of the (a, b) cross stream velocity component, V^+, and (c) streamlines in square duct flow. The increase in V^+ is well captured, which is translated as the shift of the vorticity streamlines away from the duct corner. This can be be qualitatively assessed in Figure 4b of [75]. The

predictions are a consequence of the second normal stress difference, $\overline{w'}^2 - \overline{v'}^2$, closure model for both $\overline{w'}^2$ and $\overline{v'}^2$ addressed separately in previous sections.

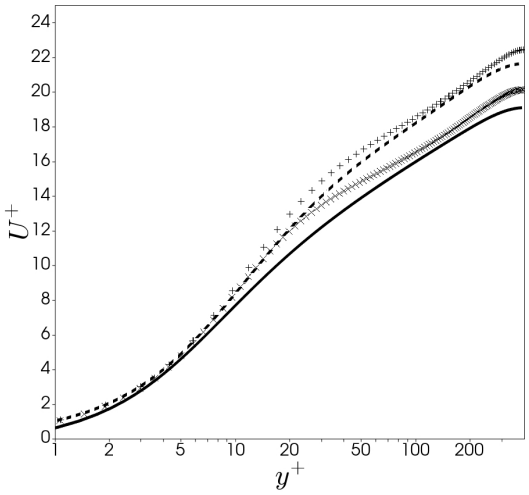

(a)

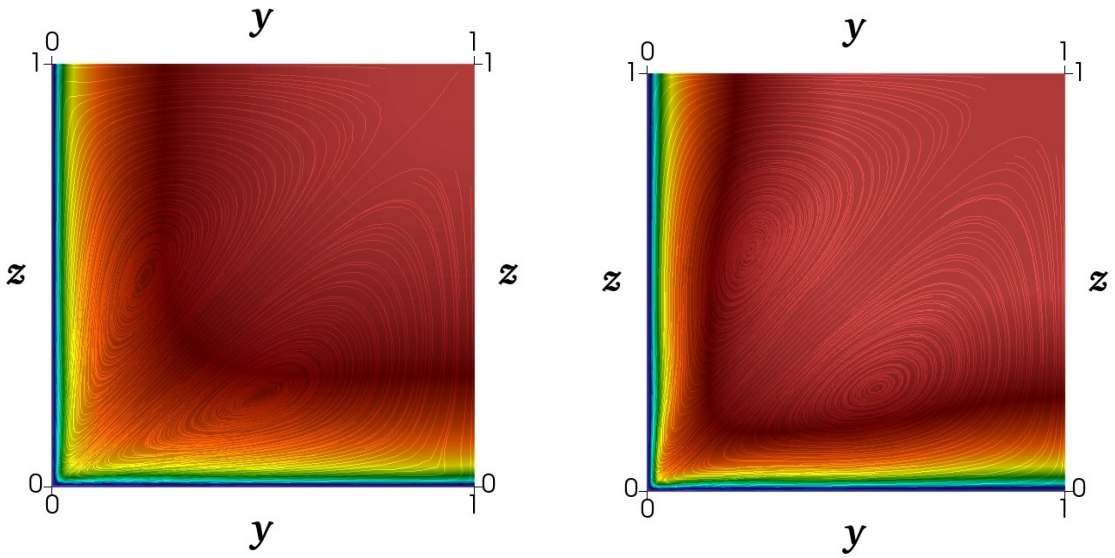

(b) (c)

Figure 5.12: Comparison of the U^+ predictions (lines: solid line, Newtonian; dashed line, case 'A') with DNS data from Newtonian [14] (crosses) and case 'A' (plus) in fully developed channel flow (a), and square duct model predictions (b, c): (b) Newtonian, and (c) LDR. The colour scale ranges from 0 (blue) to 20 (red).

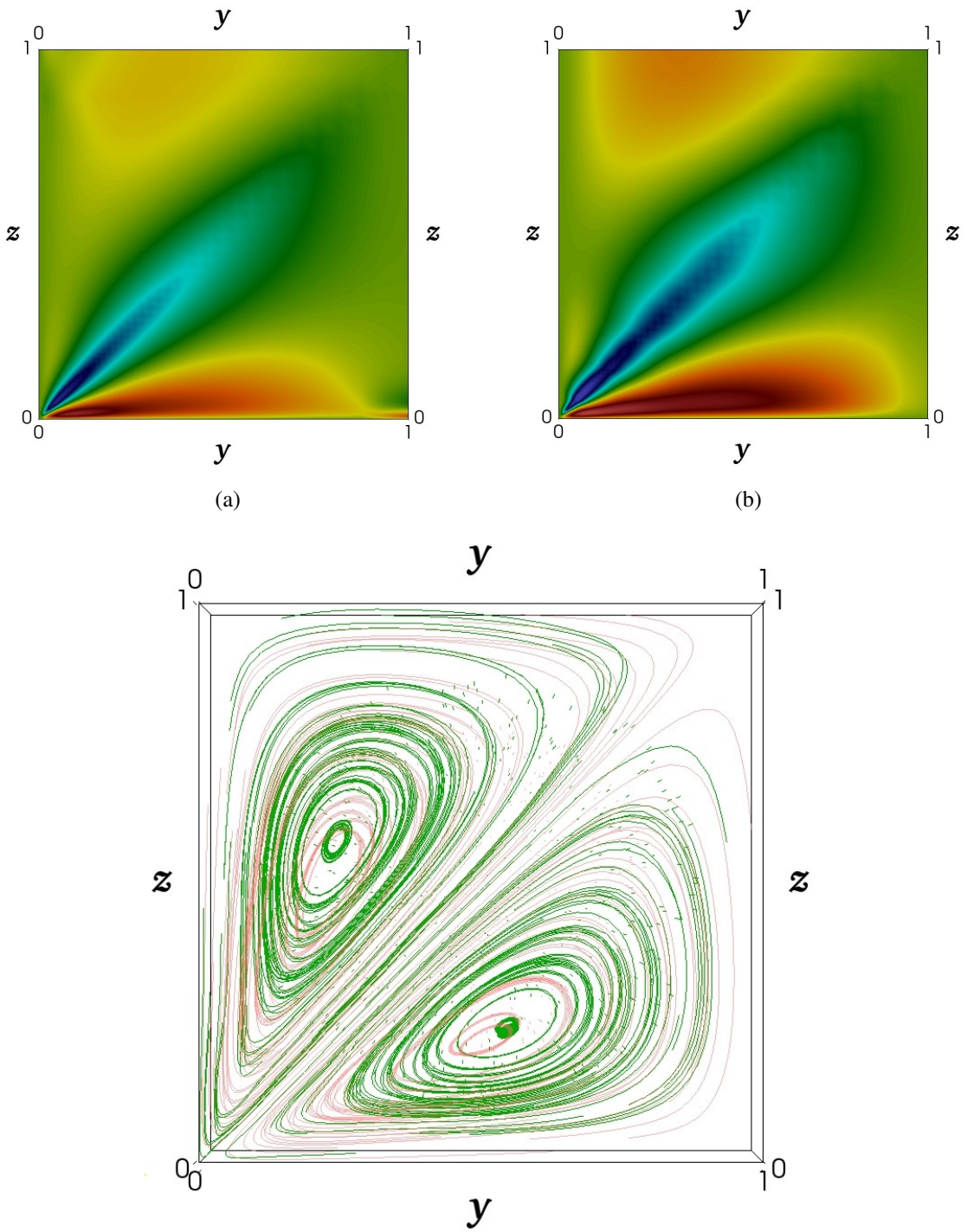

Figure 5.13: Model predictions of (a,b) V^+, and (c) cross streamlines, in square duct flow with the same comparative flow conditions as DNS data from Newtonian [14] and case 'A': (a) Newtonian, (b) LDR, and (c) Newtonian (red) and LDR (green). The colour scale in (a, b) ranges from -0.5 (blue) to 0.5 (red).

5.7 Conclusion

A viscoelastic turbulence model in fully developed channel and square duct flows is proposed, with turbulent eddies modelled under an anisotropic $k-\varepsilon-v^2-f$ representation, along with polymeric solutions described by the finitely extensible nonlinear elastic-Peterlin (FENE-P) constitutive model. The model performance is evaluated against low drag reduction in fully developed channel flow [40] (DR=18% ($Re_{\tau_0}=395$, $Wi_{\tau_0}=25$, $L^2=900$, $\beta=0.9$), and then subsequently qualitatively assessed against square duct flow DNS data [75] with the same rheological parameters.

The model proposes a new closure for the NLT_{ij} term, which redistributes the trace component, NLT_{kk}, to the streamwise and transverse components in a similar manner to the redistribution term found in the normal Reynolds stress model of the Newtonian part [91]. This model shows more robustness than previous models [40, 99, 108] and is the first to give predictions in square ducts. Simple *ad hoc* closures are presented for the spanwise normal Reynolds stress, $\overline{w^2}$, and the turbulent energy redistribution term, f, which are able to calculate the mean flow properties for low drag reduction well.

Overall the model can predict polymer flow features for fully developed channel flow, and is the first model of its kind to predict features in square ducts. This includes the conformation tensor field behaviour, normal Reynolds stress reductions, mean velocity bend of the isolines, along with the shift of the secondary flow vorticity centre away from the wall. The simplicity of the present model allows easy implementation into 3D codes and increased numerical stability for further investigations into more complex geometries.

Chapter 6

Conclusions and future work

This thesis aims to improve the current modelling capabilities and predictions of drag reducing wall bounded turbulent viscoelastic flows, with polymer solutions described by the FENE-P constitutive model, under a RANS description of turbulence. The next sections summarise the contributions made in more detail.

6.1 DNS data, numerical procedure and OpenFOAM

The DNS database was collected from a large source of independent work, containing mean flow data for the whole range of rheological properties and drag reduction regimes. This allowed for *a priori* and *a posteriori* development of closure models for the non-linear terms within the governing equations, along with the validation and testing of the models predictions on mean field values.

Numerical code was developed in OpenFOAM (foam-extend/4.0) as presented in Chapter 2. OpenFOAM was chosen as it allows for the application of future models in more complex geometries, which is open-source and readily available. The key features of the developed numerical code include the adaptation of the pre-existing turbulent class structure, to include the FENE-P parameters within the momentum equation and source files, which can be denoted as an 'effective' turbulent field. The geometry and meshes are developed based on symmetry and mesh independence with 50 wall adjacent cells. The system of equations were solved based on a fixed pressure gradient (*ex post facto*), with the hydraulic radius determined from the geometry, such that the desired friction velocity was set to unity. This enabled easier calculations for the dimensionless field parameters. Each case is uniquely determined from the rheological and flow properties of the corresponding DNS data, namely ν_0, λ, β and L^2 — which are ran in series with sophisticated python and bash scripts for model calibration. The boundary condition for the conformation tensor and dissipation rate is generated using the *groovyBC* functionality within the *swak4foam* functionality, which allows for stable and smooth flow calculations. Relaxation factors, artificial diffusion and finite volumes schemes are included for the additional conformation tensor field, aiding the numerical stability of the simulations. Overall, the numerical procedure is robust and well developed, which enhances the advancement of future turbulent viscoelastic numerical simulations within OpenFOAM.

6.2 Isotropic $k-\varepsilon$ and $k-\omega$ models

In this work, RANS models for FENE-P fluids were improved by removing friction velocity dependence and reducing complexity from the current literature [70]. This is presented with published work in Chapter 3 [99] and Chapter 4 [108]. The defining features of the work are the simplified NLT_{ij} component, and the modified damping function, f_μ. The NLT_{ij} shows more robustness and stability in predicting a wider range of friction Reynolds

numbers and rheological properties. The goal of the damping function was to mimic the viscoelastic effects on the turbulent redistribution process, via a reduction in the eddy viscosity as it is shifted away from the buffer layer. The $k-\varepsilon$ model is capable of predicting a large range of flow features for low and high Reynolds number at all regimes of DR and improves significantly on the model of Resende et al. [70], with its ability to capture higher Reynolds numbers with simpler closures.

Further improvements were made with the development of the $k-\omega$ model. This includes the addition of concentration variation, β, and spans a larger DNS data set than the $k-\varepsilon$ model. The damping function was demonstrated to have robustness with a valid sensitivity study, along with the $k-\omega$ model naturally having more numerical stability.

Both models capture well the turbulent kinetic energy redistribution, as it shifts away from the wall and thickens in the buffer layer. These predictions improve on the $k-\varepsilon-v^2-f$ and Reynolds stress models [40, 69] previously developed, where for HDR, these trends are reversed in these models. This is due to the damping function capabilities in reducing the near wall eddy activities. Although the two models can capture features well in fully developed channel flow, expanding them to more general flows is challenging as a result of some of the *ad hoc* terms developed. More analysis in complex flows (backward facing step, constricting flows,...) is required to investigate the applicability of modified damping functions.

6.3 Anisotropic $k-\varepsilon-v^2-f$ model

The anisotropic $k-\varepsilon-v^2-f$ model (Chapter 5) is the first model to predict polymer flow features in multiple canonical geometries, fully developed channel and square ducts — which expands upon the Newtonian anisotropic model of Pecnik and Iaccarino [91]. The key feature is the developed NLT_{ij} component, which redistributes the trace component, NLT_{kk}, to the streamwise and transverse components in a similar fashion to the normal Reynolds stress term in the Newtonian model. This was inspired by the fact that polymers tend to align themselves with the mean normal Reynolds stress direction or mean vorticity direction (denoted t_i), along with *a priori* DNS analysis of the distribution of normal Reynolds stresses compared to the NLT_{ij} term. This improves upon the previous attempts to form a Boussinesq-like NLT_{ij} term [40], where now the proportionality is made with the correct transverse component and not the shear term. The model also removes friction velocity dependence and additional damping functions as found in the Reynolds stress model NLT_{ij} term [69].

The predictions for the model include fully developed channel flow and square ducts in LDR, with flow features in the conformation tensor, Reynolds stresses, mean velocity (and the bending of the isolines), along with the shift of the secondary flow vorticity centre away from the wall. The model shows great potential for wall bounded turbulent polymer flow, with robustness in the modelled terms, and ability to capture the physics

and key dynamics adequately. The simplicity of the present model allows easy implementation into 3D codes and increased numerical stability for further investigations into more complex geometries.

6.4 Future work

The use of OpenFOAM in this thesis was chosen as it is open-source and readily available. Although the developed code shows great potential, there is yet to be a fully integrated turbulent viscoelastic class structure from the OpenFOAM team. There does exist a laminar viscoelastic tool kit with *Rheotool*, and it would be advantageous for the community to integrate these feature with turbulence.

The ability to capture important flow features for the developed anisotropic $k-\varepsilon-v^2-f$ model for square ducts can potentially be expanded more generally for regular polygons. Results for a triangular (equilateral) duct at $Re_{\tau_0}=395$ for DR=0% and DR=18% (LDR) can be viewed in Figures 6.1 and 6.2. The same polymer flow features are observed as in the square duct. Although DNS data in turbulent viscoelastic flow for other non-circular ducts (triangle, hexagon...) have not been performed, it is a fair assumption that the same features will occur in these systems.

An alternative Newtonian model to Chapter 5 can be the use of the $k-\varepsilon-\phi-f$ model by Laurence et al. [115], where $\phi=v^2/k$ is used as a more natural scaling. The Newtonian model is already built into the OpenFOAM turbulence class structure, meaning the development of the turbulent viscoelastic model would have more ease of access. The potential model skeleton can be viewed in the Appendix. Although this model is untested in the current work, it allows for the potential of more robust and stable calculations in the same fashion as the $k-\omega$ counterparts.

In the current literature, more attention is needed for features such as heat exchange and mechanical degradation (scission in real polymers). Heat exchange is uniquely captured with a simple linear model [40], although these features must be investigated in more complex geometries. With regards to mechanical degradation, a more recent study [116] attempts to model the maximum polymer extension with temporal and spatial variations, $L(x,y,z,t)$. The numerical simulations are unstable as a result of the varying L, meaning adequate results are difficult to obtain.

Overall, the advancement of more sophisticated models within open-source 3D codes that can capture a range of turbulent polymer flow features is highly advantageous for industry and academic personnel.

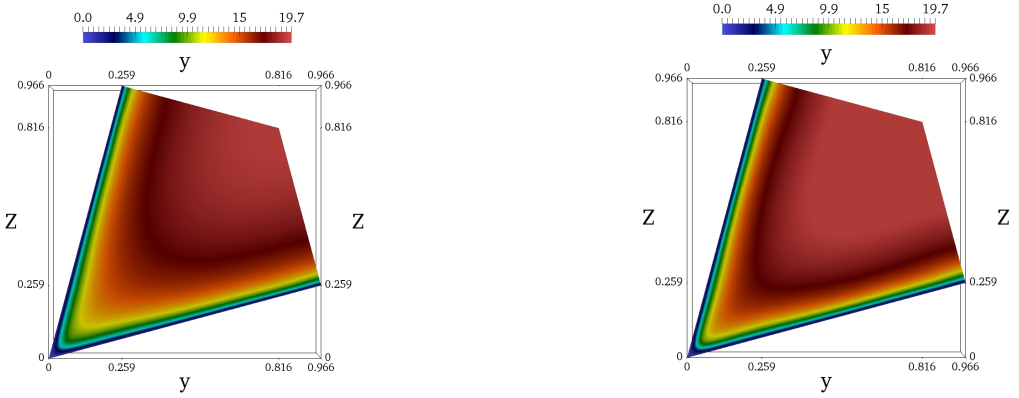

(a) U^{+}_{Newt}

(b) U^{+}_{LDR}

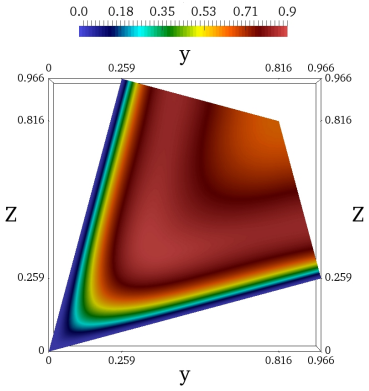

(c) v^{2+}_{Newt}

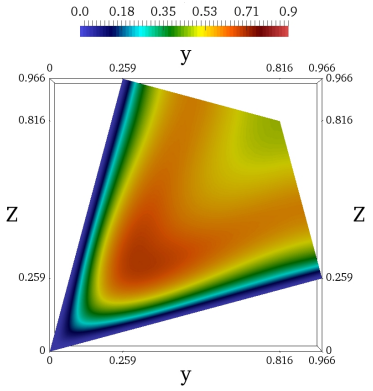

(d) v^{2+}_{Vis}

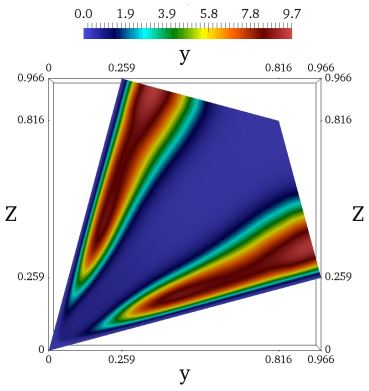

(e) NLT^{+}_{kk}

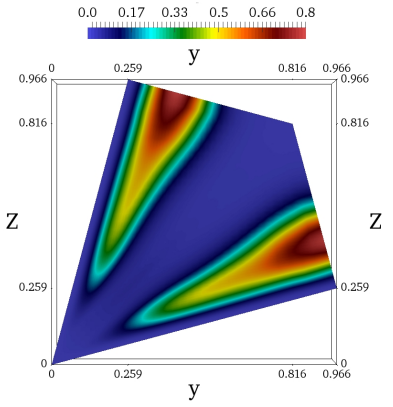

(f) $NLT^{+}_{v^2}$

Figure 6.1: Model predictions of fully developed triangular (equilateral) duct flow at $Re_{\tau_0} = 395$ for $DR = 0\%$ (Newtonian) and $DR = 18\%$ (LDR). (a, b) mean velocity, U^{+}; (c, d) wall normal Reynolds stress, v^{2+}; (e, f) NLT^{+}_{ij} components.

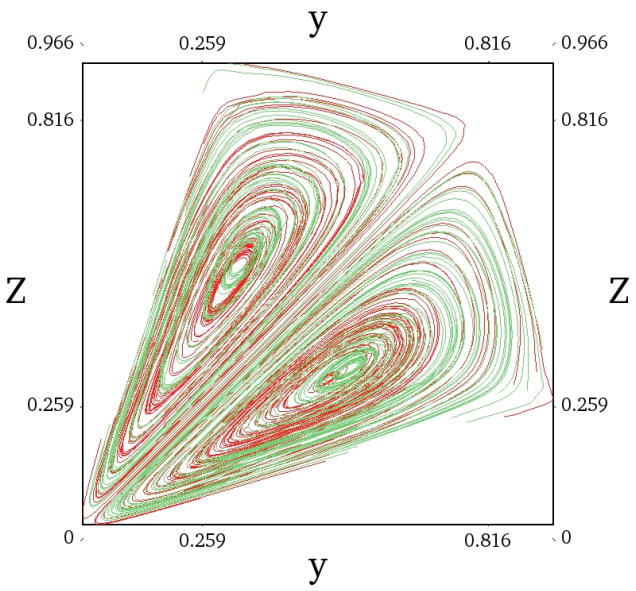

Figure 6.2: Model predictions of cross streamlines in fully developed triangular (equilateral) duct flow at $Re_{\tau_0} = 395$: Newtonian (red) and LDR (green).

Appendix

RANS FENE-P $k-\varepsilon-\phi-f$ model

Presented here are the governing equations for an untested $k-\varepsilon-\phi-f$ model, applicable in non-circular ducts for turbulent polymer flow.

Momentum equation:

$$U_j\frac{\partial U_i}{\partial x_j} = -\frac{\partial \overline{p}}{\partial x_i} + \frac{\partial}{\partial x_j}\left((\beta\nu_0+\nu_T)\frac{\partial U_i}{\partial x_j} - kN_{ij}\right) + \frac{(1-\beta)\nu_0}{\lambda}\frac{\partial}{\partial x_j}\left(f(C_{mm})C_{ij}-\delta_{ij}\right), \tag{6.1}$$

where the eddy viscosity is

$$\nu_T = C_\mu \phi k T_t, \tag{6.2}$$

the normal Reynolds stress distribution term is

$$N_{ij} = \frac{2}{3}\delta_{ij} + \left(1-\frac{3}{2}\phi\right)\left(\frac{\delta_{ij}}{3}-n_in_j\right) + \left(\frac{2-f_d}{2+f_d}-\frac{1}{2}\phi\right)(2t_it_j+n_in_j-\delta_{ij}), \tag{6.3}$$

with

$$f_d = \min\left[\max\left(\left(\frac{3}{2}\phi\right)^{1/2}, \frac{0.3}{1+(L/30)^2}\right), 1.0\right]. \tag{6.4}$$

The wall normal vector, n_i, and the normalised direction of mean vorticity, t_i, are given by Eqs. (5.10) and (5.12), respectively.

Conformation tensor transport equation:

$$\frac{DC_{ij}}{Dt} - M_{ij} - NLT_{ij} = -\frac{1}{\lambda}[f(C_{kk})C_{ij}-\delta_{ij}], \tag{6.5}$$

with

$$NLT_{ij} = C_{N1}f_N M_{kk}\left(t_it_j + C_{N2}\phi n_in_j\right), \tag{6.6}$$

where $f_N = \nu_T/\nu_0$ is the local eddy viscosity.

Turbulent kinetic energy transport equation:

$$U_j \frac{\partial k}{\partial x_j} = \frac{\partial}{\partial x_j}\left[\left(\beta \nu_0 + \frac{\nu_\mathrm{T}}{\sigma_k}\right)\frac{\partial k}{\partial x_j}\right] + \left(P_k - \varepsilon^V\right) - \varepsilon, \tag{6.7}$$

where $P_k = \overline{u_i' u_j'} S_{ij}$ and

$$\varepsilon^V \equiv \varepsilon^V_{kk} = \frac{\nu_\mathrm{p}}{2\lambda} f(C_{mm}) NLT_{kk}. \tag{6.8}$$

Dissipation transport equation:

$$U_j \frac{\partial \varepsilon}{\partial x_j} = \frac{\partial}{\partial x_j}\left[\left(\beta \nu_0 + \frac{\nu_\mathrm{T}}{\sigma_\varepsilon}\right)\frac{\partial \varepsilon}{\partial x_j}\right] + \frac{C_{\varepsilon 1}(P_k - \varepsilon^V) - C_{\varepsilon 2}\varepsilon}{T_t} \tag{6.9}$$

Normalised wall-normal fluctuating velocity scale transport equation:

$$U_j \frac{\partial \phi}{\partial x_j} = \frac{\partial}{\partial x_j}\left[\left(\beta \nu_0 + \frac{\nu_\mathrm{T}}{\sigma_k}\right)\frac{\partial \phi}{\partial x_j}\right] + f - \frac{\phi}{k} P_k \tag{6.10}$$

Elliptic relaxation, f, transport equation

$$L_t^2 \frac{\partial^2 f}{\partial x_j \partial x_j} - f = \frac{1}{T_t}\left(C_1 - 1 + C_2' \frac{P_k}{\varepsilon}\right)\left(\phi - \frac{2}{3}\right). \tag{6.11}$$

DNS data visuals in square ducts

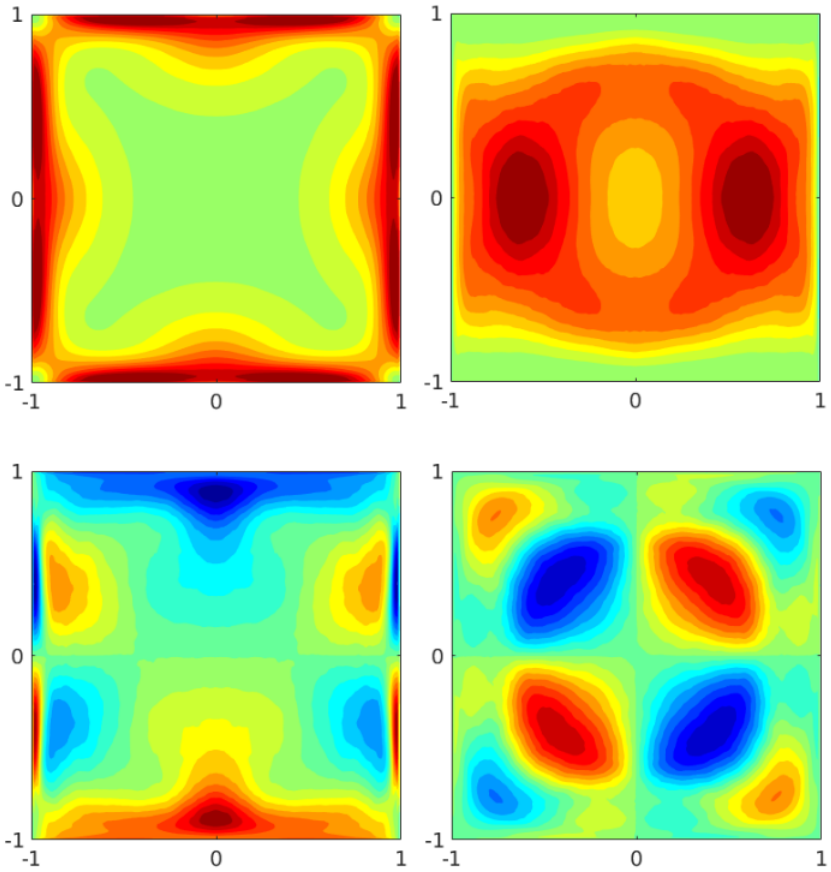

FIGURE 8. Contours of four components of the conformation tensor C_{ij}: (top left) C_{11}, (top right) C_{22}, (bottom left) C_{12}, and (bottom right) C_{23}. Color scales range from 30 (green) to 800 (red), from 5 (blue) to 50 (red), from -30 (blue) to 30 (red), and from -10 (blue) to 10 (red), respectively.

Figure 6.3: Mean confirmation tensor DNS data for ($DR = 27\%, Re_{\tau_0} = 180$, $L^2 = 3600$, $Wi_{\tau_0} = 18$) [75]

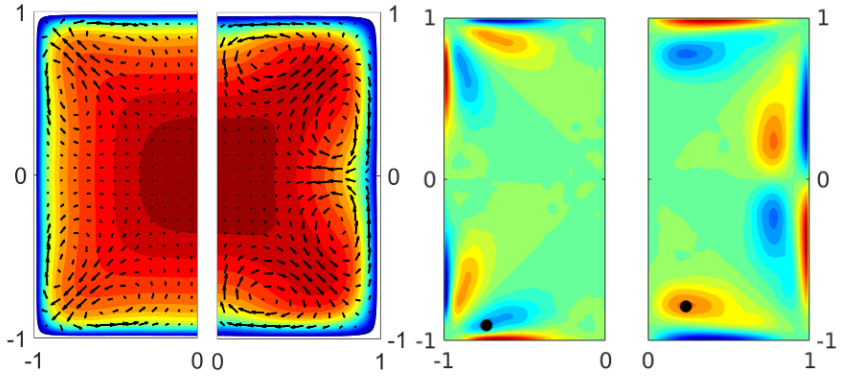

FIGURE 4. Contour of the mean streamwise component of (left) velocity $\overline{u}$ and (right) vorticity $\overline{\omega}_x$. In each figure, the left and right half of the duct are used for the Newtonian and viscoelastic fluids, respectively. The color scale ranges from 0 (blue) to $1.4U_b$ (red) in the left panel and from $-0.5U_b/h$ (blue) to $0.5U_b/h$ (red) in the right one. The two left panels also report the in-plane mean velocity with arrows.

Figure 6.4: Mean velocity and vorticity DNS data for ($DR = 27\%, Re_{\tau_0} = 180$, $L^2 = 3600$, $Wi_{\tau_0} = 18$) [75]

Bibliography

[1] G. Settles. Laminar-turbulent transition: This schlieren photograph shows the thermal convection plume rising from an ordinary candle in still air. https://commons.wikimedia.org/wiki/file:laminar-turbulent-transition.jpg, 2007. 3

[2] T. W. Berger, J. Kim, C. Lee, and J. Lim. Turbulent boundary layer control utilising the Lorentz force. *Physics of Fluids*, 12(3):631–649, 2000. 3

[3] T. Segawa, H. Mizunuma, K. Murakami, F. C. Li, and H. Yoshida. Turbulent drag reduction by means of alternating suction and blowing jets. *Fluid Dynamics Research*, 39(7):552, 2007. 3

[4] Y. Du, V. Symeonidis, and G. E. Karniadakis. Drag reduction in wall-bounded turbulence via a transverse travelling wave. *Journal of Fluid Mechanics*, 457:1, 2002. 3

[5] Y. Mito and N. Kasagi. DNS study of turbulence modification with streamwise-uniform sinusoidal wall-oscillation. *International Journal of Heat and Fluid Flow*, 19(5):470–481, 1998. 3

[6] M. Quadrio, P. Ricco, and C. Viotti. Streamwise-travelling waves of spanwise wall velocity for turbulent drag reduction. *Journal of Fluid Mechanics*, 627:161–178, 2009. 3

[7] F. C. Li, B. Yu, J. J. Wei, and Y. Kawaguchi. *Turbulent drag reduction by surfactant additives*. John Wiley & Sons, 2012. 3

[8] J. J. J. Gillissen, B. J. Boersma, P. H. Mortensen, and H. I. Andersson. Fibre-induced drag reduction. *Journal of Fluid Mechanics*, 602:209, 2008. 3

[9] L. Xi. Turbulent drag reduction by polymer additives: Fundamentals and recent advances. *Physics of Fluids*, 31(12):121302, 2019. 3, 6, 28, 99

[10] B. A. Toms. Some observations on the flow of linear polymer solutions through straight tubes at large Reynolds numbers. *Proceedings of the International Congress on Rheology, 1948*, 135, 1948. 3, 15

[11] A. Gyr and H. W. Bewersdorff. *Drag reduction of turbulent flows by additives*, volume 32. Springer Science & Business Media, 2013. 3

[12] J. F. Motier and D. J. Prilutski. Case histories of polymer drag reduction in crude-oil lines. *Pipe Line Industry*, 62(6):33, 1985. 3

[13] H. K. Versteeg and W. Malalasekera. *An introduction to computational fluid dynamics: the finite volume method*. Pearson Education, 2007. 5, 8, 29

[14] R. D. Moser, J. Kim, and N. N. Mansour. Direct numerical simulation of turbulent channel flow up to $Re_\tau = 590$. *Physics of Fluids*, 11(4):943–945, 1999. xv, 6, 62, 68, 73, 75, 85, 86, 93, 94, 102, 103, 104, 105, 106

[15] C. F. Li, V. K. Gupta, R. Sureshkumar, and B. Khomami. Turbulent channel flow of dilute polymeric solutions: Drag reduction scaling and an eddy viscosity model. *Journal of Non-Newtonian Fluid Mechanics*, 139(3):177–189, 2006. 6, 13, 14, 18, 43, 49

[16] M. Masoudian, K. Kim, F. T. Pinho, and R. Sureshkumar. A viscoelastic $k-\varepsilon-v^2-f$ turbulent flow model valid up to the maximum drag reduction limit. *Journal of Non-Newtonian Fluid Mechanics*, 202:99–111, 2013. 6, 14, 18, 19, 27, 28, 37, 38, 39, 40, 41, 43, 44, 45, 46, 50, 52, 62, 63, 65, 69, 81, 83, 88, 90, 94, 95, 99, 102

[17] J. Smagorinsky. General circulation experiments with the primitive equations: I. The basic experiment. *Monthly Weather Review*, 91(3):99–164, 1963. 6

[18] J. W. Deardorff. A numerical study of three-dimensional turbulent channel flow at large Reynolds numbers. *Journal of Fluid Mechanics*, 41(2):453–480, 1970. 6

[19] A. C. Mósca, C. B. da Silva, F. T. Pinho, and P. C. Valente. Relevant terms for large-eddy simulations of viscoelastic isotropic turbulence. *14th European Turbulence Conference*, 2013. 7

[20] L. Thais, A. E. Tejada-Martinez, T. B. Gatski, and G. Mompean. Temporal large eddy simulations of turbulent viscoelastic drag reduction flows. *Physics of Fluids*, 22(1):013103, 2010. 7, 41

[21] L. Feng-Chen, W. Lu, and C. Wei-Hua. New subgrid-scale model based on coherent structures and temporal approximate deconvolution, particularly for LES of turbulent drag-reducing flows of viscoelastic fluids. *China Physics B*, 2015. 7

[22] J. Li, B. Yu, L. Wang, F. Li, and L. Hou. A mixed subgrid-scale model based on ICSM and TADM for LES of surfactant-induced drag-reduction in turbulent channel flow. *Applied Thermal Engineering*, 115:1322–1329, 2017. 7

[23] J. Li, B. Yu, X. Zhang, S. Sun, D. Sun, and T. Zhang. LES study on high Reynolds turbulent drag-reducing flow of viscoelastic fluids based on multiple relaxation times constitutive model and mixed subgrid-scale model. In *International Conference on Computational Science*, pages 174–188. Springer, 2018. 7

[24] W D. McComb. The physics of fluid turbulence. *Chemical Physics*, 1990. 8

[25] F. S. Lien and P. A. Durbin. Non-linear $k-\varepsilon-v^2-f$ modelling with application to high-lift. *Summer Program Centre for Turbulence Research, Stanford*, pages 5–22, 1996. 9

[26] Y. Roiter and S. Minko. AFM single molecule experiments at the solid-liquid interface: in situ conformation of adsorbed flexible polyelectrolyte chains. *Journal of the American Chemical Society*, 127(45):15688–15689, 2005. 10

[27] A. Yethiraj and C. K. Hall. Monte-Carlo simulation of polymers confined between flat plates. *Macromolecules*, 23(6):1865–1872, 1990. 11

[28] N. Rathore and J. J. de Pablo. Monte-Carlo simulation of proteins through a random walk in energy space. *The Journal of Chemical Physics*, 116(16):7225–7230, 2002. 11

[29] R. B. Bird, R. C. Armstrong, and O. Hassager. *Dynamics of polymeric liquids. Vol. 1: Fluid mechanics*. John Wiley and Sons, 1987. 11, 12, 17

[30] R. B. Bird and H. C. Ottinger. Transport properties of polymeric liquids. *Annual Review of Physical Chemistry*, 43(1):371–406, 1992. 11

[31] R. Keunings. On the Peterlin approximation for finitely extensible dumbbells. *Journal of Non-Newtonian Fluid Mechanics*, 68(1):85–100, 1997. 11

[32] C. M. White and M. G. Mungal. Mechanics and prediction of turbulent drag reduction with polymer additives. *Annual Review of Fluid Mechanics*, 40:235–256, 2008. 12, 15, 17

[33] G. Lielens, R. Keunings, and V. Legat. The FENE-L and FENE-LS closure approximations to the kinetic theory of finitely extensible dumbbells. *Journal of Non-Newtonian Fluid Mechanics*, 87(2-3):179–196, 1999. 12

[34] P. R. Resende. *Turbulence models for viscoelastic fluids*. PhD thesis, Universidade do Porto (Portugal), 2010. 13

[35] Q. Zhou and R. Akhavan. A comparison of FENE and FENE-P dumbbell and chain models in turbulent flow. *Journal of Non-Newtonian Fluid Mechanics*, 109(2-3):115–155, 2003. 13

[36] R. Sureshkumar, A. N. Beris, and R. A. Handler. Direct numerical simulation of the turbulent channel flow of a polymer solution. *Physics of Fluids*, 9(3):743–755, 1997. 13, 17, 18, 27, 48

[37] K. D. Housiadas, A. N. Beris, and R. A. Handler. Viscoelastic effects on higher order statistics and on coherent structures in turbulent channel flow. *Physics of Fluids*, 17(3):035106, 2005. 13, 14, 18

[38] F. T. Pinho, C. F. Li, B. A. Younis, and R. Sureshkumar. A low reynolds number turbulence closure for viscoelastic fluids. *Journal of Non-Newtonian Fluid Mechanics*, 154(2-3):89–108, 2008. 14, 18, 19, 25, 27, 37, 39, 41, 43, 45, 61, 64, 65, 86, 88, 94

[39] G. Iaccarino, E. S. G. Shaqfeh, and Y. Dubief. Reynolds-averaged modelling of polymer drag reduction in turbulent flows. *Journal of Non-Newtonian Fluid Mechanics*, 165(7-8):376–384, 2010. 14, 19, 30, 38, 39, 41, 43, 62, 63, 64, 67, 90, 95

[40] M. Masoudian, F. T. Pinho, K. Kim, and R. Sureshkumar. A RANS model for heat transfer reduction in viscoelastic turbulent flow. *International Journal of Heat and Mass Transfer*, 100:332–346, 2016. 19, 27, 38, 39, 40, 41, 44, 45, 46, 48, 62, 63, 65, 69, 85, 86, 88, 90, 94, 95, 96, 100, 102, 107, 110, 111

[41] P. R. Resende, F. T. Pinho, B. A. Younis, K. Kim, and R. Sureshkumar. Development of a low-Reynolds-number $k-\omega$ model for FENE-P fluids. *Flow, Turbulence and Combustion*, 90(1):69–94, 2013. 14, 18, 56, 58, 60, 61, 65, 69, 73, 78

[42] P. S. Virk. Drag reduction fundamentals. *AIChE Journal*, 21(4):625–656, 1975. 15

[43] A. Abubakar, T. Al-Wahaibi, Y. Al-Wahaibi, A. R. Al-Hashmi, and A. Al-Ajmi. Roles of drag reducing polymers in single-and multi-phase flows. *Chemical Engineering Research and Design*, 92(11):2153–2181, 2014. 16

[44] J. G. Oldroyd. A suggested method of detecting wall-effects in turbulent flow through tubes. *International Congress on Rheology*, 2:130, 1948. 16

[45] J. L. Lumley. Drag reduction by additives. *Annual Review of Fluid Mechanics*, 1(1):367–384, 1969. 16, 17

[46] E. J. Hinch. Mechanical models of dilute polymer solutions in strong flows. *Physics of Fluids*, 20(10):S22–S30, 1977. 16

[47] G. Ryskin. Turbulent drag reduction by polymers: a quantitative theory. *Physical Review Letters*, 59(18):2059, 1987. 16

[48] P. S. Virk. An elastic sublayer model for drag reduction by dilute solutions of linear macromolecules. *Journal of Fluid Mechanics*, 45(3):417–440, 1971. 16

[49] M. Tabor and P. G. De Gennes. A cascade theory of drag reduction. *Euro-Physics Letters*, 2(7):519, 1986. 16

[50] V. N. Kalashnikov. Shear-rate dependent viscosity of dilute polymer solutions. *Journal of Rheology*, 38(5):1385–1403, 1994. 16

[51] V. S. L'vov, A. Pomyalov, I. Procaccia, and V. Tiberkevich. Drag reduction by polymers in wall bounded turbulence. *Physical Review Letters*, 92(24):244503, 2004. 17

[52] T. Min, J. Y. Yoo, H. Choi, and D. D. Joseph. Drag reduction by polymer additives in a turbulent channel flow. *Journal of Fluid Mechanics*, 486:213–238, 2003.

[53] V. Dallas, J. C. Vassilicos, and G. F. Hewitt. Strong polymer-turbulence interactions in viscoelastic turbulent channel flow. *Physical Review E*, 82(6):066303, 2010.

[54] L. Thais, T. B. Gatski, and G. Mompean. Analysis of polymer drag reduction mechanisms from energy budgets. *International Journal of Heat and Fluid Flow*, 43:52–61, 2013. 18, 38, 39

[55] Y. Dubief, V. E. Terrapon, C. M. White, E. S. G. Shaqfeh, P. Moin, and S. K. Lele. New answers on the interaction between polymers and vortices in turbulent flows. *Flow, Turbulence and Combustion*, 74(4):311–329, 2005. 17, 19

[56] K. Kim, C. F. Li, R. Sureshkumar, S. Balachandar, and R. J. Adrian. Effects of polymer stresses on eddy structures in drag-reduced turbulent channel flow. *Journal of Fluid Mechanics*, 584:281–299, 2007. 17, 27, 85, 86, 87, 94

[57] P. K. Ptasinski, B. J. Boersma, F. T. M. Nieuwstadt, M. A. Hulsen, B. H. A. A. Van den Brule, and J. C. R. Hunt. Turbulent channel flow near maximum drag reduction: simulations, experiments and mechanisms. *Journal of Fluid Mechanics*, 490:251–291, 2003. 17, 18, 62, 63, 102

[58] R. B. Bird, P. J. Dotson, and N. L. Johnson. Polymer solution rheology based on a finitely extensible bead—spring chain model. *Journal of Non-Newtonian Fluid Mechanics*, 7(2-3):213–235, 1980. 17

[59] C. D. Dimitropoulos, R. Sureshkumar, A. N. Beris, and R. A. Handler. Budgets of Reynolds stress, kinetic energy and streamwise enstrophy in viscoelastic turbulent channel flow. *Physics of Fluids*, 13(4):1016–1027, 2001. 17, 21, 87, 90

[60] Y. Dubief, G. Laccarino, and S. K. Lele. A turbulence model for polymer flows. *Center for Turbulence Research, Stanford*, 2004. 17, 19, 40, 67, 88

[61] C. F. Li, R. Sureshkumar, and B. Khomami. Influence of rheological parameters on polymer induced turbulent drag reduction. *Journal of Non-Newtonian Fluid Mechanics*, 140(1-3):23–40, 2006. 18, 27, 38, 39, 43, 62, 63, 67, 71, 87, 89

[62] F. T. Pinho. A GNF framework for turbulent flow models of drag reducing fluids and proposal for a $k-\varepsilon$ type closure. *Journal of Non-Newtonian Fluid Mechanics*, 114(2-3):149–184, 2003. 18, 20, 43

[63] D. O. A. Cruz and F. T. Pinho. Turbulent pipe flow predictions with a low Reynolds number $k-\varepsilon$ model for drag reducing fluids. *Journal of Non-Newtonian Fluid Mechanics*, 114(2-3):109–148, 2003. 18

[64] D. O. A. Cruz, F. T. Pinho, and P. R. Resende. Modelling the new stress for improved drag reduction predictions of viscoelastic pipe flow. *Journal of Non-Newtonian Fluid Mechanics*, 121(2-3):127–141, 2004. 18, 43

[65] P. R. Resende, M. P. Escudier, F. Presti, F. T. Pinho, and D. O. A. Cruz. Numerical predictions and measurements of Reynolds normal stresses in turbulent pipe flow of polymers. *International Journal of Heat and Fluid Flow*, 27(2):204–219, 2006. 18, 43

[66] P. R. Resende, F. T. Pinho, and D. O. Cruz. A Reynolds stress model for turbulent flows of viscoelastic fluids. *Journal of Turbulence*, 14(12):1–36, 2013. 18

[67] R. Leighton, D. T. Walker, T. Stephens, and G. Garwood. Reynolds stress modelling for drag reducing viscoelastic flows. In *4th Joint Fluids Summer Engineering Conference*, pages 735–744. American Society of Mechanical Engineers, 2003. 18, 19, 67, 84, 90, 95

[68] P. R. Resende, K. Kim, B. A. Younis, R. Sureshkumar, and F. T. Pinho. A FENE-P $k-\varepsilon$ turbulence model for low and intermediate regimes of polymer-induced drag reduction. *Journal of Non-Newtonian Fluid Mechanics*, 166(12-13):639–660, 2011. 18, 19, 27, 37, 39, 43, 45, 46, 69, 73, 78, 95

[69] M. Masoudian, K. Kim, F. T. Pinho, and R. Sureshkumar. A Reynolds stress model for turbulent flow of homogeneous polymer solutions. *International Journal of Heat and Fluid Flow*, 54:220–235, 2015. 19, 40, 64, 89, 94, 110

[70] P. R. Resende, A. M. Afonso, and D. O. Cruz. An improved $k-\varepsilon$ turbulence model for FENE-P fluids capable to reach high drag reduction regime. *International Journal of Heat and Fluid Flow*, 73:30–41, 2018. xii, 19, 27, 35, 39, 40, 41, 42, 43, 44, 45, 46, 47, 49, 51, 52, 55, 56, 58, 64, 65, 67, 69, 73, 78, 83, 90, 94, 109, 110

[71] P. R. Resende, F. T. Pinho, and P. J. Oliveira. Improvement of the energy distribution in isotropic turbulent viscoelastic fluid models. *MEFTE*, page 221, 2014. 19

[72] P. R. Resende and A. S. Cavadas. New developments in isotropic turbulent models for FENE-P fluids. *Fluid Dynamics Research*, 50(2):025508, 2018. 19, 43

[73] T. Tsukahara and Y. Kawaguchi. Proposal of damping function for low-Reynolds number model applicable in prediction of turbulent viscoelastic-fluid flow. *Journal of Applied Mathematics*, 2013, 2013. 20, 43

[74] M. C. Guimarães, N. Pimentel, F. T. Pinho, and C. B. da Silva. Direct numerical simulations of turbulent viscoelastic jets. *Journal of Fluid Mechanics*, 899:A11, 2020. 20

[75] A. Shahmardi, S. Zade, M. N. Ardekani, R. J. Poole, F. Lundell, M. E. Rosti, and L. Brandt. Turbulent duct flow with polymers. *Journal of Fluid Mechanics*, 859:1057–1083, 2019. xvi, 20, 21, 81, 85, 86, 100, 104, 107, 116

[76] R. J. Poole and MP Escudier. Turbulent flow of non-newtonian liquids over a backward-facing step: Part i. a thixotropic and shear-thinning liquid. *Journal of Non-Newtonian Fluid Mechanics*, 109(2-3):177–191, 2003. 20

[77] RJ Poole and MP Escudier. Turbulent flow of non-newtonian liquids over a backward-facing step: Part ii. viscoelastic and shear-thinning liquids. *Journal of Non-Newtonian Fluid Mechanics*, 109(2-3):193–230, 2003. 20

[78] L. Prandtl. Turbulent flow. *National Advisory Committee for Aeronautics*, 1927. 20

[79] L. C. Hoagland. *Fully developed turbulent flow in straight rectangular ducts: secondary flow, its cause and effect on the primary flow*. PhD thesis, Massachusetts Institute of Technology, 1962. 20

[80] J. Nikuradse. Untersuchungen über turbulente strömungen in nicht kreisförmigen rohren. *Ingenieur-Archiv*, 1(3):306–332, 1930. 20

[81] H. J. Leutheusser. Turbulent flow in rectangular ducts. *Journal of the Hydraulics Division*, 89(3):1–19, 1963. 20

[82] E. Brundrett and W. D. Baines. The production and diffusion of vorticity in duct flow. *Journal of Fluid Mechanics*, 19(3):375–394, 1964. 20

[83] F. B. Gessner and J. B. Jones. On some aspects of fully-developed turbulent flow in rectangular channels. *Journal of Fluid Mechanics*, 23(4):689–713, 1965. 20

[84] B. E. Launder and W. M. Ying. Secondary flows in ducts of square cross-section. *Journal of Fluid Mechanics*, 54(2):289–295, 1972. 20

[85] M. J. Rudd. Velocity measurements made with a laser dopplermeter on the turbulent pipe flow of a dilute polymer solution. *Journal of Fluid Mechanics*, 51(4):673–685, 1972. 21

[86] M. P. Escudier, A. K. Nickson, and R. J. Poole. Turbulent flow of viscoelastic shear-thinning liquids through a rectangular duct: Quantification of turbulence anisotropy. *Journal of Non-Newtonian Fluid Mechanics*, 160(1):2–10, 2009. 21

[87] C. G. Speziale. On turbulent secondary flows in pipes of non-circular cross-section. *International Journal of Engineering Science*, 20(7):863–872, 1982. 21

[88] C. G. Speziale. On nonlinear $k-l$ and $k-\varepsilon$ models of turbulence. *Journal of Fluid Mechanics*, 178:459–475, 1987. 21

[89] S. Nisizima. A numerical study of turbulent square-duct flow using an anisotropic $k-\varepsilon$ model. *Theoretical and Computational Fluid Dynamics*, 2(1):61–71, 1990. 21

[90] S. B. Pope. A more general effective-viscosity hypothesis. *Journal of Fluid Mechanics*, 72(2):331–340, 1975. 21

[91] R. Pecnik and G. Iaccarino. Predictions of turbulent secondary flows using the v^2-f model. In *38th Fluid Dynamics Conference and Exhibit*, page 3852, 2008. 21, 81, 82, 93, 99, 107, 110

[92] F. S. Lien, G. Kalitzin, and P. A. Durbin. RANS modelling for compressible and transitional flows. In *Summer Program Centre for Turbulence Research, Stanford*, pages 267–286. Citeseer, 1998. 21, 83

[93] D. Modesti. A priori tests of eddy viscosity models in square duct flow. *Theoretical and Computational Fluid Dynamics*, 34(5):713–734, 2020. 21

[94] F. Pimenta and M. A. Alves. Stabilization of an open-source finite-volume solver for viscoelastic fluid flows. *Journal of Non-Newtonian Fluid Mechanics*, 239:85–104, 2017. 25

[95] S. Azad, A. Riasi, and H. Amiri Moghadam. Parametric study of a viscoelastic RANS turbulence model in the fully developed channel flow. *Journal of Computational Applied Mechanics*, 48(1):65–74, 2017. 27, 96

[96] K. D. Housiadas and A. N. Beris. Characteristic scales and drag reduction evaluation in turbulent channel flow of non-constant viscosity viscoelastic fluids. *Physics of Fluids*, 16(5):1581–1586, 2004. 29

[97] C. Y. Lin and C. A. Lin. Direct Numerical Simulations of turbulent channel flow with polymer additives. *Journal of Mechanics*, 36(5):691–698, 2020. 30

[98] B. F. Gschaider. The incomplete swak4Foam reference. *Technical Report*, 131:202, 2013. 31

[99] M. McDermott, P. Resende, T. Charpentier, M. Wilson, A. Afonso, D. Harbottle, and G. de Boer. A FENE-P $k-\varepsilon$ viscoelastic turbulence model valid up to high drag reduction without friction velocity dependence. *Applied Sciences*, 10(22):8140, 2020. 35, 58, 83, 88, 90, 91, 94, 107, 109

[100] Y. Nagano and M. Hishida. Improved form of the $k-\varepsilon$ model for wall turbulent shear flows. *Journal of Fluids Engineering*, 109(2):156–160, 1987. 37, 59

[101] Y. Nagano. Modelling the dissipation-rate equation for two-equation turbulence model. In *9th Symposium on Turbulent Shear Flows*, pages 23–2, 1993. 37, 59

[102] L. Thais, T. B. Gatski, and G. Mompean. Some dynamical features of the turbulent flow of a viscoelastic fluid for reduced drag. *Journal of Turbulence*, 13(19):N19, 2012. 38, 39, 62, 63

[103] M. Masoudian, C. B. da Silva, and F. T. Pinho. Grid and subgrid-scale interactions in viscoelastic turbulent flow and implications for modelling. *Journal of Turbulence*, 17(6):543–571, 2016. 38, 39, 62, 63

[104] R. Benzi. A short review on drag reduction by polymers in wall bounded turbulence. *Physica D: Nonlinear Phenomena*, 239(14):1338–1345, 2010. 41, 43, 64

[105] T. S. Park and H. J. Sung. A nonlinear low-Reynolds number $k-\varepsilon$ model for turbulent separated and reattaching flows: Flow field computations. *International Journal of Heat and Mass Transfer*, 38(14):2657–2666, 1995. 43

[106] S. Wallin and A. V. Johansson. An explicit algebraic Reynolds stress model for incompressible and compressible turbulent flows. *Journal of Fluid Mechanics*, 403:89–132, 2000. 44, 60

[107] J. Bredberg, S. H. Peng, and L. Davidson. An improved $k-\omega$ turbulence model applied to recirculating flows. *International Journal of Heat and Fluid Flow*, 23(6):731–743, 2002. 58, 59, 78

[108] M. McDermott, P. R. Resende, M. C. T. Wilson, A. M. Afonso, D. Harbottle, and G. de Boer. An improved $k-\omega$ turbulence model for FENE-P fluids without friction velocity dependence. *International Journal of Heat and Fluid Flow*, 90:108799, 2021. 58, 88, 90, 91, 94, 95, 107, 109

[109] D. C. Wilcox. *Turbulence modelling for CFD*, volume 2. DCW Industries, 1998. 71

[110] P. S. Virk, E. W. Merrill, H. S. Mickley, K. A. Smith, and E. L. Mollo-Christensen. The toms phenomenon: turbulent pipe flow of dilute polymer solutions. *Journal of Fluid Mechanics*, 30(2):305–328, 1967. 73, 75

[111] P. G. Tucker. Prediction of turbulent oscillatory flows in complex systems. *International Journal for Numerical Methods in Fluids*, 33(6):869–895, 2000. 82

[112] R. Manceau, M. Wang, and P. Durbin. Assessment of non-local effect on pressure term in RANS modelling using a DNS database. In *Summer Program Centre for Turbulence Research, Stanford*, pages 303–322, 1998. 84

[113] R. Manceau and K. Hanjalić. A new form of the elliptic relaxation equation to account for wall effects in RANS modelling. *Physics of Fluids*, 12(9):2345–2351, 2000. 84

[114] F. T. Pinho, B. Sadanandan, and R. Sureshkumar. One equation model for turbulent channel flow with second order viscoelastic corrections. *Flow, Turbulence and Combustion*, 81(3):337–367, 2008. 89

[115] D. R. Laurence, J. C. Uribe, and S. V. Utyuzhnikov. A robust formulation of the $v^2 - f$ model. *Flow, Turbulence and Combustion*, 73(3):169–185, 2005. 111

[116] A. S. Pereira, G. Mompean, and E. J. Soares. Modeling and numerical simulations of polymer degradation in a drag reducing plane Couette flow. *Journal of Non-Newtonian Fluid Mechanics*, 256:1–7, 2018. 111